

# Large-eddy Simulations of a Jet in Crossflow Using Julia

Amelia Jane Thomas

January 3, 2018

*Thesis submitted for the degree of  
Master of Philosophy  
in  
Applied Mathematics  
at The University of Adelaide  
Faculty of Engineering, Computer and Mathematical Sciences  
School of Mathematical Sciences*



THE UNIVERSITY  
of ADELAIDE



# Contents

|   |             |
|---|-------------|
| <b>Signed Statement</b>                                     | <b>xv</b>   |
| <b>Acknowledgements</b>                                     | <b>xvii</b> |
| <b>Abstract</b>   | <b>xix</b>  |
| <b>1 Introduction</b>                                       | <b>1</b>    |
| 1.1 Jets in Crossflow . . . . .                             | 2           |
| 1.2 Problem Statement . . . . .                             | 5           |
| 1.2.1 Simulation Domain . . . . .                           | 5           |
| 1.2.2 Governing Equations . . . . .                         | 5           |
| 1.2.3 Non-Dimensionalisation . . . . .                      | 6           |
| 1.2.4 Boundary Conditions . . . . .                         | 7           |
| 1.2.5 Initial Conditions . . . . .                          | 9           |
| 1.3 Large-Eddy Simulation . . . . .                         | 9           |
| 1.3.1 Modification of the Navier–Stokes Equations . . . . . | 10          |
| 1.3.2 Sub-grid Models . . . . .                             | 11          |
| 1.4 Julia . . . . .   | 13          |
| 1.5 Thesis Summary . . . . .                                | 15          |
| <b>2 Numerical Methods</b>                                  | <b>17</b>   |
| 2.1 Considerations . . . . .                                | 17          |
| 2.2 Spatial Discretisation . . . . .                        | 20          |
| 2.2.1 Discretised Domain and Staggered Grid . . . . .       | 21          |
| 2.2.2 Interpolation . . . . .                               | 23          |
| 2.2.3 First Derivatives . . . . .                           | 23          |
| 2.2.4 Second Derivatives . . . . .                          | 24          |
| 2.2.5 Non-Linear Terms . . . . .                            | 24          |
| 2.3 Temporal Integration . . . . .                          | 26          |
| 2.3.1 Adam–Bashforth–Moulton Predictor-Corrector . . . . .  | 26          |
| 2.3.2 Euler Method . . . . .                                | 31          |

|          |  |           |
|----------|--|-----------|
| 2.4      | Boundary Conditions . . . . .                            | 31        |
| 2.4.1    | Outlet . . . . .   | 31        |
| 2.4.2    | No-slip walls . . . . .                                  | 32        |
| 2.5      | Pressure Correction . . . . .                            | 32        |
| 2.6      | Analysis . . . . .                                       | 35        |
| 2.6.1    | Mean Field . . . . .                                     | 35        |
| 2.6.2    | Trajectories . . . . .                                   | 35        |
| 2.6.3    | Jet Spreading . . . . .                                  | 37        |
| 2.6.4    | Spectra . . . . .  | 38        |
| 2.6.5    | Dissipation . . . . .                                    | 38        |
| 2.6.6    | Turbulent Kinetic Energy . . . . .                       | 39        |
| 2.6.7    | Vortex identification . . . . .                          | 40        |
| 2.7      | Implementation . . . . .                                 | 41        |
| 2.7.1    | Fourier transform . . . . .                              | 41        |
| 2.7.2    | Producing and factorising matrices . . . . .             | 41        |
| 2.7.3    | Calling Fortran functions . . . . .                      | 42        |
| 2.7.4    | Saving Data - HDF5 . . . . .                             | 42        |
| 2.8      | Comparisons to Known Solutions . . . . .                 | 43        |
| 2.9      | General flow properties . . . . .                        | 45        |
| 2.9.1    | Counter-rotating vortex pair . . . . .                   | 45        |
| 2.10     | Conclusion . . . . .                                     | 56        |
| <b>3</b> | <b>Comparison to experiments and other simulations</b>   | <b>57</b> |
| 3.1      | Comparison with published experimental results . . . . . | 58        |
| 3.2      | Comparison with published simulations . . . . .          | 60        |
| 3.2.1    | $Re = 1500, V_{av}/U_{max} = 1.52, d = 0.44$ . . . . .   | 60        |
| 3.2.2    | $Re = 6930, V_{av}/U_{max} = 3.3, d = 0.5$ . . . . .     | 61        |
| 3.2.3    | $Re = 20500, V_{av}/U_{max} = 0.5, d = 1$ . . . . .      | 62        |
| 3.3      | Verification against an alternative LES code . . . . .   | 69        |
| 3.3.1    | Trajectories . . . . .                                   | 69        |
| 3.3.2    | Velocity and Scalar Profiles . . . . .                   | 70        |
| 3.3.3    | Spectral density . . . . .                               | 77        |
| 3.3.4    | Turbulent Kinetic Energy . . . . .                       | 79        |
| 3.3.5    | Dissipation and Kolmogorov length scale . . . . .        | 81        |
| 3.4      | Conclusion . . . . .                                     | 84        |
| <b>4</b> | <b>Parameter Investigation - Velocity ratio</b>          | <b>85</b> |
| 4.1      | Trajectories . . . . .                                   | 85        |
| 4.2      | Jet Spreading . . . . .                                  | 90        |
| 4.3      | Spectra . . . . .  | 92        |
| 4.4      | Dissipation and Kolmogorov length scale . . . . .        | 95        |

|          |  |            |
|----------|--|------------|
| 4.5      | Conclusion . . . . .   | 98         |
| <b>5</b> | <b>Comparison of large-eddy simulation and direct numerical simulation</b> | <b>99</b>  |
| 5.1      | Velocity and scalar profiles . . . . .                                     | 100        |
| 5.2      | Trajectories . . . . .   | 107        |
| 5.3      | Spectra . . . . .  | 110        |
| 5.4      | Kolmogorov length scale ratio . . . . .                                    | 114        |
| 5.5      | Conclusion . . . . .   | 117        |
| <b>6</b> | <b>Conclusion</b>  | <b>119</b> |
| 6.1      | Future work . . . . .  | 120        |
|          | <b>Bibliography</b>  | <b>123</b> |



# List of Tables

|     |   |    |
|-----|---|----|
| 3.1 | Table of parameters for simulations discussed in this chapter, showing Reynolds number, $Re$ , velocity ratio, $V_{av}/U_{max}$ , and crossflow boundary layer thickness, $d$ . . . . . | 57 |
| 4.1 | Names and parameters for the three simulations discussed in this chapter. . . . .   | 85 |
| 5.1 | Names, simulation types and parameters of the four simulations discussed in this chapter. . . . .   | 99 |





# List of Figures

|     |  |    |
|-----|--|----|
| 1.1 | (a) Diagram and (b) photo displaying vortex types seen in jets in crossflow. Crossflow direction in (a) is indicated by large arrow, and in (b) is from left to right. Images reproduced from Kelso et al. [22]. . . . .   | 2  |
| 1.2 | Isosurface of enstrophy showing ring vortex folding that leads to CVP formation. . . . .   | 3  |
| 1.3 | Simulation domain with location and size of jet inlet indicated by a black circle. . . . .   | 6  |
| 1.4 | Crossflow inlet profile, $U_{in}(y)$ . . . . .   | 8  |
| 1.5 | Poiseuille jet profile . . . . .   | 9  |
| 2.1 | Modified wavenumber ( $\kappa'$ ) vs wavenumber ( $\kappa$ ) for second-order central-difference (green), fourth order central-difference (blue), 6th order central-difference (red) and spectral methods (black dashed line). $\Delta$ is the grid spacing. . . . . | 19 |
| 2.2 | Simulation domain with one slice shaded. For any particular value of $z$ , in this case $z = 0$ , all data points are located within the indicated plane. . . . .  | 22 |
| 2.3 | Four staggered grid cells. Positions where different terms are calculated are as marked. . . . .   | 23 |
| 2.4 | Stability boundary of Adam–Bashforth–Moulton method, for complex values of $\lambda\Delta t$ . . . . .   | 29 |
| 2.5 | Running Averages of (a) speed and (b) concentration at $(x, y, z) = (7.7, 5.9, 0)$ for $Re = 2 \times 10^4$ and $V_{av}/U_{max} = 2.25$ . . . . .  | 36 |
| 2.6 | Average error in $u$ (blue), $v$ (red) and $w$ (black) over time for Taylor-Green vortex with $\nu = 0$ . . . . .  | 44 |
| 2.7 | Isosurfaces of streamwise velocity, $u = 1.2$ , for $V_{av}/U_{max} = 2.3$ and $Re = 640$ , at non-dimensional times of (a) 6.9, (b) 34.5, and (c) 69 and (d) the temporal average taken after the transient stage has passed. . . . .                               | 46 |

|      |   |    |
|------|---|----|
| 2.8  | Isosurfaces of transverse velocity, with increasing opacity indicating increasing velocity, for $V_{av}/U_{max} = 2.3$ and $Re = 640$ , at non-dimensional times of (a) 6.9, (b) 34.5, and (c) 69 and (d) the temporal average taken after the transient stage has passed.                                    | 47 |
| 2.9  | Isosurfaces of cross-stream velocity, with increasing opacity indicating increasing velocity and colours indicating direction, for $V_{av}/U_{max} = 2.3$ and $Re = 640$ , at non-dimensional times of (a) 6.9, (b) 34.5, and (c) 69 and (d) the temporal average taken after the transient stage has passed. | 48 |
| 2.10 | Isosurfaces of scalar concentration, for $V_{av}/U_{max} = 2.3$ and $Re = 640$ , at non-dimensional times of (a) 6.9, (b) 34.5, and (c) 69 and (d) the temporal average taken after the transient stage has passed.   | 49 |
| 2.11 | Isosurfaces of (a) cross-stream vorticity, $\omega_z = 5$ , and (b) enstrophy, $\omega^2 = 20$ , at 10000 timesteps, showing spanwise rollers.  | 50 |
| 2.12 | Isosurface of time-averaged enstrophy, $\omega^2 = 5$ , showing CVP development.  | 51 |
| 2.13 | Isosurface of the time-averaged discriminant, $\Delta = 1 \times 10^{-3}$ showing CVP.  | 52 |
| 2.14 | Contours of time-averaged scalar concentration in $yz$ -plane. Slices taken at (a) $x = 1$ , (b) $x = 3.5$ , (c) $x = 6$ , (d) $x = 8.5$ , (e) $x = 11$ and (f) $x = 13.5$ .  | 54 |
| 2.15 | Contours of time-averaged vorticity in $yz$ -plane overlaid with quiver plot of velocity. Slices taken at (a) $x = 1$ , (b) $x = 3.5$ , (c) $x = 6$ , (d) $x = 8.5$ , (e) $x = 11$ and (f) $x = 13.5$ .   | 55 |
| 3.1  | Counter-rotating vortex pair trajectories of my simulation (line) and Cambonie et al.'s configuration 1 (circles) for (a) $Re = 243$ , $V_{av}/U_{max} = 0.54$ , $d = 1.83$ , and (b) $Re = 640$ , $V_{av}/U_{max} = 3.05$ and $d = 2.06$ .   | 59 |
| 3.2  | Centreline trajectory from my simulation (blue line) and that of Muppidi and Mahesh [40] (orange circles).  | 60 |
| 3.3  | Velocity magnitude profiles in the jet centreline, $z = 0$ , from my simulation (blue lines) and Yuan et al. [59] (orange circles). Profiles are given at (a) the centre of the jet inlet at $x = 0$ , and downstream of the jet inlet at (b) $x = 1.84$ , (c) $x = 3.67$ and (d) $x = 5.54$ .                | 62 |
| 3.4  | Streamwise velocity profiles for my simulation (blue lines) and Wegner et al. [56] (orange circles). Profiles given at (a) $x = -0.5$ , (b) $x = -0.25$ , (c) $x = 0$ , (d) $x = 0.25$ , (e) $x = 0.5$ , (f) $x = 1$ , (g) $x = 2$ , and (h) $x = 4$ .  | 65 |

|      |   |    |
|------|---|----|
| 3.5  | Transverse velocity profiles for my simulation (blue lines) and Wegner et al. [56] (orange circles). Profiles given at (a) $x = -0.5$ , (b) $x = -0.25$ , (c) $x = 0$ , (d) $x = 0.25$ , (e) $x = 0.5$ , (f) $x = 1$ , and (g) $x = 2$ . . . . .  | 66 |
| 3.6  | Concentration profiles for my simulation (blue lines) and Wegner et al. [56] (orange circles). Profiles given at (a) $x = -0.25$ , (b) $x = 0$ , (c) $x = 0.5$ , (d) $x = 1$ , (e) $x = 2$ , and (f) $x = 4$ . . . . .  | 67 |
| 3.7  | Turbulent kinetic energy profiles for my simulation (blue lines) and Wegner et al. [56] (orange circles). Profiles given at (a) $x = -0.25$ , (b) $x = 0$ , (c) $x = 0.25$ , (d) $x = 0.5$ , (e) $x = 1$ , (f) $x = 2$ , and (g) $x = 4$ . . . . .  | 68 |
| 3.8  | (a) Centreline, (b) concentration and (c) CVP trajectories of my simulation (blue) and Mattner's simulation (red). . . . .  | 72 |
| 3.9  | Contours of vertical velocity in the cross section at (a) $x = 5$ , (b) $x = 8$ , (c) $x = 11$ and (d) $x = 14$ , for my simulation (left) and Mattner's simulation (right). Also shown are the positions of the jet centreline trajectory (magenta circle) and CVP trajectory (red square). White areas are regions where the vertical velocity is less than $-0.05$ . . . . . | 73 |
| 3.10 | Streamwise velocity profiles for my simulation (blue lines) and Mattner's simulation (orange lines) at (a) $x = -2.5$ , (b) $x = 0$ , (c) $x = 1$ , (d) $x = 2$ , (e) $x = 4$ , (f) $x = 10$ , (g) $x = 14$ . . . . .   | 74 |
| 3.11 | Transverse velocity profiles for my simulation (blue lines) and Mattner's simulation (orange lines) at (a) $x = -2.5$ , (b) $x = 0$ , (c) $x = 1$ , (d) $x = 2$ , (e) $x = 4$ , (f) $x = 10$ , (g) $x = 14$ . . . . .   | 75 |
| 3.12 | Scalar concentration profiles for my simulation (blue lines) and Mattner's simulation (orange lines) at (a) $x = -2.5$ , (b) $x = 0$ , (c) $x = 1$ , (d) $x = 2$ , (e) $x = 4$ , (f) $x = 10$ , (g) $x = 14$ . . . . .  | 76 |
| 3.13 | Time averaged spectral density of velocity components, (a) kinetic energy and (b) scalar concentration, taken at $(x, y) = (7.7, 5.9)$ , for my simulation (blue) and $(x, y) = (7.7, 5.0)$ for Mattner's simulation (red). Black dashed line has ideal $-\frac{5}{3}$ slope. . . . .   | 78 |
| 3.14 | Contour plots of turbulent kinetic energy ratio at $z = 0$ , with 0.8 contour marked in black for (a) my simulation and (b) Mattner's simulation. . . . .   | 80 |
| 3.15 | Logarithm of point-wise dissipation ratio on plane $z = 0$ for regions where scalar concentration $c \geq 0.05$ for (a) my simulation and (b) Mattner's simulation. Black line shows contour where $\log(\varepsilon_{SGS}/\varepsilon_{LS}) = 0$ . . . . .   | 82 |

|      |  |     |
|------|--|-----|
| 3.16 | Point-wise Kolmogorov length scale ratio on plane $z = 0$ for regions where scalar concentration $c \geq 0.05$ for (a) my simulation and (b) Mattner's simulation. . . . .   | 83  |
| 4.1  | (a) Centreline, (b) concentration and (c) CVP trajectories of $V_{av}/U_{max} = 0.405$ (blue), $V_{av}/U_{max} = 2.25$ (green) and $V_{av}/U_{max} = 3$ (red) simulations. . . . .   | 88  |
| 4.2  | Isosurfaces of scalar concentration for simulations run at (a) $V_{av}/U_{max} = 0.405$ and (b) $V_{av}/U_{max} = 2.25$ . . . . .  | 89  |
| 4.3  | (a) Vertical and (b) horizontal spreading of the jet for $V_{av}/U_{max} = 0.405$ (blue), $V_{av}/U_{max} = 2.25$ (green) and $V_{av}/U_{max} = 3$ (red) simulations. . . . .  | 91  |
| 4.4  | Isosurfaces of scalar concentration for $V_{av}/U_{max} = 3$ simulation. Isosurface values are 1 (dark blue), 0.5 (cyan) and 0.05 (pink) . . . . .   | 92  |
| 4.5  | Spectra of velocity components (a) kinetic energy, and (b) scalar concentration for $V_{av}/U_{max} = 0.405$ (blue), $V_{av}/U_{max} = 2.25$ (green) and $V_{av}/U_{max} = 3$ (red) simulations, with optimal [37] $-\frac{5}{3}$ slope marked (dashed line). . . . .  | 94  |
| 4.6  | Logarithm of point-wise dissipation ratio on plane $z = 0$ for regions where scalar concentration $c \geq 0.05$ for simulations run at (a) $V_{av}/U_{max} = 0.405$ , (b) $V_{av}/U_{max} = 2.25$ and (c) $V_{av}/U_{max} = 3$ . Black line shows contour where $\log(\varepsilon_{SGS}/\varepsilon_{LS}) = 0$ . . . . . | 96  |
| 4.7  | Point-wise Kolmogorov length scale ratio on plane $z = 0$ for regions where scalar concentration $c \geq 0.05$ for simulations run at (a) $V_{av}/U_{max} = 0.405$ , (b) $V_{av}/U_{max} = 2.25$ and (c) $V_{av}/U_{max} = 3$ . . . . .  | 97  |
| 5.1  | Profiles of $u$ for LES (blue) and DNS (black), for $Re = 640$ and $V_{av}/U_{max} = 3.05$ , at (a) $x = -2$ , (b) $x = 0$ , (c) $x = 1$ , (d) $x = 2$ , (e) $x = 4$ , and (f) $x = 10$ . Note that the horizontal range changes between profiles. . . . .   | 101 |
| 5.2  | Profiles of $v$ for LES (blue) and DNS (black), for $Re = 640$ and $V_{av}/U_{max} = 3.05$ , at (a) $x = -2$ , (b) $x = 0$ , (c) $x = 1$ , (d) $x = 2$ , (e) $x = 4$ , and (f) $x = 10$ . Note that the horizontal range changes between profiles. . . . .   | 102 |
| 5.3  | Profiles of $c$ for LES (blue) and DNS (black), for $Re = 640$ and $V_{av}/U_{max} = 3.05$ , at (a) $x = -2$ , (b) $x = 0$ , (c) $x = 1$ , (d) $x = 2$ , (e) $x = 4$ , and (f) $x = 10$ . Note that the horizontal range changes between profiles. . . . .   | 103 |

|      |   |     |
|------|---|-----|
| 5.4  | Profiles of $u$ for LES (blue) and DNS (black) for $\text{Re} = 13640$ and $V_{av}/U_{max} = 2.2$ , at (a) $x = -2$ , (b) $x = 0$ , (c) $x = 1$ , (d) $x = 2$ , (e) $x = 4$ , and (f) $x = 10$ . Note that the horizontal range changes between profiles. . . . .                       | 104 |
| 5.5  | Profiles of $v$ for LES (blue) and DNS (black) for $\text{Re} = 13640$ and $V_{av}/U_{max} = 2.2$ , at (a) $x = -2$ , (b) $x = 0$ , (c) $x = 1$ , (d) $x = 2$ , (e) $x = 4$ , and (f) $x = 10$ . Note that the horizontal range changes between profiles. . . . .                       | 105 |
| 5.6  | Profiles of $c$ for LES (blue) and DNS (black) for $\text{Re} = 13640$ and $V_{av}/U_{max} = 2.2$ , at (a) $x = -2$ , (b) $x = 0$ , (c) $x = 1$ , (d) $x = 2$ , (e) $x = 4$ , and (f) $x = 10$ . Note that the horizontal range changes between profiles. . . . .                       | 106 |
| 5.7  | Comparison of (a) centreline, (b) concentration and (c) CVP trajectories of LES (blue) and DNS (black) simulations for $\text{Re} = 640$ and $V_{av}/U_{max} = 3.05$ . . . . .  | 108 |
| 5.8  | Comparison of (a) centreline, (b) concentration and (c) CVP trajectories of LES (blue) and DNS (black) simulations for $\text{Re} = 13640$ and $V_{av}/U_{max} = 2.2$ . . . . .   | 109 |
| 5.9  | Spectra of components of velocity (a) kinetic energy, and (b) scalar concentration of LES (blue) and DNS (black) simulations for $\text{Re} = 640$ and $V_{av}/U_{max} = 3.05$ . . . . .  | 112 |
| 5.10 | Spectra of components of velocity (a) kinetic energy, and (b) scalar concentration of LES (blue) and DNS (black) simulations for $\text{Re} = 13640$ and $V_{av}/U_{max} = 2.2$ . . . . .   | 113 |
| 5.11 | Point-wise Kolmogorov length scale ratio on plane $z = 0$ for regions where scalar concentration $c \geq 0.05$ (a) LES and (b) DNS simulations run at $V_{av}/U_{max} = 3.05$ , $d = 2.06$ and $\text{Re} = 640$ . Black line indicates the contour where $\eta/\Delta x = 1$ . . . . . | 115 |
| 5.12 | Point-wise Kolmogorov length scale ratio on plane $z = 0$ for regions where scalar concentration $c \geq 0.05$ (a) LES and (b) DNS simulations run at $V_{av}/U_{max} = 2.2$ , $d = 0.28$ and $\text{Re} = 13640$ . . . . .   | 116 |



# Signed Statement

I certify that this work contains no material which has been accepted for the award of any other degree or diploma in my name, in any university or other tertiary institution and, to the best of my knowledge and belief, contains no material previously published or written by another person, except where due reference has been made in the text. In addition, I certify that no part of this work will, in the future, be used in a submission in my name, for any other degree or diploma in any university or other tertiary institution without the prior approval of the University of Adelaide and where applicable, any partner institution responsible for the joint-award of this degree.

I give permission for the digital version of my thesis to be made available on the web, via the University's digital research repository, the Library Search and also through web search engines, unless permission has been granted by the University to restrict access for a period of time.

I acknowledge the support I have received for my research through the provision of an Australian Government Research Training Program Scholarship.

Signed: ... ..... Date: January 25, 2018





# Acknowledgements

This work would have been difficult to achieve without the assistance and support of many people. First and foremost, I would like to thank my supervisors, Dr Trent Mattner and Associate Professor Yvonne Stokes. Trent has taught me all that I know about turbulence, and much of what I know about computational mathematics. He has also taught me many bad maths habits. Yvonne has tried to break those bad habits before they stuck, and has done her best to turn me into a proper mathematician. Without their support I would not have reached this point.

The financial support of the University of Adelaide Graduate Centre (scholarship), and of the School of Mathematical Sciences is acknowledged.

My thanks go to my parents, Alun Thomas and Kathleen Cunningham, and my best friend Karyn Hulbert, for their willingness to smile and nod while I rambled on about mathematics that they don't quite understand. They have been the support that kept me going, even in the toughest of times.

Finally to my other friends, Caroline Phillips, Bill Pearce and Steph Ducker, who I can always count on for coffee or lunch whenever I forget how to be social. My continued sanity is all thanks to you.



# Abstract

The jet in crossflow (JICF) is a complex flow that has applications in many fields, from pollutant dispersion into air or water to the injection and mixing of fuel in engines. In this thesis, large-eddy simulations, using a stretched-vortex sub-grid model, of a JICF with a non-reactive scalar are performed using a discrete numerical method that is implemented using code written in the computational language Julia. Velocity profiles, trajectories, entrainment, power spectra, turbulent kinetic energy and dissipation of energy are analysed for simulations run at velocity ratios varying between 0.405 and 3.3, crossflow boundary layer thicknesses between 0.28 and 2.06 and Reynolds numbers between 243 and 20500.

Simulations are compared to published experimental and simulation-based results, and a full comparison was performed with a simulation provided by Mattner, run on the same computational grid. It was found that the mathematical model used in this thesis performs better at higher velocities and Reynolds numbers.

An investigation into the effect of the ratio of average jet inlet velocity to maximum crossflow velocity was performed. It was found that a jet with a higher velocity ratio showed increased penetration into the crossflow. The amount of turbulent kinetic and scalar energy in the system, as well as the amount of dissipation of energy from the system, also increased with velocity ratio.

Finally, a comparison of large-eddy simulation (LES) and direct numerical simulation (DNS) of a JICF was performed on the same computational grid for low and moderate Reynolds numbers. At low Reynolds numbers the differences in results between the LES and DNS are minor, although it is not possible to resolve the flow on the computational grid that is used. At moderate Reynolds numbers, above  $Re = 1 \times 10^4$ , the differences between the LES and DNS are more pronounced. Deeper jet penetration is seen in the LES than in the DNS, and the distribution of energy in the system is different, with the sub-grid model used in the LES dissipating more energy from the high wavenumber scales.



# Chapter 1

## Introduction

The jet in crossflow is a complex flow in which a narrow stream of fluid, the jet, is injected into a larger flow, the crossflow, as shown in Figure 1.1. The jet can be injected perpendicularly to the crossflow, or at an angle, pointing either upstream or downstream of the injection point. At sufficiently high Reynolds number the interaction between them may be turbulent, causing crossflow fluid close to the jet inlet to be entrained into the jet plume at a higher rate than would be seen in the equivalent jet injected into stationary fluid [41]. It is this enhanced mixing ability that makes the jet in crossflow desirable for use in a number of systems, such as fuel injection in engines and the dispersal of pollutants from smoke stacks.

Depending on the application, the jet and crossflow can be fluids of different densities. In this thesis we assume that both the jet and crossflow are fluids of the same density, and that the fluid is incompressible.

Turbulence is characterised by fast and irregular changes in velocity and pressure, and causes strong three-dimensional vortices to develop within a fluid flow. Turbulence exists on a wide range of length scales, from large to extremely small at high Reynolds numbers, and resolving all of these scales requires a very fine grid. In many applications it is prohibitively expensive, both in terms of time and computational power, to perform simulations on such a large grid of points, so, in order to perform simulations in a reasonable amount of time, models are used to approximate the effect of the smallest scales of turbulence on the large-scale flow. Models allow for fewer grid points to be used, so the simulation is considerably less expensive. This method is known as large-eddy simulation (LES), and models have been developed for the approximation of the sub-grid stresses and flux.

In this thesis, a discrete numerical method written in the computational language Julia is used to perform a large-eddy simulation of a jet in crossflow. Julia is a new open-source language built for both efficiency and ease of

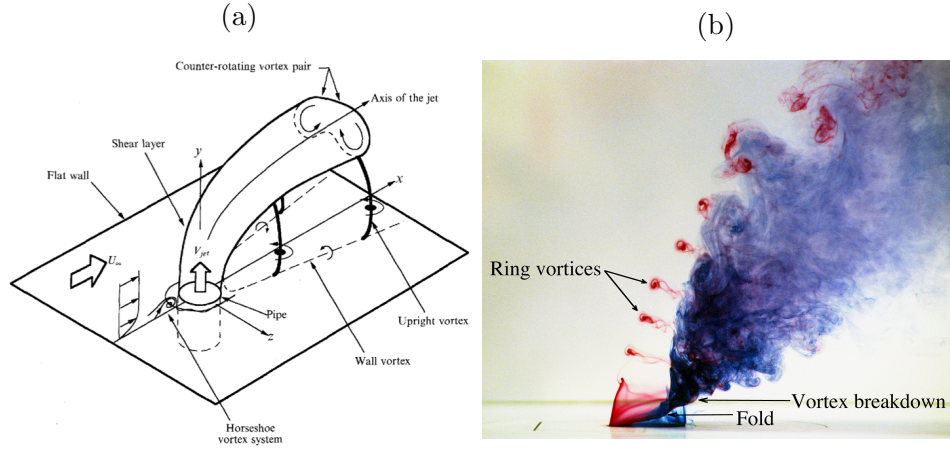


Figure 1.1: (a) Diagram and (b) photo displaying vortex types seen in jets in crossflow. Crossflow direction in (a) is indicated by large arrow, and in (b) is from left to right. Images reproduced from Kelso et al. [22].

use, with support for code parallelisation, presenting new opportunities for scientific and mathematical computing.

## 1.1 Jets in Crossflow

Jets in crossflow have been studied extensively both numerically and experimentally, as they have a wide range of applications across many fields, such as fuel mixing, pollutant dispersal and the estimation of the impact of volcanic ash plumes after an eruption [29]. Jets in crossflow display a number of interesting vortex structures whose appearance depends on the ratio of the jet and crossflow velocities, as well as the jet and crossflow velocity profiles. The crossflow is a free stream flow that can be uniform or non-uniform, and may have a laminar or turbulent wall boundary layer; here  $U_{\max}$  denotes the maximum crossflow velocity at the inlet. The jet may be laminar or turbulent when it enters the flow;  $V_{av}$  denotes the average jet velocity at the jet inlet. The ratio of the jet and crossflow velocities is quantified by  $V_{av}/U_{\max}$ , and is known as the velocity ratio.

There are a number of methods used to track the trajectory of a jet as it interacts with a crossflow. One of these methods defines the trajectory as the streamline starting at the centre of the jet inlet [8, 40]. This streamline can be calculated either in the full three dimensional domain, or in the plane that passes through the centre of the jet inlet. In a situation where a scalar quantity such as concentration enters the flow via the jet inlet, the maximum

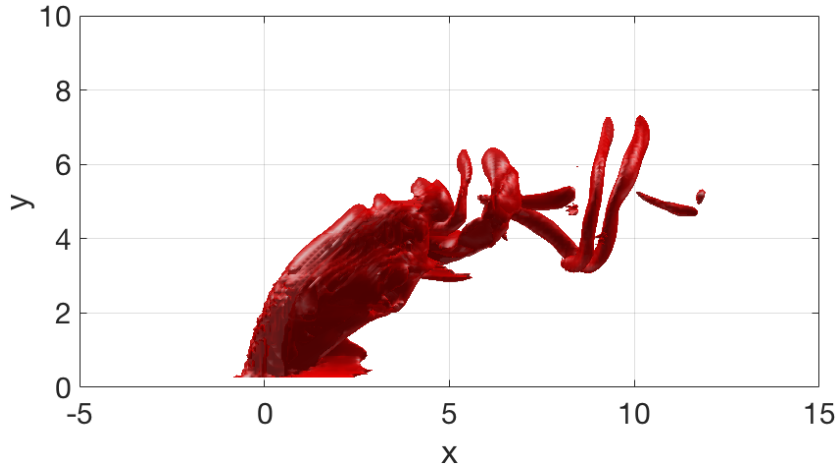


Figure 1.2: Isosurface of enstrophy showing ring vortex folding that leads to CVP formation.

value of the scalar at each position downstream of the jet can also be used as a definition of the trajectory, as the scalar in the central region of the jet will be the least mixed with the surrounding fluid [49]. It has been found that the trajectory of the jet, once it encounters the crossflow, depends on the ratio of the velocities of the jet and the crossflow [20, 40], with higher velocity ratios leading to deeper penetration. The shape of the jet velocity profile can also affect the depth of penetration, with parabolic profiles penetrating much further than plug-shaped profiles of the same average jet inlet velocity [40].

A well documented form of vortex that appears in a jet in crossflow is the counter-rotating vortex pair (CVP), seen in Figure 1.1. These develop downstream of the jet inlet, and persist far downstream [6]. They are caused by the interactions in the shear layer between the two flows [22]. Near to the jet inlet, the shear layer of the jet folds, and rolls up into a vortex ring, called spanwise rollers by Yuan et al. [59], surrounding the jet [22]. These vortex rings are deformed by the different conditions on the upstream and downstream sides of the jet, and this deformation causes the vortex ring to fold on the downstream side of the jet, so that the upstream portion of the vortex ring remains curved around the jet, and the downstream portion aligns with the direction of the jet [12]. It is this downstream portion that contributes to the CVP's development. An example of this vortex folding can be seen in Figure 1.2. The distance downstream of the jet inlet to which the CVP persists increases with the velocity ratio [20]. Kamotani and Greber [21] found that increasing the velocity ratio delayed the formation of the CVP.

The trajectory of the CVP, which generally differs from the centreline trajectory, is also used to investigate the jet in crossflow. The CVP trajectory is less easily tracked than the centreline trajectory, as the CVP does not begin immediately when the jet enters the flow, but develops as the jet travels downstream [6]. Once the CVP develops, its trajectory is defined as either the line of maximum vorticity within one of the vortices in the pair [17] or as the line of maximum vertical velocity [6]. Often the line of maximum vertical velocity is chosen as it is simpler to measure. Penetration of the CVP is affected by the velocity ratio,  $V_{av}/U_{max}$ , and jet velocity profile in a similar manner to the jet trajectory [40], however these are not the only factors that have an effect. The depth of the boundary layer of the crossflow can also alter the height of the CVP trajectory. A thin boundary layer has more momentum close to the jet injection nozzle, which causes the jet to bend earlier, and the CVP to develop closer to the lower wall [6].

Other types of vortices identified by Kelso et al. [22] in their flow visualisation experiments include horseshoe vortices that surround the upstream side of the jet inlet, ring-like vortices that shed from the near field shear layer, and streamwise wall vortices and vertical shedding vortices that appear beneath the downstream side of the jet. All of these vortices contribute to the mixing properties of the system.

Wegner et al. [56] investigated the relationship between the angle of the jet with respect to the crossflow and the extent to which the two fluids mixed, using large-eddy simulation with a Smagorinsky turbulence model [28] to model the sub-grid turbulence and an eddy-viscosity model for the sub-grid flux. The large-scale flow was simulated using a finite volume method for the spatial derivatives, and a second-order Crank–Nicholson scheme for the temporal integration. They found that the flows mixed more effectively, and in a shorter distance, for jets inclined more strongly against the direction of the crossflow. This more effective mixing was caused by the stronger shear between the two flows, which led to stronger vortices forming, and thus more entrainment of the crossflow fluid into the jet. An inclined gas phase sonic jet entering a supersonic turbulent crossflow was also investigated by Ferrante et al. [18], using large-eddy simulation with the stretched-vortex sub-grid model. Different methods of producing turbulent inflow conditions were compared, and it was found that synthetic turbulence constructed from a modified version of the method given by Le et al. [27] produced large amounts of turbulent kinetic energy closer to the jet inlet than either single mode forcing or a non-turbulent inflow condition. Cutler [13] found that the decay of concentration on the jet centreline increased with velocity ratio, indicating increased mixing.



## 1.2 Problem Statement

We consider a constant density incompressible jet in crossflow, where the jet enters the domain perpendicular to the crossflow, as shown in Figure 1.1. We investigate the influence of the ratio of average jet velocity to maximum crossflow velocity on characteristics of the flow, such as the trajectory, power spectra and dissipation. Large-eddy simulation (LES) is used to model the sub-grid scale stresses and flux, and results of these simulations are compared to equivalent direct numerical simulations (DNS) on the same grid to ascertain the effect of the LES model. Both low and medium Reynolds numbers are considered.

### 1.2.1 Simulation Domain

The simulation domain, shown in Figure 1.3, is a rectangular prism. The  $x$ -direction is the streamwise direction, that is the direction of the crossflow. The  $y$ -direction is the transverse direction, and the  $z$ -direction is the cross-stream direction. The components of velocity in the  $x$ -,  $y$ -, and  $z$ -directions are  $u$ ,  $v$ , and  $w$  respectively. The crossflow enters the region at  $x = -5L$  and exits at  $x = 15L$ , where  $L$  is the diameter of the jet, while the jet enters the region at  $(x/L, y/L, z/L) = (0, 0, 0)$ . The two side boundaries, at  $z = \pm 5L$ , have periodic boundary conditions, which results in the simulation actually being of an infinite array of cloned jets, rather than a single jet. The height and width of the domain have been set to 10 times the diameter of the jet so that the jet does not come into contact with the top wall or either of the side boundaries.

### 1.2.2 Governing Equations

The motion of a constant density incompressible fluid is governed by the incompressible Navier–Stokes equations,

$$\frac{\partial u_i}{\partial t} + u_j \frac{\partial u_i}{\partial x_j} = -\frac{1}{\rho} \frac{\partial P}{\partial x_i} + \nu \frac{\partial^2 u_i}{\partial x_j \partial x_j}, \quad (1.1)$$

and the continuity equation,

$$\frac{\partial u_i}{\partial x_i} = 0, \quad (1.2)$$

presented using Einstein notation, where repeated indices imply summation, and where  $x_i$  is the  $i$ -th coordinate in a Cartesian coordinate system,  $u_i$  is the velocity in the  $i$ -th direction,  $t$  is time,  $P$  is pressure,  $\rho$  is density, and  $\nu$  is the kinematic viscosity. Equation (1.1) ensures conservation of momentum, while

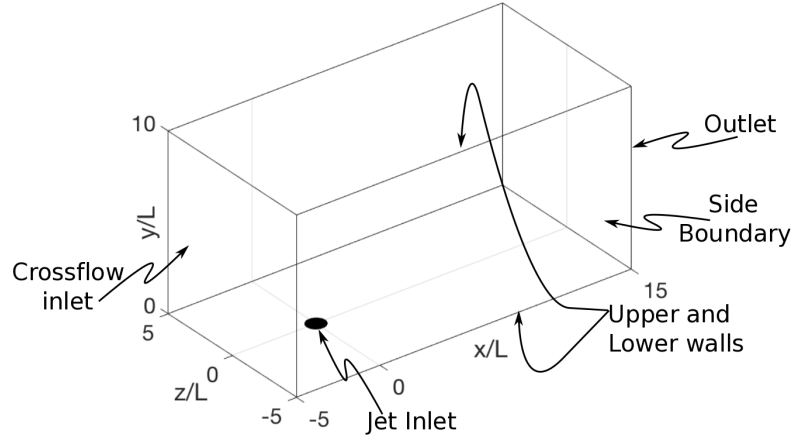


Figure 1.3: Simulation domain with location and size of jet inlet indicated by a black circle.

equation (1.2) ensures conservation of mass. In addition to these equations, a scalar transport equation,

$$\frac{\partial c}{\partial t} + u_j \frac{\partial c}{\partial x_j} = \mathcal{D} \frac{\partial^2 c}{\partial x_j \partial x_j}, \quad (1.3)$$

which conserves the mass of the scalar, is used to track the concentration of a dye or other non-reactive substance within the fluid. In this equation,  $c$  is the concentration of the scalar and  $\mathcal{D}$  is the diffusivity of the scalar. Again, Einstein summation notation has been used.

### 1.2.3 Non-Dimensionalisation

Equations (1.1)-(1.3) are non-dimensionalised to extract dimensionless parameters that define properties of the flow. A set of dimensionless parameters, indicated by stars, are defined as

$$u_i^* = \frac{u_i}{V_{av}}, \quad x_i^* = \frac{x_i}{L}, \quad P^* = \frac{P}{V_{av}^2 \rho}, \quad t^* = \frac{t}{T}, \quad c^* = \frac{c}{C},$$

where  $V_{av}$  is the average jet velocity at the inlet,  $L$  is the diameter of the jet,  $C$  is the concentration of the scalar at the jet inlet, assumed to be constant, and  $T = L/V_{av}$  is the characteristic time scale. With these scalings, equations (1.1)-(1.3) become

$$\frac{\partial u_i^*}{\partial t^*} + u_j^* \frac{\partial u_i^*}{\partial x_j^*} = -\frac{\partial P^*}{\partial x_i^*} + \frac{1}{\text{Re}} \frac{\partial^2 u_i^*}{\partial x_j^* \partial x_j^*}, \quad (1.4)$$

$$\frac{\partial u_i^*}{\partial x_i^*} = 0, \quad (1.5)$$

$$\frac{\partial c^*}{\partial t^*} + u_j^* \frac{\partial c^*}{\partial x_j^*} = \frac{1}{\text{Pe}} \frac{\partial^2 c^*}{\partial x_j^* \partial x_j^*}, \quad (1.6)$$

where  $\text{Re} = V_{av}L/\nu$  is the Reynolds number, and  $\text{Pe} = V_{av}L/\mathcal{D}$  is the Péclet number. We use the Reynolds number as a guide to determine whether the flow is turbulent or laminar. Dimotakis [15] found that a Reynolds number, defined as it is here, of approximately  $1 - 2 \times 10^4$  marked a transition to a fully developed turbulent flow, independent of the flow geometry. The Péclet number is used to determine whether advection or diffusion dominate the transport of the scalar. A Péclet number greater than 1 indicates that advection dominates, and a Péclet number of less than 1 indicates that diffusion dominates. The Péclet number can also be written as  $\text{Pe} = \text{Re} \times \text{Sc}$ , where  $\text{Sc} = \nu/\mathcal{D}$  is the Schmidt number, the ratio of momentum diffusivity to mass diffusivity. In this thesis the Schmidt number is fixed at 0.7 for all simulations, which is typical of gas-phase mixing, and the effect of the Reynold number is investigated.

From this point forward, the asterisks will be dropped from the dimensionless variables.

## 1.2.4 Boundary Conditions

Boundary conditions for velocity and scalar concentration at the inlet,  $x = -5$ , outlet,  $x = 15$ , and upper and lower walls,  $y = 0$  and  $y = 10$ , are specified below. The final two boundaries,  $z = \pm 5$ , are periodic in both velocity and scalar concentration.

### Velocity Conditions

At the crossflow inlet,  $x = -5$ , Dirichlet boundary conditions are specified for all three components of velocity. The velocities in the  $y$  and  $z$  directions are set to zero, while  $u$  is given the velocity profile,

$$u(-5, y, z) = U_{\text{in}}(y) = U_{\text{max}} \left(1 - e^{-\frac{10y}{d}}\right), \quad (1.7)$$

as shown in Figure 1.4. This profile has an artificial boundary layer near  $y = 0$  whose thickness is determined by the parameter  $d$ . For  $y \geq d$  the profile has  $u \approx U_{\text{max}}$ , including the upper wall at  $y = 10$ , which is well beyond the boundary layer. The boundary layer was chosen on the lower wall to remove the numerical discontinuity between the streamwise velocity on the lower wall and that within the jet inlet.

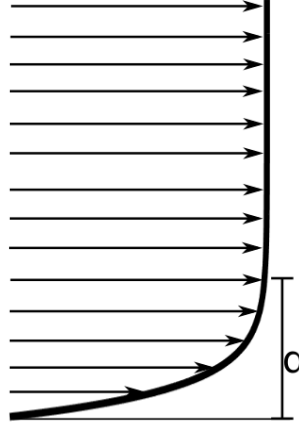


Figure 1.4: Crossflow inlet profile,  $U_{in}(y)$

At the outlet, it is desirable for flow structures to be removed smoothly from the simulation region. In order to achieve this, an advective outlet condition is used [43]. The form of this condition is:

$$\frac{\partial \phi}{\partial t} - \beta \frac{\partial \phi}{\partial x} = 0, \quad (1.8)$$

where  $\phi$  is any component of velocity, and  $\beta$  is a constant. In these simulations  $\beta$  is chosen to be the free stream velocity of the crossflow,  $U_{max}$ .

The upper and lower walls of the simulation region are solid, and do not allow any material to pass through them. As such, at these boundaries  $v = 0$ . Conditions on the other two components of velocity at this boundary are determined to enforce the no-slip condition on the walls. The no-slip condition is that  $u = w = 0$  on these walls.

Dirichlet boundary conditions are also applied at the circular jet inlet. A circular Poiseuille profile, defined by the radial distance  $r$  from the centre of the jet inlet, is used at the jet inlet. The radially symmetric velocity profile over the jet inlet is given as

$$V_{jet} = 2(1 - 4r^2), \quad r \leq \frac{1}{2}. \quad (1.9)$$

This allows the average jet velocity over the inlet to be calculated as

$$V_{av} = \frac{\int_0^{\frac{1}{2}} V_{jet} r dr}{\int_0^{\frac{1}{2}} r dr} = 8 \int_0^{\frac{1}{2}} V_{jet} r dr, \quad (1.10)$$

Which for the defined  $V_{jet}$  gives unit dimensionless average jet inlet velocity, which is desirable. The shape is shown in Figure 1.5.

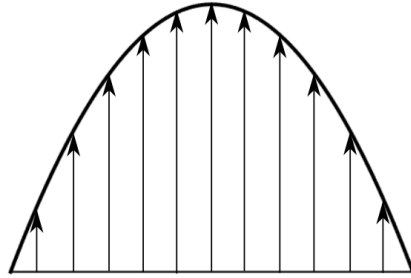


Figure 1.5: Poiseuille jet profile

### Scalar Conditions

At the crossflow inlet, the scalar concentration is set to zero, as the scalar is introduced to the domain via the jet. At the outlet, equation (1.8) is used with  $\phi = c$  to carry the scalar smoothly out of the simulation domain.

The boundary condition for the scalar within the jet inlet is

$$c(r) = C_{\max} \text{ for } r \leq \frac{1}{2}, \quad (1.11)$$

where  $C_{\max}$  is the maximum concentration of the scalar. At all other points on the upper and lower walls, a no-flux boundary condition,

$$\frac{\partial c}{\partial y} = 0, \quad (1.12)$$

is used.

### 1.2.5 Initial Conditions

Initial conditions for the velocity inside the domain are  $u(x, y, z) = U_{\text{in}}(y)$ , as given in equation 1.7, and  $v = w = 0$ . The scalar concentration is also set to zero everywhere.

## 1.3 Large-Eddy Simulation

Large-eddy simulation (LES) is a method of simulating turbulent flows that falls between Reynolds-averaged Navier–Stokes methods (RANS) and direct numerical simulation (DNS) in terms of both accuracy and computational expense. RANS involves decomposing each of the velocity components and the pressure into a temporal mean and a time-dependant fluctuation, and temporally averaging the resultant equations. It is necessary to use a model

to approximate the value of terms involving products of fluctuations, such as those produced by the non-linear terms. This is the least accurate and least expensive method for simulating turbulence. DNS involves solving the Navier–Stokes equations numerically on a grid that is fine enough to resolve all scales of the flow. This is very expensive in terms of both time and computer power. LES is performed on a grid that is too coarse to resolve all scales of turbulence. The flow scales that are larger than the grid size are resolved by the equations, and the sub-grid scales are approximated using a model. LES is less accurate than DNS as it uses a model to approximate the smallest scales of the flow, rather than resolving all scales using the Navier–Stokes equations, however it is less computationally expensive as it does not require such a fine grid. LES is more accurate than RANS in producing a time-dependant solution, but RANS is also less computationally expensive than LES, as it produces a single temporally averaged result, which only requires the equations to be solved once at each grid point, rather than a time-dependant series of results requiring the equations to be solved multiple times.

### 1.3.1 Modification of the Navier–Stokes Equations

In LES, velocity fields and other quantities are decomposed into large scales and sub-grid scales using a low-pass filter. The large-scale portion of a variable  $\phi$  is given by

$$\bar{\phi}(\mathbf{x}, t) = \int_{\Omega} G(\mathbf{r}, \mathbf{x}) \phi(\mathbf{x} - \mathbf{r}, t) d\mathbf{r}, \quad (1.13)$$

where a bold variable indicates a vector. The vector  $\mathbf{x}$  is the vector of Cartesian positions and  $\mathbf{r}$  is a vector of dummy integration variables. The function  $G$  is a low-pass filter. Applying the filter to the Navier–Stokes equations gives modified versions of equations (1.1) – (1.3),

$$\frac{\partial \bar{u}_i}{\partial t} + \bar{u}_j \frac{\partial \bar{u}_i}{\partial x_j} = -\frac{\partial \bar{P}}{\partial x_i} + \frac{1}{\text{Re}} \frac{\partial^2 \bar{u}_i}{\partial x_j \partial x_j} - \frac{\partial \tau_{ij}^{\text{SGS}}}{\partial x_j}. \quad (1.14)$$

$$\frac{\partial \bar{u}_i}{\partial x_i} = 0 \quad (1.15)$$

$$\frac{\partial \bar{c}}{\partial t} + \bar{u}_j \frac{\partial \bar{c}}{\partial x_j} = \frac{1}{\text{Pe}} \frac{\partial^2 \bar{c}}{\partial x_j \partial x_j} - \frac{\partial q_j^{\text{SGS}}}{\partial x_j} \quad (1.16)$$

where the velocities  $u_i$  and concentration  $c$  are replaced with their filtered counterparts,  $\bar{u}_i$  and  $\bar{c}$ . A number of different filters can be used in the

derivation of a large-eddy simulation scheme, however once the scheme has been derived the filtered Navier–Stokes equations are independent of the filter used [47]. Additional terms, marked with the superscript SGS are added to represent the impact of the small scale turbulence on the flow. In these equations

$$\tau_{ij}^{\text{SGS}} = \overline{u_i u_j} - \bar{u}_i \bar{u}_j \quad (1.17)$$

is the tensor of sub-grid stresses, and

$$q_j^{\text{SGS}} = \overline{u_j c} - \bar{u}_j \bar{c} \quad (1.18)$$

is the vector of sub-grid flux.

Models are used to evaluate these sub-grid terms, while larger scales are resolved directly using the Navier-Stokes equations. This allows a coarser grid to be used than is possible for direct numerical simulation, decreasing computational expense. The accuracy of the simulation depends on the model used to evaluate the sub-grid stresses and other sub-grid quantities.

### 1.3.2 Sub-grid Models

There are two main types of model used to simulate the sub-grid scales in a large-eddy simulation, eddy-viscosity models, such as the Smagorinsky model [48], Dynamic Vreman model [55] or Sigma model [42], and stretched-vortex models, such as that of Misra and Pullin [37]. Eddy viscosity models use the resolved rate-of-strain tensor and a characteristic length scale dependent on the size of the coarse grid in order to calculate the sub-grid stresses. Other sub-grid quantities such as the turbulent diffusivity and viscosity are calculated as functions of the resolved scale velocities [19].

Ghaisas et al. [19] tested a number of different models on the same problems and found that the Dynamic Smagorinsky, Stretched Vortex and Sigma models all showed strong agreement with experimental results, while the Dynamic Vreman model was highly inaccurate. When evaluating their stretched vortex model, Misra and Pullin [37] found that it performed well in modelling both decaying and forced isotropic turbulence. Using a modification of this model in a turbulent mixing layer simulation, Mattner [36] found that the simulation slightly over-predicted quantities such as the degree of mixing and the variation of composition of the mixed fluid, while still producing a reasonable solution.

In the stretched vortex model of Misra and Pullin [37] the sub-grid stresses are written as a function of the sub-grid energy and the orientation of the sub-grid vortices [37]. This model assumes that the turbulence is homogeneous, which is not the case in general but, as an approximation of the behaviour of

the sub-grid scale flow, it is sufficient. Modifications to this model have been made by others [10, 24, 32, 35, 54], to allow for its application to a wider range of systems.

The stretched vortex model has been applied to a wide range of turbulent flow types. Faddy and Pullin performed simulations of a trailing vortex wake, using direct numerical simulation at low Reynolds numbers and large-eddy simulation with the stretched vortex model developed by Misra and Pullin [37] at higher Reynolds numbers [16]. Helical instabilities were visible in both the DNS and LES simulations. It was shown that the model could produce up to 70% of the total dissipation in the system, although at longer times this percentage dropped, indicating that the flow was becoming more resolved. As suggested by Dimotakis [15], a transition from unsteady to fully turbulent flow conditions was seen at  $Re = (1-2) \times 10^4$ . Voelkl, Pullin and Chan developed a physical space version of the stretched vortex model, and tested it on simulations of both decaying isotropic turbulence and turbulent channel flow [54]. It was found from the decaying isotropic turbulence simulation that the model underestimated the sub-grid kinetic energy. The channel flow simulations showed that the model predicted the mean flow velocity profiles very well at low and moderately high Reynolds numbers, but that there was little model dissipation and poor turbulence-energy balance close to the walls of the simulation domain. Away from the walls, the model was shown to predict these values more accurately. Kosovic, Pullin and Samtaney [24] developed a stretched-vortex model to be used for simulations of compressible turbulence and applied it to decaying compressible isotropic turbulence. It was found that both the total and sub-grid turbulent kinetic energy were satisfactorily predicted when compared to a direct numerical simulation. Energy spectra from the large-eddy simulation also showed good agreement with the direct numerical simulation, although a slight build-up of energy at the highest resolved wavenumber was seen at longer simulation times. It was also found that while the model did allow for backscatter of energy from the sub-grid scales to the large scales, the amount of backscatter was underestimated. Matheou and Chung developed a buoyancy-assisted stretched vortex model, and applied it to the simulation of a number of different atmospheric boundary layers [10, 32]. Good agreement with both experimental observations and previous large-eddy simulations without buoyancy assistance was seen, although the maxima of both statistical vertical velocity variance and turbulent kinetic energy were larger than seen previously. Simulations were also used to investigate grid convergence of the model. It was found that, for this particular model, it was necessary for 90% of the turbulent kinetic energy to be resolved in the large scales to achieve convergence of solutions, whereas for previous models it was necessary to resolve only 80% of the turbulent



kinetic energy. It is necessary to reduce the grid size to achieve the increase in turbulent kinetic energy resolution.

In this work we use the stretched vortex model of Misra and Pullin [37], with modifications by Mattner [35]. The derivation of the stretched vortex model is given in Misra and Pullin [37]. In this derivation second-order structure functions are used in the calculation of a constant term,  $\mathcal{K}_0 \varepsilon^{\frac{2}{3}}$ , which is involved in the definition of the energy spectrum. Mattner used the local energy balance between the large and sub-grid scales to evaluate this same term without the need to use structure functions [35]. Mattner's method ensures that the energy transfer from the large to the sub-grid scales matches the energy that is dissipated from the sub-grid scales.

According to the stretched vortex model, the sub-grid scale stress is

$$\tau_{ij}^{\text{SGS}} = K(\delta_{ij} - e_i^v e_j^v), \quad (1.19)$$

and the sub-grid flux is

$$q_j^{\text{SGS}} = -\frac{1}{2} \Delta K^{\frac{1}{2}} (\delta_{ij} - e_i^v e_j^v) \frac{\partial \bar{c}}{\partial x_j}. \quad (1.20)$$

In these equations,  $\delta_{ij}$  is the Kronecker delta,  $e_i^v$  are the components of a unit vector aligned with the sub-grid vortex axis,  $\Delta$  is the grid spacing and

$$K = \int_{\kappa_c}^{\infty} \frac{4}{3} \frac{\bar{S}_{ij} \bar{S}_{ij}}{\kappa^{\frac{4}{3}}} \kappa^{-\frac{5}{3}} e^{\lambda_\nu^2 \kappa^2} d\kappa, \quad (1.21)$$

where  $\kappa = \pi/\Delta$  is the cutoff wavenumber, and  $\lambda_\nu^2 = 2\nu/3|a|$ ,  $a$  being a constant chosen to balance the rate of transfer of energy from the large to the sub-grid scales with the sub-grid dissipation [35].

## 1.4 Julia

Julia is an open-source computational language that was released in February 2012. It was developed to address a number of issues surrounding scientific and mathematical computing. One of these issues is the developer-user divide, due to the underlying code being written at a level too high to be understood or manipulated by the average programmer. Another is the two language problem, that is prototyping and debugging a code by a programmer using a less powerful but easier to understand language, after which the code is rewritten in a more powerful language for data manipulation.

It is often thought that there are parts of a computational language that are for the developers alone, parts that are too complex for a user to understand or manipulate. The developers of Julia have attempted to shake

this idea by writing all of the standard Julia library in Julia itself, so it can be understood as easily by users as developers. As Julia is an open source language, user modifications and additions are welcome. Even in the first 6 months after its release, a good proportion of new additions to the function library were provided by “new” users outside of the development team [2], and this has continued to the present day. Graphical packages that allow the production of graphs and images have also been developed by users. This implies that the language is easy to learn and productive, as it aimed to be.

There are two main types of computational languages that are used in scientific and mathematical computing. The first of these are dynamically typed languages, such as MATLAB or R. These languages do not require assigning types to variables, making codes simpler and more convenient to write. This is good for testing and code development, however the consequence of this simplicity is a slower and less efficient code that struggles with large data sets and computationally expensive manipulations. The alternative to a dynamically typed language is a statically typed language, such as Fortran or C. In these languages, it is necessary to declare types for all variables before they are assigned values. While this can result in more complex code, the prior knowledge of data types allows codes written in these languages to be more efficient. Julia attempts to span the divide between these two language types, with the ease of use of a dynamically typed language while approaching the efficiency and performance of a statically typed language. It is not necessary to declare the types of variables in Julia, although it is possible, as the type will be determined by context. Julia’s inbuilt functions have also been developed to take in variables of many different types, and evaluate them in the same way, recognising their similarities rather than their differences. In cases where this is not possible, the type of a variable is evaluated and the most efficient algorithm to manipulate data of each type is used. This allows for the production of a code that is as efficient as possible at each step.

Another of Julia’s features which contributes to its efficiency is its parallelisation capability, which has been written into the language from the beginning. This parallelisation ability has three levels of increasing complexity and efficiency, parallelisation within a single CPU, multi-threading, where operations are performed on arrays distributed between multiple CPUs on a single machine, and distributed memory programming, where arrays are split between multiple machines, each with multiple CPUs [1]. These methods are applied using a built in message based multi-processing system that is part of the standard library of the language [2].

Julia’s efficiency has been tested against a number of other languages, both statically and dynamically typed, with execution speeds of a number of

data manipulations on both scalars and arrays measured and compared to that of C++. It was found that Julia is not as efficient as C for many of the tested operations, but is on par for some, and consistently performs better than other dynamically typed languages, such as JavaScript and Python [1]. This suggests that the developers claim of it approaching the efficiency of statically typed languages is valid.

The community of Julia users has expanded greatly since its public release in 2012. From the beginning of 2016 until the beginning of 2017 the number of packages developed for the Julia language increased by 72%, while the number of downloads of the Julia language increased by 161% [11].

Julia was chosen as the language for this investigation to determine its usefulness when applied to fluid dynamics simulations. It was also chosen due to its straightforward code parallelisation process, which could reduce the computational time necessary to perform simulations. Unfortunately, we were not able to implement this within the timeframe of the project.

## 1.5 Thesis Summary

The primary objective of the present work is to produce and validate a code in the computational language Julia to perform a large-eddy simulation of a jet in crossflow, using the stretched-vortex sub-grid model. Simulations produced by this code are used to determine the effect of velocity ratio on the flow, as well as the effect of the sub-grid model at low and moderate Reynolds numbers.

In Chapter 2 a detailed description of the numerical methods used is presented. The numerical methods are tested through the direct numerical simulation of a Taylor–Green vortex, which has an analytic solution. Visualisations of general flow properties of a jet in crossflow are also presented in Chapter 2.

In Chapter 3 the code is tested further by comparison of simulation results to the published results of experimental studies, LES and DNS. An in depth comparison with an LES performed using different numerical methods but the same sub-grid model is also presented.

In Chapters 4 and 5 the results of a number of LES are presented. In Chapter 4 the Reynolds number and boundary-layer thickness are held constant while the velocity ratio is varied. This is used to investigate the effect of velocity ratio on flow characteristics such as the jet trajectory, mixing, spectra and dissipation. It is found that a jet with a higher velocity ratio will penetrate more deeply into the crossflow, and that at higher velocity ratios the flow as a whole will contain more energy. In Chapter 5 LES and

DNS are performed at the same grid resolution for low and high Reynolds numbers. The effects of the sub-grid model on velocity and scalar concentration profiles, trajectories and spectra are investigated. It is found that at low Reynolds number there is little difference between an LES and a DNS, as the sub-grid scale model switches off, and that at higher Reynolds numbers the sub-grid scale model has a strong impact on the magnitude and distribution of the energy present in the system.

A summary including conclusions and suggested future work is presented in Chapter 6.

# Chapter 2

## Numerical Methods

### 2.1 Considerations

When using numerical methods to simulate any system, there are a number of considerations that must be made. A simulation must be a sufficiently accurate representation of the system, however high accuracy methods often require a large amount of computational power. It is often necessary to sacrifice some accuracy in order to have the simulation run in a reasonable amount of time. It is also important to consider the appropriateness of any models used for the system in question. For example, a large-eddy simulation of a flow that interacts closely with a boundary should use a model which takes boundary effects into consideration. Finally, it is important, particularly for physical systems, that properties such as mass and momentum are conserved, and that numerical dissipation is kept to a minimum, to ensure that the simulation is as physically representative as possible.

The size of the error present in a solution produced by a central finite-difference scheme decreases as the order of the scheme increases. Desjardins et al. [14] found that, for a number of test cases, moving from second to fourth order numerical methods provided a large increase in accuracy, while the increase in accuracy caused by increasing from fourth to sixth order was significantly smaller. Furthermore, the computational cost was found to double in each case. A modified wavenumber analysis, in which finite-difference methods are used to represent the first derivative of an equation of the form

$$\phi(x, t) = e^{i\kappa x}, \quad (2.1)$$

and the resulting formula is rearranged into a form

$$\frac{d\phi}{dx} = i\kappa e^{i\kappa x}, \quad (2.2)$$

where  $\kappa'$  is the modified wavenumber shown in Figure 2.1 and  $\Delta$  is the grid spacing, can be used to analyse the accuracy of different numerical approximations of the first derivative. The modified wavenumber is the multiplier produced by finite difference methods that is equivalent to the wavenumber that appears in exact differentiation of exponential terms. This form of the approximation to the derivative would be equivalent to the exact derivative if  $\kappa' = \kappa$ . It can be seen that a fourth-order scheme, shown as a blue line with  $\kappa'\Delta = (4/3)\sin(\kappa\Delta) - (1/6)\sin(2\kappa\Delta)$ , captures more of the high wavenumber region accurately than the second-order scheme, shown as a green line with  $\kappa'\Delta = \sin(\kappa\Delta)$ . A sixth order central-difference method, the red line with  $\kappa'\Delta = (1/30)(45\sin(\kappa\Delta) - 9\sin(2\kappa\Delta) + \sin(3\kappa\Delta))$ , shows further improvement, but the increase is significantly smaller than seen when going from second to fourth order. Fourier spectral methods, shown as the dashed line with  $\kappa'\Delta = \kappa\Delta$ , give the most accurate solutions, and give exact solutions for exponential equations such as that used here. However, the use of some spectral methods requires particular conditions, such as periodic boundaries for Fourier spectral methods, which are not always applicable to the flow system.

It is also desirable for the finite-difference schemes to conserve not only mass and momentum but also kinetic energy, particularly for turbulent flows where numerical dissipation of energy can lead to a reduction in turbulent characteristics. Morinishi et al. [39] developed a fourth order accurate finite-difference scheme for solving the Navier-Stokes equations for incompressible flows which discretely conserves mass, momentum and kinetic energy on a staggered grid. The staggered grid also prevents zigzagging in the pressure field, a phenomenon which numerically satisfies conservation of mass in a way that is not physically possible. This scheme was initially developed only for constant density flows, however it was extended by Desjardins et al. [14] to also be applicable to variable density flows.

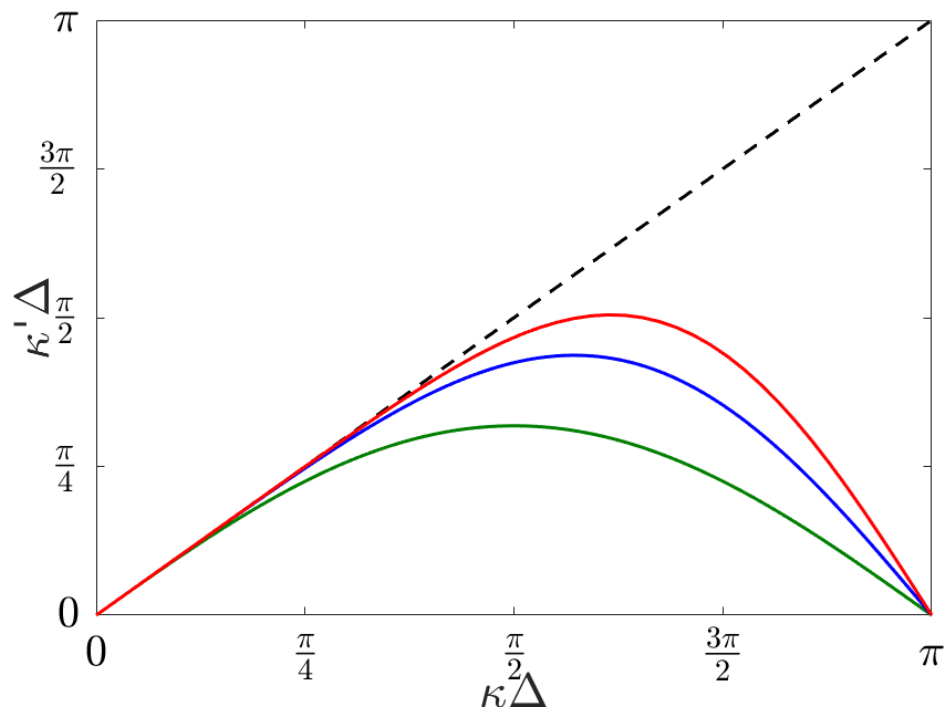


Figure 2.1: Modified wavenumber ( $\kappa'$ ) vs wavenumber ( $\kappa$ ) for second-order central-difference (green), fourth order central-difference (blue), sixth order central-difference (red) and spectral methods (black dashed line).  $\Delta$  is the grid spacing.

## 2.2 Spatial Discretisation

We approximate the solution of the Navier–Stokes equations by first discretising the spatial derivatives, then applying a time-stepping algorithm to track how the velocities change over time. The physical-space variables are first transformed into wavenumber-space variables by taking the Fourier transform of all variables in the cross-stream direction. This direction is chosen as it is assumed to be periodic. The discrete Fourier transform of a function  $\phi(x, y, z, t)$  is

$$\phi(x, y, z, t) = \sum_{n=-\frac{N_z}{2}+1}^{\frac{N_z}{2}} \hat{\phi}(x, y, 2\pi n/\ell, t) e^{i(2\pi n/\ell)z}, \quad (2.3)$$

where  $\hat{\phi}$  is a Fourier coefficient,  $n$  is the wavenumber,  $N_z$  is the number of physical-space modes in the  $z$  direction or the number of discrete wavenumbers, and  $\ell$  is the length of the domain in the  $z$  direction, in this case 10. From here we will use the substitutions  $2\pi n/\ell = \kappa$  and

$$\sum_{n=-\frac{N_z}{2}+1}^{\frac{N_z}{2}} = \sum_{\kappa} \quad (2.4)$$

for simplicity. In these equations  $\phi$  can be any dependent variable.

Using equation (2.3) the Navier–Stokes equations are rewritten as

$$\frac{\partial \hat{u}}{\partial t} + \hat{\mathcal{N}}_1 = -\frac{\partial \hat{P}}{\partial x} + \frac{1}{\text{Re}} \left( \frac{\partial^2 \hat{u}}{\partial x^2} + \frac{\partial^2 \hat{u}}{\partial y^2} - \kappa^2 \hat{u} \right) - \frac{\partial \hat{\tau}_{1,1}}{\partial x} - \frac{\partial \hat{\tau}_{1,2}}{\partial y} - \iota \kappa \hat{\tau}_{1,3} \quad (2.5)$$

$$\frac{\partial \hat{v}}{\partial t} + \hat{\mathcal{N}}_2 = -\frac{\partial \hat{P}}{\partial y} + \frac{1}{\text{Re}} \left( \frac{\partial^2 \hat{v}}{\partial x^2} + \frac{\partial^2 \hat{v}}{\partial y^2} - \kappa^2 \hat{v} \right) - \frac{\partial \hat{\tau}_{2,1}}{\partial x} - \frac{\partial \hat{\tau}_{2,2}}{\partial y} - \iota \kappa \hat{\tau}_{2,3} \quad (2.6)$$

$$\frac{\partial \hat{w}}{\partial t} + \hat{\mathcal{N}}_3 = -\iota \kappa \hat{P} + \frac{1}{\text{Re}} \left( \frac{\partial^2 \hat{w}}{\partial x^2} + \frac{\partial^2 \hat{w}}{\partial y^2} - \kappa^2 \hat{w} \right) - \frac{\partial \hat{\tau}_{3,1}}{\partial x} - \frac{\partial \hat{\tau}_{3,2}}{\partial y} - \iota \kappa \hat{\tau}_{3,3} \quad (2.7)$$

$$\frac{\partial \hat{u}}{\partial x} + \frac{\partial \hat{v}}{\partial y} + \iota \kappa \hat{w} = 0, \quad (2.8)$$

$$\frac{\partial \hat{c}}{\partial t} + \hat{\mathcal{N}}_c = \frac{1}{Pe} \left( \frac{\partial^2 \hat{c}}{\partial x^2} + \frac{\partial^2 \hat{c}}{\partial y^2} - \kappa^2 \hat{c} \right) - \frac{\partial q_1^{\text{SGS}}}{\partial x} - \frac{\partial q_2^{\text{SGS}}}{\partial y} - \iota \kappa q_3^{\text{SGS}}, \quad (2.9)$$

respectively, with  $\hat{\mathcal{N}}_i$  and  $\hat{\mathcal{N}}_c$  representing the non-linear terms of the Navier–Stokes and scalar transport equations. The calculation of these terms will be discussed in section 2.2.5 ahead. The transformation into wavenumber space



means that only derivatives in the  $x$  and  $y$  directions are calculated using finite-difference methods, while derivatives in the  $z$  direction are calculated by spectral methods. All wavenumber based analysis, such as energy spectra, is also performed in the  $z$  direction.

All calculations other than the evaluation of the non-linear terms and the calculation of the sub-grid stresses and flux are performed on the wavenumber-space variables. Where necessary, the variables are transformed to physical space by the application of the inverse Fourier transform.

### 2.2.1 Discretised Domain and Staggered Grid

When discretising the domain, it was decided that a series of two-dimensional grid systems, layered in the  $z$  direction, rather than a three-dimensional cell system, would be used for the storage of data. As such, the discretised domain is made up of a number of  $xy$  slices, as shown in Figure 2.2. This was chosen to remove the need for interpolation in the  $z$  direction. In physical space, the size of the grid used is  $200 \times 100 \times 100$ , which is fairly coarse but was chosen to allow for reasonably fast simulation times. By transforming from physical-space to wavenumber-space it is possible to reduce the size of the grid to  $200 \times 100 \times 51$ , as we can discard the slices that pertain to the negative wavenumbers by assuming that the physical solution to the Navier–Stokes solution is real, and thus that the Fourier coefficients of the negative wavenumber variables will be complex conjugates of those of the equivalent positive wavenumber coefficients. This simplifies many calculations, as it is only necessary to work with the positive wavenumbers.

Within each  $xy$  slice, a staggered grid format is used, in which the three components of velocity are stored at different points within a cell. As shown in Figure 2.3 the streamwise component of velocity ( $u$ ) is located at the centre of the left and right edges of each cell, while the transverse component ( $v$ ) is located at the centre of the upper and lower edges. The cross-stream velocity ( $w$ ), along with the pressure ( $P$ ) and the scalar concentration ( $c$ ) is located at the centre of each two dimensional cell. The staggered grid has been shown by Morinishi [39] to conserve discrete momentum and energy a priori in a second-order finite-difference scheme. It also prevents oscillatory solutions as, when calculating derivatives using a central-difference method, values at adjacent points are used rather than those at alternate grid points [25].

Using the staggered grid with finite-difference approximations to  $x$  and  $y$  derivatives leads to different terms being evaluated at different points on the grid. Interpolation and first derivative calculations lead to a shift of half a cell in the direction of the operation, while calculating a second derivative retains the original location of the variable. Locations of common terms

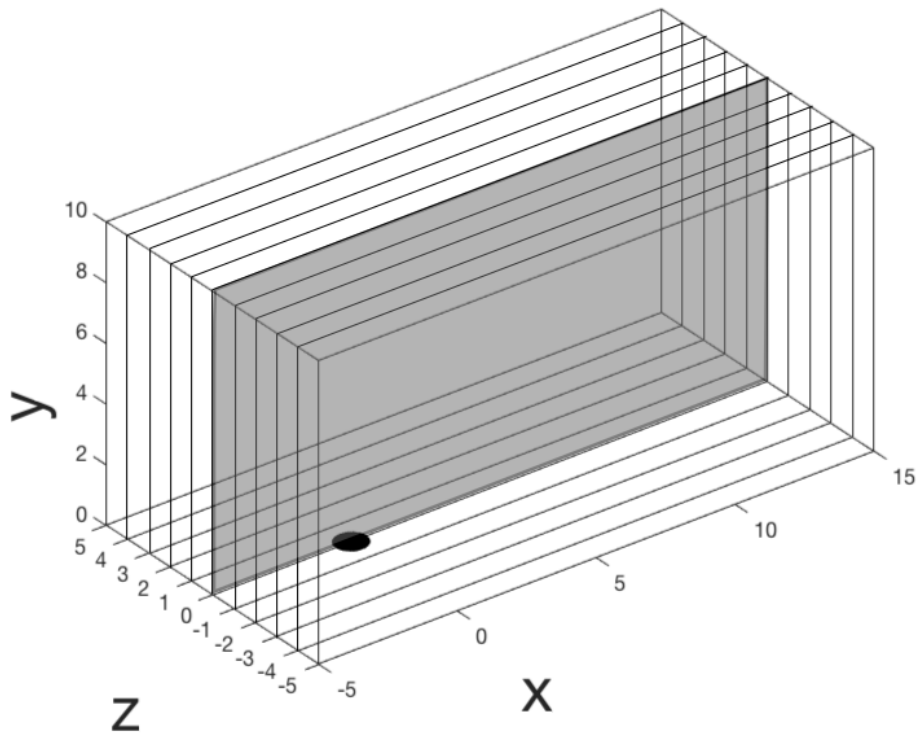
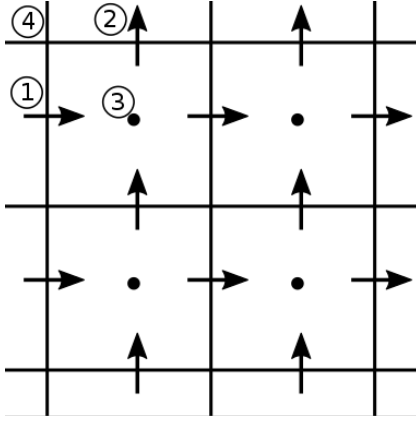


Figure 2.2: Simulation domain with one slice shaded. For any particular value of  $z$ , in this case  $z = 0$ , all data points are located within the indicated plane.

within a cell are shown in Figure 2.3. Wavenumber-space terms are stored in the same positions as their physical-space equivalents.



1.  $u, u_j \frac{\partial u}{\partial x_j}, \frac{\partial^2 u}{\partial x_j \partial x_j}, \frac{\partial u}{\partial z}, \frac{\partial w}{\partial x}, \frac{\partial c}{\partial x}$
2.  $v, u_j \frac{\partial v}{\partial x_j}, \frac{\partial^2 v}{\partial x_j \partial x_j}, \frac{\partial v}{\partial z}, \frac{\partial w}{\partial y}, \frac{\partial c}{\partial y}$
3.  $w, u_j \frac{\partial w}{\partial x_j}, \frac{\partial^2 w}{\partial x_j \partial x_j}, \frac{\partial w}{\partial z},$   
 $c, u_j \frac{\partial c}{\partial x_j}, \frac{\partial^2 c}{\partial x_j \partial x_j}, \frac{\partial c}{\partial z},$   
 $\frac{\partial u}{\partial x}, \frac{\partial v}{\partial y}, P, \tau_{ij}, q_{ij}$
4.  $\frac{\partial u}{\partial y}, \frac{\partial v}{\partial x}$

Figure 2.3: Four staggered grid cells. Positions where different terms are calculated are as marked.

### 2.2.2 Interpolation

When using a staggered grid it is necessary to interpolate some quantities during operations, so that they are available for computations at locations other than their ‘home’. A simple, second-order-accurate scheme is used for these interpolation operations, of the form

$$\overline{\phi}^x(x + \frac{\Delta x}{2}, y, \kappa) = \frac{\phi(x + \Delta x, y, \kappa) + \phi(x, y, \kappa)}{2}, \quad (2.10)$$

where the superscript attached to the overline indicates the direction of the interpolation, in this case the  $x$  direction. This operation approximates the value of  $\phi$  midway between  $\phi(x, y, \kappa)$  and  $\phi(x + \Delta x, y, \kappa)$ . A similar method can be used to interpolate values in the  $y$  direction, indicated by a superscript  $y$ . At no point is it necessary to interpolate in the  $z$  direction, as the grid is not staggered in this direction. It is sometimes necessary to apply the operation multiple times, in different directions, to find the value of  $\phi$  at the position where it is needed. The same operation can be applied to wavenumber-space variables.

### 2.2.3 First Derivatives

The first derivative of a variable  $\phi$  in the streamwise direction is evaluated using a second-order central-difference method, with the discrete approximation to the derivative indicated by the use of a  $\delta$  rather than a  $\partial$ . In the  $x$  direction, this is

$$\frac{\partial \phi}{\partial x} \approx \frac{\delta \phi}{\delta x}(x + \frac{\Delta x}{2}, y, \kappa) = \frac{\phi(x + \Delta x, y, \kappa) - \phi(x, y, \kappa)}{\Delta x}. \quad (2.11)$$

This method is not location preserving on a staggered grid, and the derivative is stored at the grid point midway between  $\hat{\phi}(x, y, \kappa)$  and  $\hat{\phi}(x + \Delta x, y, \kappa)$ . A similar method can be used in the  $y$  direction, resulting in a point midway between  $\hat{\phi}(x, y, \kappa)$  and  $\hat{\phi}(x, y + \Delta y, \kappa)$ . This method of calculating discrete derivatives can also be applied to wavenumber-space variables as necessary.

### 2.2.4 Second Derivatives

The second derivative of a variable  $\phi$  in the streamwise direction is calculated using a second-order central-difference method, with the discrete approximation to the derivative again represented by a  $\delta$  rather than a  $\partial$ . In the  $x$  direction the discrete derivative is given as

$$\frac{\partial^2 \phi}{\partial x^2} \approx \frac{\delta^2 \phi}{\delta x^2}(x, y, \kappa) = \frac{\phi(x + \Delta x, y, \kappa) - 2\phi(x, y, \kappa) + \phi(x - \Delta x, y, \kappa)}{\Delta x^2}, \quad (2.12)$$

which is equivalent to applying the discrete first-order derivative operation twice. A similar method is used for  $y$  direction second derivatives. This method is location preserving, so it is not necessary to perform any interpolation operations on these terms. This method can also be applied to wavenumber-space variables as necessary.

### 2.2.5 Non-Linear Terms

The non-linear convective terms,  $\mathcal{N}_i$  and  $\mathcal{N}_c$ , are calculated in physical space, then converted to wavenumber space. This is done for efficiency. Calculation of the non-linear terms in wavenumber space involves the evaluation of a double sum, taking  $N_z^2$  operations, where  $N_z$  is the number of points in the cross-stream direction. Converting to and from physical space by way of the Fast Fourier Transform takes  $\mathcal{O}(N_z \log_2 N_z)$  operations each, and in physical space the multiplication of terms takes  $N_z$  operations. For sufficiently large  $N_z$ , fewer operations are needed for a physical space calculation.

It is necessary, however, to consider the errors produced when calculating the non-linear terms in physical space and converting them to wavenumber space. If discrete Fourier approximations of two functions  $f(x)$  and  $g(x)$  are multiplied together, the resulting product is

$$f(x)g(x) = \sum_{\kappa} \sum_{\bar{\kappa}} \hat{f}(\kappa) \hat{g}(\bar{\kappa}) e^{i(\kappa + \bar{\kappa})x} \quad (2.13)$$

where for some values of  $\kappa$  and  $\bar{\kappa}$  the value of  $(\kappa + \bar{\kappa})$  will be outside the range of discrete wavenumbers used,  $\frac{\pi(-N_z + 2)}{\ell} \leq \kappa \leq \frac{\pi N_z}{\ell}$ . In wavenumber space

calculations these wavenumbers are removed from the calculations, however in transforming the resulting term from physical space to wavenumber space these high wavenumbers are aliased into lower wavenumbers, within the range of discrete wavenumbers used [3]. This can lead to numerical instability. To counteract this, we calculate the convective terms in skew-symmetric form, as given by Morinishi et al. [39], which has been shown to minimise aliasing errors [3, 60]. This form of the terms is calculated by taking the average of the advective and divergence forms of the non-linear terms

$$\mathcal{N}_i = (\text{Skew})_i = \frac{1}{2}(\text{Div})_i + \frac{1}{2}(\text{Adv})_i = \frac{1}{2}u_j \frac{\partial u_i}{\partial x_j} + \frac{1}{2} \frac{\partial u_i u_j}{\partial x_j}. \quad (2.14)$$

This form is energy conserving a priori for a fully second-order central-difference method [39], however it may not be in my hybrid finite-difference spectral method. Where necessary, cross-stream derivatives are calculated in wavenumber space before being transformed into physical space to be used in the following calculations. Streamwise and transverse derivatives are calculated in physical space. Once the non-linear terms have been calculated, they are transformed back into wavenumber space before being used in the solution of the Navier–Stokes equations.

The main complication present in calculating the non-linear terms on a staggered grid is shifting the component terms to a shared location before they can be multiplied. The interpolation steps necessary for the calculation of the advective and divergence forms are described below, along with the methods of calculating these terms.

### Advective Form

Streamwise and transverse derivatives are calculated in physical space using the method given in section 2.2.3. This produces derivatives that are located at cell centres or corners, so it is necessary to interpolate the physical velocity components to the same points using the method given in section 2.2.2. These interpolated values are then multiplied with the derivatives, and the resulting values interpolated back to the correct locations.

For example, the streamwise advective term  $u_j \frac{\partial u}{\partial x_j}$  is calculated as

$$u_j \frac{\partial u}{\partial x_j} = \overline{\left(\bar{u}^x \frac{\delta u}{\delta x}\right)^x} + \overline{\left(\bar{v}^x \frac{\delta u}{\delta y}\right)^y} + \bar{w}^x \sum_{\kappa} i\kappa \hat{u} e^{i\kappa z}. \quad (2.15)$$

The resulting term, located at the left and right cell edges, is transformed back into wavenumber space before being used in equation (2.5). Similar methods can be used to calculate advective terms for the other two directions, although different interpolation operations are required.

## Divergence Form

In this form, the components of velocity are first multiplied, then the derivative of the product is taken. As before, it is necessary to interpolate the components of physical velocity to a shared position before multiplication, using the method given in section 2.2.2.

For example, the streamwise divergence term  $\frac{\partial uu_j}{\partial x_j}$  is calculated as

$$\frac{\partial uu_j}{\partial x_j} = \overline{\left(\frac{\delta uu}{\delta x}\right)^x} + \frac{\delta(\bar{u}^y \bar{v}^x)}{\delta y} + \sum_{\kappa} i\kappa \overline{(\bar{u}^x w)^x} e^{i\kappa z}. \quad (2.16)$$

The resulting term, again located at left and right cell edges, is transformed back into wavenumber space before being used in equation (2.5). Similar methods can be used to calculate the transverse and cross stream terms, although different interpolation operations are required.

## 2.3 Temporal Integration

### 2.3.1 Adam–Bashforth–Moulton Predictor–Corrector

The evolution equations (2.5), (2.6), (2.7) and (2.9) are solved by the third-order, constant timestep, Adam–Bashforth–Moulton (ABM3) scheme [57]. For the model problem

$$\frac{\partial y}{\partial t} = f(t, y), \quad (2.17)$$

this is given as

$$y^{(*)} = y^{(n)} + \frac{\Delta t}{2} [3f^{(n)} - f^{(n-1)}], \quad (2.18)$$

$$y^{(n+1)} = y^{(*)} + \frac{5\Delta t}{12} [f^{(*)} - 2f^{(n)} + f^{(n-1)}], \quad (2.19)$$

where  $n$  is the time step index,  $\Delta t = t^{(n+1)} - t^{(n)}$ ,  $f^{(n)} = f(y^{(n)}, t^{(n)})$  and  $f^{(*)}$  is the function  $f$  evaluated at the point  $y^{(*)}$ .

To use the ABM3 scheme to solve the Navier–Stokes equations and ensure that the continuity equation is satisfied, we first split the pressure term, and write equations (2.5) - (2.7) in the form

$$\frac{\partial \hat{u}}{\partial t} = \Lambda_1 - \frac{\partial \hat{P}}{\partial x}, \quad (2.20)$$

$$\frac{\partial \hat{v}}{\partial t} = \Lambda_2 - \frac{\partial \hat{P}}{\partial y}, \quad (2.21)$$

$$\frac{\partial \hat{w}}{\partial t} = \Lambda_3 - \iota\kappa \hat{P}, \quad (2.22)$$

where

$$\Lambda_1 = -\hat{\mathcal{N}}_1 + \frac{1}{\text{Re}} \left( \frac{\partial^2 \hat{u}}{\partial x^2} + \frac{\partial^2 \hat{u}}{\partial y^2} - \kappa^2 \hat{u} \right) - \frac{\partial \hat{\tau}_{1,1}}{\partial x} - \frac{\partial \hat{\tau}_{1,2}}{\partial y} - \iota\kappa \hat{\tau}_{1,3}, \quad (2.23)$$

$$\Lambda_2 = -\hat{\mathcal{N}}_2 + \frac{1}{\text{Re}} \left( \frac{\partial^2 \hat{v}}{\partial x^2} + \frac{\partial^2 \hat{v}}{\partial y^2} - \kappa^2 \hat{v} \right) - \frac{\partial \hat{\tau}_{2,1}}{\partial x} - \frac{\partial \hat{\tau}_{2,2}}{\partial y} - \iota\kappa \hat{\tau}_{2,3}, \quad (2.24)$$

$$\Lambda_3 = -\hat{\mathcal{N}}_3 + \frac{1}{\text{Re}} \left( \frac{\partial^2 \hat{w}}{\partial x^2} + \frac{\partial^2 \hat{w}}{\partial y^2} - \kappa^2 \hat{w} \right) - \frac{\partial \hat{\tau}_{3,1}}{\partial x} - \frac{\partial \hat{\tau}_{3,2}}{\partial y} - \iota\kappa \hat{\tau}_{3,3}. \quad (2.25)$$

Applying the predictor (2.18) to these equations and simplifying gives

$$\hat{u}^{(*)} = \Phi_1^{(*)} - \Delta t \frac{\partial \bar{P}^{(*)}}{\partial x}, \quad (2.26)$$

$$\hat{v}^{(*)} = \Phi_2^{(*)} - \Delta t \frac{\partial \bar{P}^{(*)}}{\partial y}, \quad (2.27)$$

$$\hat{w}^{(*)} = \Phi_3^{(*)} - \iota\kappa \Delta t \bar{P}^{(*)} \quad (2.28)$$

where

$$\Phi_1^{(*)} = \hat{u}^{(n)} + \frac{\Delta t}{2} \left[ 3\Lambda_1^{(n)} - \Lambda_1^{(n-1)} \right], \quad (2.29)$$

$$\Phi_2^{(*)} = \hat{v}^{(n)} + \frac{\Delta t}{2} \left[ 3\Lambda_2^{(n)} - \Lambda_2^{(n-1)} \right], \quad (2.30)$$

$$\Phi_3^{(*)} = \hat{w}^{(n)} + \frac{\Delta t}{2} \left[ 3\Lambda_3^{(n)} - \Lambda_3^{(n-1)} \right], \quad (2.31)$$

and

$$\bar{P}^{(*)} = \frac{1}{2} \left[ 3\hat{P}^{(n)} - \hat{P}^{(n-1)} \right]. \quad (2.32)$$

Taking the divergence of the vector  $(\hat{u}^{(*)}, \hat{v}^{(*)}, \hat{w}^{(*)})$  and applying the incompressibility constraint (2.8) gives

$$\frac{\partial^2 \bar{P}^{(*)}}{\partial x^2} + \frac{\partial^2 \bar{P}^{(*)}}{\partial y^2} - \kappa^2 \bar{P}^{(*)} = \frac{1}{\Delta t} \left( \frac{\partial \Phi_1^{(*)}}{\partial x} + \frac{\partial \Phi_2^{(*)}}{\partial y} + \iota\kappa \Phi_3^{(*)} \right). \quad (2.33)$$

We solve (2.33) subject to the boundary conditions given in section 1.2.4, using the method that will be described shortly in section 2.5, and substitute

$\bar{P}^{(*)}$  into (2.28) to obtain  $u^{(*)}$ ,  $v^{(*)}$  and  $w^{(*)}$ . This completes the predictor step.

Applying the corrector, (2.19), and simplifying, gives

$$\hat{u}^{(n+1)} = \Phi_1 - \Delta t \frac{\partial \bar{P}}{\partial x} \quad (2.34)$$

$$\hat{v}^{(n+1)} = \Phi_2 - \Delta t \frac{\partial \bar{P}}{\partial y} \quad (2.35)$$

$$\hat{w}^{(n+1)} = \Phi_3 - \nu \kappa \Delta t \bar{P} \quad (2.36)$$

where

$$\Phi_1 = \hat{u}^{(*)} + \frac{5\Delta t}{12} \left[ \Lambda_1^{(*)} - 2\Lambda_1^{(n)} + \Lambda_1^{(n-1)} \right], \quad (2.37)$$

$$\Phi_2 = \hat{v}^{(*)} + \frac{5\Delta t}{12} \left[ \Lambda_2^{(*)} - 2\Lambda_2^{(n)} + \Lambda_2^{(n-1)} \right], \quad (2.38)$$

$$\Phi_3 = \hat{w}^{(*)} + \frac{5\Delta t}{12} \left[ \Lambda_3^{(*)} - 2\Lambda_3^{(n)} + \Lambda_3^{(n-1)} \right], \quad (2.39)$$

and

$$\bar{P} = \frac{5}{12} \left[ \bar{P}^{(*)} - 2\hat{P}^{(n)} + \hat{P}^{(n-1)} \right]. \quad (2.40)$$

Again, taking the divergence and applying the incompressibility constraint gives

$$\frac{\partial^2 \bar{P}}{\partial x^2} + \frac{\partial^2 \bar{P}}{\partial y^2} - \kappa^2 \bar{P} = \frac{1}{\Delta t} \left( \frac{\partial \Phi_1}{\partial x} + \frac{\partial \Phi_2}{\partial y} + \nu \kappa \Phi_3 \right). \quad (2.41)$$

Solving (2.41) subject to the boundary conditions given in section 1.2.4 gives  $\bar{P}$ , which can be substituted into (2.36) to obtain  $\hat{u}^{(n+1)}$ ,  $\hat{v}^{(n+1)}$  and  $\hat{w}^{(n+1)}$ . This completes the corrector step.

### Stability Analysis

To obtain a rough estimate of the stability of our numerical method, we analyse the stability of the Adam–Bashforth–Moulton predictor corrector by first applying both steps of this method to the model problem

$$\frac{dy}{dt} = \lambda y, \quad (2.42)$$

giving

$$y^{(n+1)} = y^{(n)} \left( 1 + \frac{13}{12} \lambda \Delta t + \frac{5}{8} (\lambda \Delta t)^2 \right) + y^{(n-1)} \left( \frac{1}{12} \lambda \Delta t + \frac{5}{24} (\lambda \Delta t)^2 \right). \quad (2.43)$$



The solution of the differential equation (2.42) is  $y(t^{(n)}) = C\sigma^n$ , where  $\sigma = e^{\lambda\Delta t}$ . By substituting this solution into (2.43), we arrive at

$$\sigma^2 - \sigma \left( 1 + \frac{13}{12}\lambda\Delta t + \frac{5}{8}(\lambda\Delta t)^2 \right) + \left( \frac{1}{12}\lambda\Delta t + \frac{5}{24}(\lambda\Delta t)^2 \right) = 0, \quad (2.44)$$

which has solutions

$$\sigma = \frac{\left( 1 + \frac{13}{12}\lambda\Delta t + \frac{5}{8}(\lambda\Delta t)^2 \right)}{2} \pm \frac{\sqrt{\left( 1 + \frac{13}{12}\lambda\Delta t + \frac{5}{8}(\lambda\Delta t)^2 \right)^2 - 4\left( \frac{1}{12}\lambda\Delta t + \frac{5}{24}(\lambda\Delta t)^2 \right)}}{2}. \quad (2.45)$$

If the real part of  $\lambda$  is positive,  $|\sigma| > 1$ , which leads to growth of the error, and instability. If the real part of  $\lambda$  is negative,  $|\sigma| < 1$ , so the error decays and the solution is stable. By investigating the region where  $|\sigma| = 1$ , we can see where solutions are stable and unstable. Figure 2.4 shows the stability boundary, where  $|\sigma| = 1$ . The interior of this region is stable, and the exterior is unstable.

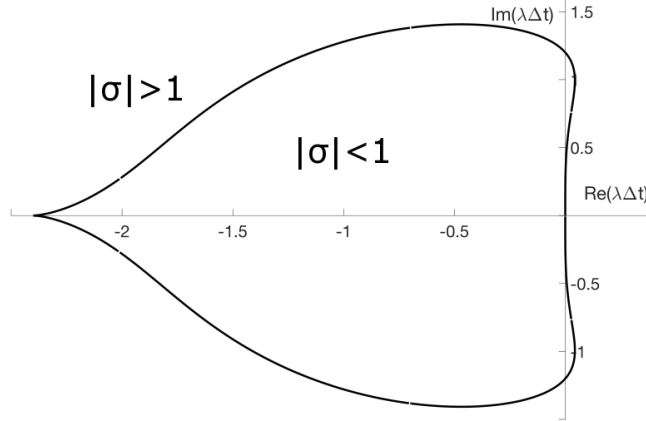


Figure 2.4: Stability boundary of Adam–Bashforth–Moulton method, for complex values of  $\lambda\Delta t$ .

Approximate stability criteria are obtained by analysing the one-dimensional advection and diffusion equations subject to  $2\pi$ -periodic boundary conditions. We also investigate the Fourier transform method of calculating the derivatives rather than the finite-difference method, because the maximum

modified wavenumber of the first derivative is higher when using this method, as can be seen in Figure 2.1, also leading to conservative stability criteria.

For advective stability, we investigate the basic advection PDE,

$$\frac{\partial u}{\partial t} = -c \frac{\partial u}{\partial x}, \quad (2.46)$$

which has  $c$  as a positive real constant. Setting  $u(x, t) = \hat{u}(t)e^{i\kappa x}$ , where  $\kappa$  is the wavenumber, and simplifying, we achieve the form

$$\frac{d\hat{u}}{dt} = \lambda \hat{u}, \quad (2.47)$$

where  $\lambda = -ci\kappa$ . We assume that  $\kappa$  is positive without loss of generality. In Figure 2.4 above, the stability boundary crosses the imaginary axis at  $\pm 1.2$ . Thus we set

$$c\kappa\Delta t \leq 1.2, \quad (2.48)$$

where in the worst case,  $\kappa = \frac{N}{2} = \frac{\pi}{\Delta x}$ . The condition for advective stability [38] is that

$$\gamma_{adv.} = \frac{c\Delta t}{\Delta x} \leq \frac{1.2}{\pi} \approx 0.38. \quad (2.49)$$

To investigate the viscous stability condition, we begin with the equation

$$\frac{\partial u}{\partial t} = \nu \frac{\partial^2 u}{\partial x^2}, \quad (2.50)$$

and substitute in  $u = \hat{u}e^{i\kappa x}$  as before. This gives

$$\frac{d\hat{u}}{dt} = \lambda \hat{u} \quad (2.51)$$

with  $\lambda = -\kappa^2\nu$ . The stability boundary crosses the real axis at -2.4, so  $\kappa^2\nu\Delta t \leq 2.4$ . As before, we take the worst case value of  $\kappa = \frac{\pi}{\Delta x}$ . The viscous stability condition [38] is that

$$\gamma_{visc.} = \frac{\nu\Delta t}{\Delta x^2} \leq \frac{2.4}{\pi^2} \approx 0.24. \quad (2.52)$$

At high Reynolds numbers, we expect (2.49) to be the critical constraint. This is because  $\nu$  is small. The constraint (2.52) becomes critical only if  $\Delta x$  is of the same order of magnitude as  $\nu$ , which is not the case here. By experimenting with different values of  $\gamma_{adv.}$  it was found that stable simulations could be run with values as high as 0.3. This gave a good balance between stability of the numerical method and length of timestep. In my simulations  $c$  is chosen to be 10, to be always larger than the maximum velocity, and  $\nu = V_{av}L/Re$ .

### 2.3.2 Euler Method

The scheme given in section 2.3.1 is a multistep method, so it requires that a different method be applied at the first time step. In my simulations, the first timestep is calculated using the Euler method.

The Euler method is

$$y^{(1)} = y^{(0)} + \Delta t f(y^{(0)}, 0) \quad (2.53)$$

where  $\Delta t = t^{(1)} - t^{(0)}$ . The application of this method is similar to that of the predictor step of the Adam–Bashforth–Moulton method, and as such will not be given here.

## 2.4 Boundary Conditions

The boundary conditions discussed in section 1.2.4 must be applied on the boundaries of the discretised domain. The crossflow inlet boundary conditions are simply evaluated on the discrete grid at  $x = -5$ , however the application of other conditions is more complicated, and is discussed below.

### 2.4.1 Outlet

The advective outlet boundary condition is implemented by applying the ABM3 predictor-corrector (Euler’s method for the first timestep) to (1.8), which has the same form in wavenumber space. The spatial derivative in the streamwise direction is calculated using a backwards difference method, as using a central-difference method would require points outside of the simulation region. For Euler integration, a variable  $\hat{\phi}$  at the outlet is updated by

$$\hat{\phi}^{(n+1)}(x_{\text{end}}, y, \kappa) = \hat{\phi}^{(n)}(x_{\text{end}}, y, \kappa) - \frac{\beta \Delta t}{\Delta x} (\hat{\phi}^{(n)}(x_{\text{end}}, y, \kappa) - \hat{\phi}^{(n)}(x_{\text{end}} - \Delta x, y, \kappa)) \quad (2.54)$$

where  $x_{\text{end}}$  denotes the outlet boundary position, and  $\beta$  is the free stream velocity of the crossflow,  $U_{\text{max}}$ .

When  $\hat{\phi} = \hat{u}$  the values at the outlet are scaled after the integration step to ensure that the mass fluxes entering and exiting the simulation region are equal. This involves multiplying the unscaled streamwise outlet velocity,  $\hat{u}_{\text{out}}^*$  by a scaling coefficient  $\alpha$ , such that the final streamwise velocity at the outlet,  $\hat{u}_{\text{out}}$ , is given by

$$\hat{u}_{\text{out}} = \alpha \hat{u}_{\text{out}}^*. \quad (2.55)$$

The scaling coefficient is given by

$$\alpha = \frac{Q_{\text{in}}}{Q_{\text{out}}^*} = \frac{\int \hat{u}_{\text{in},0} dy + \int \hat{v}_{\text{jet},0} dx}{\int \hat{u}_{\text{out},0}^* dy} \approx \frac{\Delta y \sum_y \hat{u}_{\text{in},0} + \Delta x \sum_x \hat{v}_{\text{jet},0}}{\Delta y \sum_y \hat{u}_{\text{out},0}^*}, \quad (2.56)$$

where  $Q_{\text{in}}$  is the flux into the domain through both the crossflow and jet inlets,  $Q_{\text{out}}^*$  is the unscaled flux through the outlet, and  $\hat{u}_{\text{in}}$  and  $\hat{v}_{\text{jet}}$  are the streamwise velocity at the inlet and the transverse velocity within the jet inlet respectively. In the integrals the velocity at the outlet prior to performing the scaling, here denoted as  $\hat{u}^*$ , with subscript 0 indicates the Fourier coefficients relating to the zero wavenumber, or the mean flow.

### 2.4.2 No-slip walls

The walls at  $y = 0$  and  $y = 10$  have the condition that  $u = v = w = 0$ . In the staggered grid system  $v$  is located on the upper and lower edges of each cell, so this value can be easily set by overwriting the boundary values with zeros. However, neither  $u$  or  $w$  are calculated directly on the boundary, so we use interpolation to define the value of a ghost point outside of the simulation region. A ghost point is a point outside of the simulation region whose value is required for intermediate calculations during the simulation but is not stored after these calculations are performed. For  $y = 0$  we have

$$\hat{u}(x, 0, \kappa) = \frac{\hat{u}(x, -\frac{\Delta y}{2}, \kappa) + \hat{u}(x, \frac{\Delta y}{2}, \kappa)}{2} = 0, \quad (2.57)$$

which rearranges to  $\hat{u}(x, -\frac{\Delta y}{2}, \kappa) = -\hat{u}(x, \frac{\Delta y}{2}, \kappa)$ . These values of  $\hat{u}$  outside of the simulation region can be used to find the values of various derivatives in the transverse direction. A similar method is used to calculate values of  $\hat{u}$  outside of the other transverse wall, at  $y = 10$ , and  $\hat{w}$  outside of both of these walls.

## 2.5 Pressure Correction

In the solution of the Navier Stokes equations as described in section 2.3, it is necessary to solve

$$\frac{\delta^2 \hat{P}}{\delta x^2} + \frac{\delta^2 \hat{P}}{\delta y^2} - \kappa^2 \hat{P} = \frac{1}{\Delta t} \left( \frac{\delta \hat{\Phi}_1}{\delta x} + \frac{\delta \hat{\Phi}_2}{\delta y} + \nu \kappa \hat{\Phi}_3 \right), \quad (2.58)$$

or

$$(A - \kappa^2 I) \hat{\mathbf{P}} = \hat{\mathbf{f}}(x, y, \kappa) \quad (2.59)$$

The system of equations (2.59) is a system of uncoupled linear systems for each wavenumber  $\kappa$ . In these equations,  $\kappa$  are the wavenumbers,  $\hat{\mathbf{P}}$  is a vector of elements of the array of pressure values at each  $\kappa$ , with element  $\hat{P}(i, j)$  of the pressure array located in  $\hat{\mathbf{P}}(N_x(j-1) + i)$  where  $N_x$  is the number of grid points in the  $x$  direction,  $\mathbf{f}$  is a vector of elements from the right hand side of equation (2.58), with elements ordered in the same way as for  $\hat{\mathbf{P}}$ , and  $A$  is an  $N_x N_y \times N_x N_y$  matrix.

In the  $\kappa = 0$  case, we set the pressure in the lower left-hand corner of the pressure array, equivalent to  $\hat{\mathbf{P}}(1)$ , to zero, which fixes the mean pressure. As the solution requires only the derivatives of  $\hat{P}$ , and not  $\hat{P}$  itself, it does not matter what value we choose for the mean pressure, so zero was chosen for simplicity.

On the boundaries, the matrix entries are modified to enforce the boundary conditions on the wall-normal component of velocity. On the upstream streamwise boundary equation (2.36) becomes

$$\hat{u}^{(n+1)}(0, y + \frac{\Delta y}{2}, \kappa) = \hat{\Phi}_1(0, y + \frac{\Delta y}{2}, \kappa) - \Delta t \frac{\hat{P}(\frac{\Delta x}{2}, y + \frac{\Delta y}{2}, \kappa) - \hat{P}(-\frac{\Delta x}{2}, y + \frac{\Delta y}{2}, \kappa)}{\Delta x}, \quad (2.60)$$

where the negative coordinate indicates a value outside of the simulation region, called a ghost point. For a boundary cell, the discrete second-derivative of pressure in the  $x$  direction is

$$\frac{\delta^2 \hat{P}}{\delta x^2}(\frac{\Delta x}{2}, y + \frac{\Delta y}{2}, \kappa) = \frac{\hat{P}(\frac{3\Delta x}{2}, y + \frac{\Delta y}{2}, \kappa) - 2\hat{P}(\frac{\Delta x}{2}, y + \frac{\Delta y}{2}, \kappa) + \hat{P}(-\frac{\Delta x}{2}, y + \frac{\Delta y}{2}, \kappa)}{\Delta x^2}. \quad (2.61)$$

The ghost point in (2.61) is eliminated using (2.60), in which case

$$\frac{\delta^2 \hat{P}}{\delta x^2}(\frac{\Delta x}{2}, y + \frac{\Delta y}{2}, \kappa) = \frac{\hat{P}(\frac{3\Delta x}{2}, y + \frac{\Delta y}{2}, \kappa) - \hat{P}(\frac{\Delta x}{2}, y + \frac{\Delta y}{2}, \kappa)}{\Delta x^2} - \frac{\hat{\Phi}_1(0, y + \frac{\Delta y}{2}, \kappa) - \hat{u}^{(n+1)}(0, y + \frac{\Delta y}{2}, \kappa)}{\Delta x \Delta t}. \quad (2.62)$$

Further substituting this into equation (2.58) allows the cancelling of some

terms, to give

$$\begin{aligned} & \frac{\hat{P}(\frac{3\Delta x}{2}, y + \frac{\Delta y}{2}, \kappa) - \hat{P}(\frac{\Delta x}{2}, y + \frac{\Delta y}{2}, \kappa)}{\Delta x^2} + \frac{\delta \hat{P}^2}{\delta y^2} - \kappa^2 \hat{P} = \\ & \frac{1}{\Delta t} \left( \frac{\hat{\Phi}_1(\Delta x, y + \frac{\Delta y}{2}, \kappa) - \hat{u}^{(n+1)}(0, y + \frac{\Delta y}{2}, \kappa)}{\Delta x} + \frac{\delta \hat{\Phi}_2}{\delta y} + \nu \kappa \hat{\Phi}_3 \right). \end{aligned} \quad (2.63)$$

The discrete  $x$ -derivative on the right-hand side of (2.63) has the same form as it has in the original equation, (2.58), except that the unknown  $\hat{\Phi}_1(0, y + \frac{\Delta y}{2}, \kappa)$  is replaced by the known values  $\hat{u}^{(n+1)}(0, y + \frac{\Delta y}{2}, \kappa)$ . This substitution is achieved in the code by overwriting the boundary values of  $\hat{u}^{(*)}$  with the specified boundary conditions before the derivative is taken. A similar method can be used to manage the downstream streamwise boundary, and both of the transverse boundaries. On the corners of the domain, where both boundary conditions apply, the modification is applied in both directions simultaneously.

After applying these boundary conditions, we construct the matrix  $A$  as an  $N_y \times N_y$  matrix of  $N_x \times N_x$  matrices, where  $N_x$  is the number of grid points in the  $x$  direction, and  $N_y$  is the number of points in the  $y$  direction. The matrix  $A$  is block tridiagonal, with blocks

$$A_{I,J} = \begin{cases} B & I = 1 \ \& \ N_y, J = I \\ C & I \in [2, N_y - 1], J = I \\ D & J = I \pm 1 \\ O & \text{otherwise,} \end{cases}$$

where the range  $[2, N_y - 1]$  indicates the interior points in the  $y$  direction,

$$B_{i,j} = \begin{cases} \frac{1}{\Delta x^2} + \frac{1}{\Delta y^2} & i = 1 \ \& \ N_x, j = i \\ \frac{2}{\Delta x^2} + \frac{1}{\Delta y^2} & i \in [2, N_x - 1], j = i \\ \frac{1}{\Delta x^2} & j = i \pm 1 \\ 0 & \text{otherwise,} \end{cases}$$

$$C_{i,j} = \begin{cases} \frac{1}{\Delta x^2} + \frac{2}{\Delta y^2} & i = 1 \ \& \ N_x, j = i \\ 2 \left( \frac{1}{\Delta x^2} + \frac{1}{\Delta y^2} \right) & i \in [2, N_x - 1], j = i \\ \frac{1}{\Delta x^2} & j = i \pm 1 \\ 0 & \text{otherwise,} \end{cases}$$

$$D_{i,j} = \begin{cases} \frac{1}{\Delta y^2} & j = i \\ 0 & \text{otherwise,} \end{cases}$$

and  $O$  is the  $N_x \times N_x$  zero matrix.

## 2.6 Analysis

### 2.6.1 Mean Field

Time averages are used to estimate mean quantities. Simulations were first run without collecting data for a period of 35000 - 42000 timesteps, approximately long enough for the crossflow to pass through the domain three times, to allow the transient period of the flow to pass. Velocity and scalar concentration data were then collected at evenly spaced times, and running averages of speed and concentration were calculated to confirm that transience had passed, as shown in Figure 2.5. A separation between collections of 20 timesteps, for  $\Delta t \approx 1.9 \times 10^{-3}$ , was chosen.

The mean field is given by

$$\langle \phi \rangle_T = \frac{1}{t_f - t_i} \int_{t_i}^{t_f} \phi(t) dt \approx \frac{1}{N} \sum_{n=1}^N \phi^{(n)}, \quad (2.64)$$

where  $\phi$  can be a component of velocity or the scalar concentration,  $t_i$  and  $t_f$  are the initial and final times of the period over which  $\phi$  is integrated, which was 16000 timesteps or a non-dimensional time of approximately 30.4,  $N$  is the total number of data sets used, which was 801, and  $\phi^{(n)}$  is the value of  $\phi$  at the  $n$ -th sample time.

The temporal mean was chosen for the analysis of flow statistics as the jet in crossflow is an inherently three-dimensional flow, so any spatial averaging could lead to a loss of spatial information. It is also known that the counter-rotating vortex pair is most easily visualised in the time-averaged flow [5].

### 2.6.2 Trajectories

The trajectory of the jet as it is deflected by the crossflow is of interest. Different methods of calculating this trajectory have been suggested, and each of these methods produces a slightly different trajectory that can provide information on different characteristics of the flow. Trajectories are calculated from the mean-field data using the methods described below.

#### Centreline Trajectory

The centreline trajectory of the jet is defined as the streamline that begins at the centre of the jet inlet. It has been used by Kelso et al. [22], Muppidi and Mahesh [40] and Yuan and Street [59].

The streamline is calculated using MATLAB's inbuilt `stream3d` function. This function requires that all three components of velocity are calculated

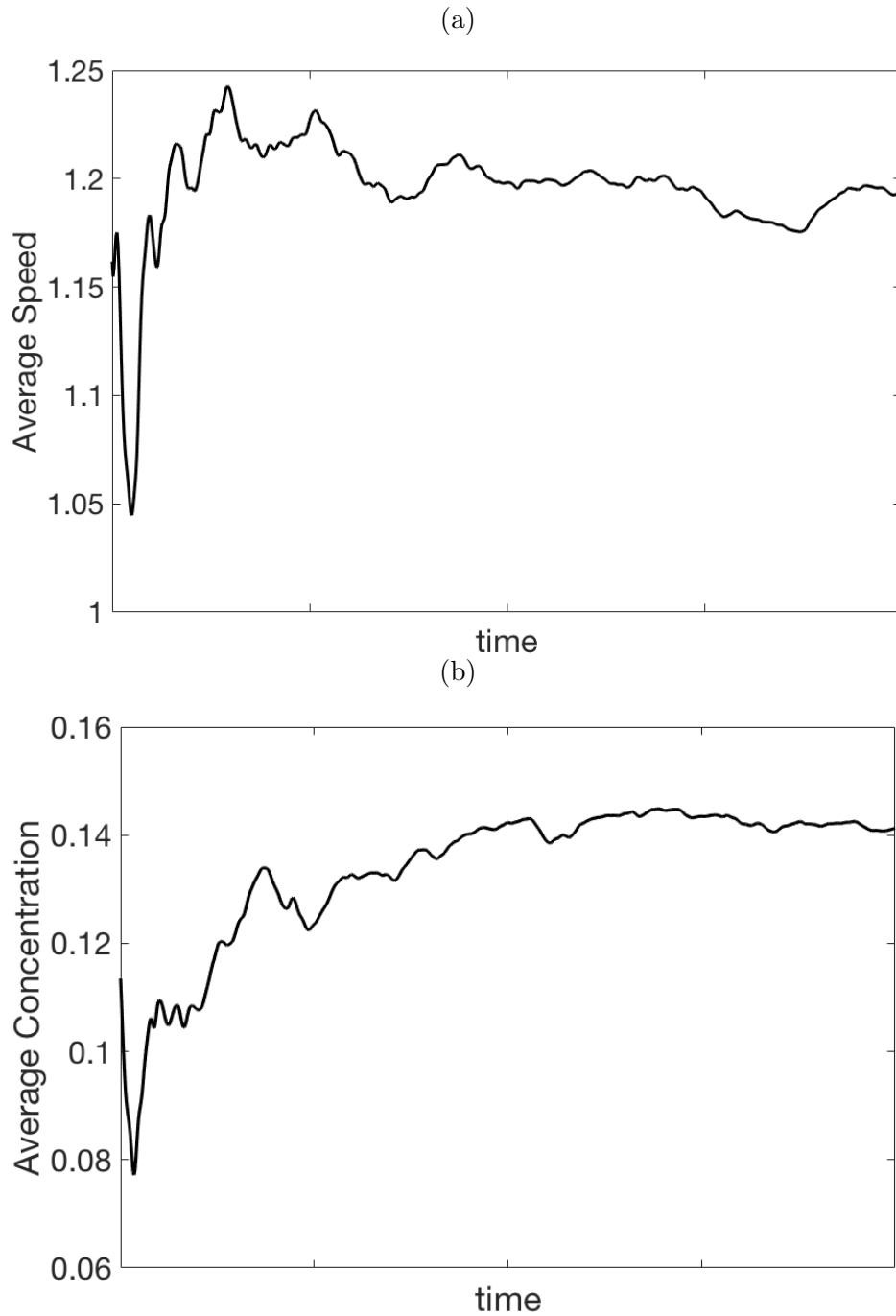


Figure 2.5: Running Averages of (a) speed and (b) concentration at  $(x, y, z) = (7.7, 5.9, 0)$  for  $\text{Re} = 2 \times 10^4$  and  $V_{av}/U_{max} = 2.25$ .



at the same position, so it is necessary to interpolate both the streamwise and transverse components of the mean velocity field to cell centres before using them as inputs in this function. The `stream3d` function produces a three dimensional trajectory, however only the  $x$  and  $y$  components of the trajectory are reported in the results, as there is little variation from  $z = 0$ .

### Concentration Trajectory

The concentration trajectory is defined as the locus of maximum scalar concentration. This method is used by Smith and Mungal [49], and the resulting trajectory is generally quite similar to the centreline trajectory.

This trajectory is calculated by finding the position of maximum concentration in the  $yz$ -plane for each value of  $x$  downstream of the centre of the jet inlet. Again, only the  $x$  and  $y$  components of the trajectory are reported in the results, as there is little variation from  $z = 0$ .

### Counter-rotating Vortex Pair Trajectory

The counter-rotating vortex pair (CVP) trajectory shows the location of the centreline of the counter-rotating vortex pair, and is measured either by the locus of maximal transverse velocity or the maximal swirling strength of the flow. Unlike the other two trajectory types, this trajectory does not begin at the centre of the jet inlet. Instead, it begins slightly downstream, at the point in the streamwise direction where the swirling strength is largest [62]. The counter-rotating vortex pair trajectory is used by Cambonie et al. [6], who note that it generally appears lower than, and parallel to, the centreline trajectory.

In this thesis, this trajectory is calculated by finding the position of maximum transverse velocity in the  $yz$ -plane for each value of  $x$  downstream of the centre of the jet inlet. As the transverse velocity values are stored on the upper and lower edges of the staggered grid, while the other two trajectory types are evaluated at cell centres, there may be a small inconsistency between the CVP trajectory and the other two trajectories, but the grid is fine enough to discount this.

### 2.6.3 Jet Spreading

Jet spreading measures the extent to which the jet entrains fluid from the crossflow. A small value of scalar concentration, in this case  $c = 0.05$ , is used to plot a contour in each  $yz$ -plane, and the maximum height and width of

the contour is recorded. The wider the jet, the more it has mixed with the surrounding crossflow.

## 2.6.4 Spectra

Spectra are calculated to show the distribution and magnitude of energy in a flow. The stretched vortex model makes the assumption that energy is proportional to  $\kappa^{-\frac{5}{3}}$  in the inertial subrange, assuming that  $\text{Re}$  is large enough. Spectra of turbulent kinetic energy and scalar concentration are calculated in the cross-stream direction, as this direction is periodic and Fourier coefficients are already available because of our numerical method. At each timestep, the fluctuation from the temporal mean is calculated,

$$\phi' = \Phi - \langle \Phi \rangle_T, \quad (2.65)$$

where  $\Phi$  is the scalar concentration,  $c$ , or the kinetic energy,  $\frac{1}{2}(u^2 + v^2 + w^2)$ ,  $\langle \Phi \rangle_T$ , is the temporal mean and  $\phi'$  is the fluctuation in the same.

As the Fourier transform is taken in the cross-stream direction, coefficients are dependent on  $x$ ,  $y$  and  $t$ . Spectral density, the amount of energy present in the system at each wavenumber  $\kappa$ , given by  $\hat{R}_\phi$ , is calculated on the jet centreline trajectory, 7.7 diameters downstream of the jet inlet at each sample time. This position was chosen to be far enough away from the inlet for turbulent flow to be developed, while also far enough away from the outlet to be unaffected by the outlet boundary conditions. The set of resulting spectra is then temporally averaged using the method given in section 2.6.1, and  $\langle \hat{R}_\phi(\kappa) \rangle_T$  is plotted for positive wavenumbers on a loglog plot for visualisation.

We expect that the majority of the energy will be located in the low wavenumbers, and that the energy will drop off as the wavenumbers increase. In an LES simulation using the stretched vortex sub-grid model, at sufficiently high Reynolds number we would expect the slope of the spectra to be approximately  $-5/3$  at the higher end of the wavenumber range.

## 2.6.5 Dissipation

The total dissipation of energy due to turbulence,  $\varepsilon$ , is split into two components,

$$\varepsilon = \varepsilon^{LS} + \varepsilon^{SGS} \quad (2.66)$$

where  $\varepsilon^{LS}$  is the resolved-scale dissipation and  $\varepsilon^{SGS}$  is the sub-grid scale dissipation. The resolved-scale dissipation rate is given by [35]

$$\varepsilon^{LS} = 2\nu \bar{S}_{ij} \bar{S}_{ij}, \quad (2.67)$$

where

$$\bar{S}_{ij} = \frac{1}{2} \left( \frac{\partial \bar{u}_i}{\partial x_j} + \frac{\partial \bar{u}_j}{\partial x_i} \right), \quad (2.68)$$

in Einstein notation. The sub-grid dissipation is approximated by the rate at which kinetic energy is transferred from resolved to sub-grid scales [35],

$$\varepsilon^{SGS} = -\tau_{ij}^{SGS} \bar{S}_{ij}. \quad (2.69)$$

Dissipation is calculated at each point within the simulation domain individually, using time-averaged quantities. The ratio of the sub-grid scale dissipation to the large scale dissipation,  $\varepsilon^{SGS}/\varepsilon^{LS}$ , can give an indication of how resolved the flow simulation is at a point within the flow. If the ratio is greater than one, the sub-grid scale dissipation dominates, indicating that the turbulence model is active. If the ratio is less than one, the majority of the dissipation happens in the large scales, and the flow is well resolved on the computational grid being used. This generally happens at low Reynolds numbers, where the flow is not necessarily turbulent. At high Reynolds number, a ratio of less than one would indicate that the turbulence model was not working properly.

The total dissipation at each point is used to calculate the Kolmogorov length scale for that point [26],

$$\eta = \left( \frac{\nu^3}{\varepsilon} \right)^{\frac{1}{4}}. \quad (2.70)$$

This scale is indicative of the size of the smallest eddies [26]. By comparing this to the grid size  $\Delta x$ , we can determine whether or not all of the eddies are being resolved.

Both the dissipation ratio,  $\varepsilon^{SGS}/\varepsilon^{LS}$ , and the Kolmogorov ratio,  $\eta/\Delta x$ , are plotted as filled contours on the centreplane,  $z = 0$ , within the jet plume, chosen as the region where the scalar concentration,  $c \geq 0.05$ . This allows the effect of the sub-grid stress model to be visualised in a region that is expected to be turbulent.

### 2.6.6 Turbulent Kinetic Energy

In an LES simulation, it is desirable for a minimum of 80% of the turbulent kinetic energy (TKE) to be resolved on the computational grid [31]. By calculating both the large scale and sub-grid TKE we can confirm whether this is achieved in our simulations.

The large-scale TKE is calculated by

$$K(t) = \frac{1}{2} u'_i(t) u'_i(t), \quad (2.71)$$

where  $u'_i$  is the fluctuation in the velocity, calculated as in equation (2.65). This calculation is performed at each timestep then averaged over time to produce the final result. The sub-grid TKE is

$$K^{\text{SGS}} = \frac{1}{2}\tau_{ii}, \quad (2.72)$$

calculated from the time averaged values of  $\tau_{ii}$ .

To determine what proportion of the energy is resolved by the large scale solver, we compute the ratio of the resolved scale TKE to the total TKE,  $K_{\text{rat}} = \frac{K}{K+K^{\text{SGS}}}$ , at all cell centres within the grid. This is plotted as a contour plot on the centreplane,  $z = 0$ .

### 2.6.7 Vortex identification

Vortices are an important feature of turbulent flows and, in jets in crossflow, are responsible for much of the entrainment of crossflow fluid into the jet. Two methods were used to identify the location of vortices within the flow.

The first method is to calculate the vorticity,  $\boldsymbol{\omega} = \nabla \times \mathbf{u}$ , where  $\mathbf{u}$  is the vector of velocities, and plot contours or isosurfaces of single vorticity components to visualise the location of regions with high vorticity. This can be extended to the enstrophy,  $\boldsymbol{\omega}^2 = \omega_1^2 + \omega_2^2 + \omega_3^2$ , a scalar quantity indicative of the magnitude of vorticity, irrespective of the direction.

The second method uses Chong et al.'s [9] result that vortices are regions where the eigenvalues of the velocity gradient tensor,  $\nabla \mathbf{u}$ , are complex. This corresponds to regions where the discriminant,  $\Delta$ , of the velocity gradient tensor is positive. For an incompressible flow  $\Delta$  is given by

$$\Delta = \frac{27}{4}R^2 - Q^3, \quad (2.73)$$

where

$$R = -\frac{1}{3} \frac{\partial u_i}{\partial x_j} \frac{\partial u_j}{\partial x_k} \frac{\partial u_k}{\partial x_i} \quad (2.74)$$

and

$$Q = -\frac{1}{2} \frac{\partial u_i}{\partial x_j} \frac{\partial u_j}{\partial x_i}, \quad (2.75)$$

in Einstein notation [23]. By plotting isosurfaces of positive  $\Delta$  we can see regions where the eigenvectors of  $\nabla \mathbf{u}$  are complex, and thus where vortices are present in the flow.

## 2.7 Implementation

The majority of the functions used to produce simulations for this thesis are written in the computational language Julia. The only exception is the sub-grid stress and sub-grid flux model, provided by Trent Mattner [34], which is written in Fortran.

### 2.7.1 Fourier transform

The Fourier transform is done using the Fast Fourier Transform (FFTW) algorithm, which is implemented as a built-in set of functions in Julia. We assume that all flows which are investigated will have only real components, so we can use the real Fast Fourier Transform, `rfft`, and its inverse, `irfft`, to reduce the size of the arrays used. These functions assume that the Fourier coefficients have conjugate symmetry, so it is only necessary to store the coefficients for  $\kappa = 0, \dots, \frac{N_z}{2}$ , rather than the full range of  $\kappa = -\frac{N_z}{2} + 1, \dots, \frac{N_z}{2}$ . This change means that the arrays of coefficients are slightly more than half the size of those that would be produced by the regular `fft` function, which allows for a more efficient solver.

The function `rfft` has two inputs: an array of physical space values and a specification of the dimension, or dimensions, of that array on which the Fourier transform will act. In these simulations, the Fourier transform was used in the third dimension, corresponding to the  $z$  direction. The function `irfft` takes three inputs: an array of Fourier coefficients, the length of the physical space array in the transformed dimension, and a specification of the dimension, or dimensions, of that array on which the inverse Fourier transform will act.

### 2.7.2 Producing and factorising matrices

The matrices used to solve the pressure Poisson equation, given in section 2.5, are large and prohibitively expensive to solve in their full state. To reduce the computational expense to manageable levels, the matrices are produced and stored in sparse form. The locations and values of non-zero elements are stored in vectors, and the sparse matrix produced using `sparse(I, J, V)`, where `I` and `J` are the indices at which the value `V` appears.

To further reduce computational cost, the sparse matrices are factorised at the beginning of the simulation, and those factorised matrices are used for the duration of the simulation. This is done by using the inbuilt Julia function `lu`, which performs LU factorisation on two dimensional arrays. A large

number of these factorised arrays are necessary, one for each of the non-negative wavenumbers. For simplicity, all of these two-dimensional factorised arrays were stored in one three-dimensional array, and called individually as necessary.

### 2.7.3 Calling Fortran functions

Julia has an inbuilt function, `ccall`, which allows calls to functions written in other languages, particularly C and Fortran. The code written in the other language must be available as a shared library, and can be called with or without input variables as necessary.

The four inputs of the `ccall` function are a function-library pair, which indicate where the function is located; a tuple of the types of the output variables; a tuple of the types of the input variables; and a tuple of the input variables themselves. In the functions used in these simulations the values of the input variables are modified by the code, rather than being output as new data, so the second `ccall` input is given as `Void`.

### 2.7.4 Saving Data - HDF5

Data that is used for analysis is saved in the Hierarchical Data Format, HDF5 [51]. This format allows a large number of arrays to be stored within a single file, with no limit on the size or type of the array. Arrays from within the files can be accessed individually by a number of different programs and languages. Along with the arrays of concentration and velocity data, arrays containing metadata such as the viscosity, diffusivity, boundary conditions and timestep are saved for reference.

HDF5 files are created and opened using the command

```
h5open(filename, write status) do file.
```

The write status can be set to "w" to write new data and overwrite old data; "r" to only read data without modifying the file; or "r+" to append new arrays to an already created file. Arrays are written to the opened file using the command `write(filename,directory,array)`. The file is then closed using an `end`. Data can also be quickly read from an HDF5 file using the command `h5read(filename,directory)`.

## 2.8 Comparisons to Known Solutions

In order to determine the accuracy of the numerical solver, a direct numerical simulation of a two dimensional Taylor–Green vortex, combined with uniform flow in the third dimension, was performed without the turbulence model implemented. The two-dimensional Taylor–Green vortex is one of the few analytic solutions to the Navier–Stokes equations. The exact solution is [50]

$$\begin{aligned} u(x, y, z, t) &= 1, \\ v(x, y, z, t) &= \sin(y) \cos(z) e^{-2\nu t}, \\ w(x, y, z, t) &= -\cos(y) \sin(z) e^{-2\nu t}. \end{aligned} \quad (2.76)$$

The simulation was run on a  $2\pi$  cubic domain, with 100 grid cells in each direction, for 10000 timesteps, with  $\frac{U\Delta t}{\Delta x} \approx 0.3$ , where  $U$  is a number larger than the highest velocity that appears during the simulation, in this case chosen as  $U = 2$ . The viscosity,  $\nu$ , of the flow was set to zero so that the Taylor–Green vortex did not decay with time. Boundary conditions requiring no tangential stress,

$$\frac{\partial u}{\partial y} = \frac{\partial w}{\partial y} = 0, \quad (2.77)$$

along with  $v = 0$ , were used on the walls at  $y = 0$  and  $y = 2\pi$ . These boundary conditions are consistent with the exact solution. As  $u$  and  $w$  are located away from the boundaries on a staggered grid, when a central-difference method is applied the value of the wall-normal derivative will be located on the boundary. The boundary condition at  $y = 0$  is implemented by setting

$$\frac{\delta \hat{\phi}}{\delta y}(x, 0, \kappa) = \frac{\hat{\phi}(x, \frac{\Delta y}{2}, \kappa) - \hat{\phi}(x, -\frac{\Delta y}{2}, \kappa)}{\Delta y} = 0, \quad (2.78)$$

where  $\phi$  is  $u$  or  $w$ , yielding  $\hat{\phi}(x, -\frac{\Delta y}{2}, \kappa) = \hat{\phi}(x, \frac{\Delta y}{2}, \kappa)$ . The variable at the ghost point  $(x, -\frac{\Delta y}{2}, \kappa)$  is substituted as necessary to calculate other derivatives in the transverse direction. A similar method is used to produce a ghost point for the value of  $\phi$  outside the other transverse wall, at  $y = 2\pi + \Delta y$ . On  $x = 2\pi$  the advective boundary condition specified by equation (1.8) was used. This outlet condition is consistent with the solution, as streamwise derivatives of all three components of velocity are zero, and the solution does not decay with time, leading to a zero temporal derivative.

The initial conditions in three dimensions are given by (2.76) at  $t = 0$ , and are consistent with the boundary conditions at  $y = 0$ ,  $y = 2\pi$  and  $x = 2\pi$ , as well as at the two periodic boundaries at  $z = 0, 2\pi$ . Equation (2.76) with  $\nu = 0$  is also used as the boundary condition at  $x = 0$  throughout

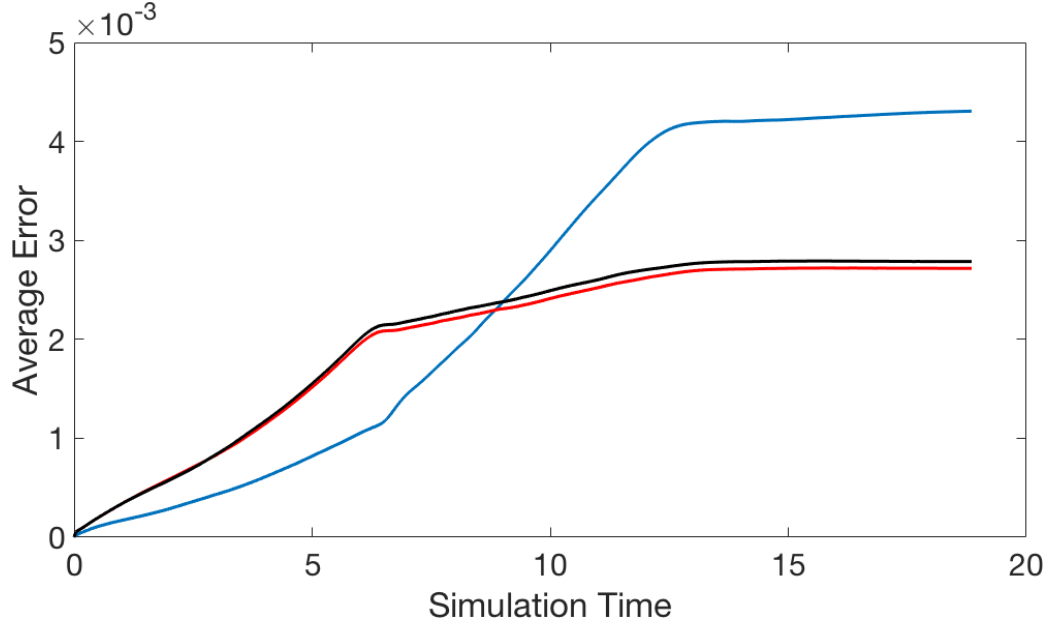


Figure 2.6: Average error in  $u$  (blue),  $v$  (red) and  $w$  (black) over time for Taylor-Green vortex with  $\nu = 0$ .

the simulation. The uniform flow in  $u$  is equivalent to the artificial boundary layer condition given in section 1.2.4 in the limit  $d \rightarrow 0$ .

As all derivatives of  $u$  are zero, the streamwise flow should have no impact on the Taylor-Green vortex in the other two directions. As the solution does not decay with time, the error is determined by comparing the results of the simulation to the exact solution.

The average error was calculated thus:

$$\text{Error}(t) = \frac{1}{N_x N_y N_z} \sum_{i=0}^{N_x} \sum_{j=0}^{N_y} \sum_{k=0}^{N_z} |\phi(x_i, y_j, z_k, t) - \phi(x_i, y_j, z_k, 0)|. \quad (2.79)$$

where  $\phi(x, y, z, t)$  is any component of velocity at timestep  $t$ . Figure 2.6 shows the evolution of the error in time. The error in  $v$  and  $w$  follow a similar path, while the error in  $u$  grows differently. Overall, the magnitude of the error is small, on the order of  $10^{-3}$ , suggesting that the solver is working correctly. It should be noted that this simulation did not test the accuracy of the calculation of the streamwise derivatives, as here they are zero everywhere.



## 2.9 General flow properties

We conclude this chapter with an example jet in crossflow simulation for a velocity ratio of  $V_{av}/U_{max} = 2.3$  and  $Re = 640$  to show the general properties of the flow, and ensure that the code is acting as expected. The simulation was run with  $\Delta t = 1.9 \times 10^{-3}$ .

Isosurfaces of individual velocity components, velocity magnitude and scalar concentration are plotted for three early simulation times, after non-dimensional times of 6.9, 34.5 and 69, and for the time averaged flow, which is calculated from 800 flow instances between non-dimensional times of 269.1 and 279.5. Early times were chosen to show the changes that occur in the transient portion of the flow.

Isosurfaces of the streamwise velocity, shown in Figure 2.7, display the spreading of the jet, both near to the jet inlet and further downstream, as time passes. In Figures 2.7a - 2.7c rings of streamwise velocity can be seen wrapped around the jet inlet and travelling downstream. These are indicative of the spanwise rollers discussed by Yuan et al. [59]. These spanwise rollers can also be seen in the isosurfaces of cross-stream vorticity and enstrophy shown in Figure 2.11. In the isosurface of time averaged velocity, Figure 2.7d, all of the turbulent fluctuations are smoothed out, and only the mean-flow feature, the central portion of the jet plume, remains. The isosurfaces of transverse velocity in Figure 2.8, and cross-stream velocity in Figure 2.9 also show structures in the transient images that are not present in the time averaged flow, which are likely indicative of vortical structures.

Isosurfaces of scalar concentration are shown in Figure 2.10, and reveal that while the higher concentration regions,  $c = 1$  and  $c = 0.5$ , do not significantly change in shape over time, the low concentration isosurface,  $c = 0.05$ , changes shape dramatically over time, giving a good indication of the shape of the jet. Figure 2.10b shows a wide plume until around  $x = 10$ , and a narrow plume thereafter. In Figure 2.10c the wide plume has travelled to the outlet of the simulation domain. The narrower region of the jet is likely the inner jet plume, travelling faster than the surrounding crossflow, while the wider region is caused by entrainment of fluid into the jet over time. The time averaged isosurfaces of the scalar concentration show the shape generally associated with the counter-rotating vortex pair.

### 2.9.1 Counter-rotating vortex pair

The counter-rotating vortex pair (CVP) is a flow characteristic of time averaged jets in crossflow that has been investigated at length through both experiments [4, 5, 6, 17, 21, 22] and simulations [46, 58, 59]. The presence of

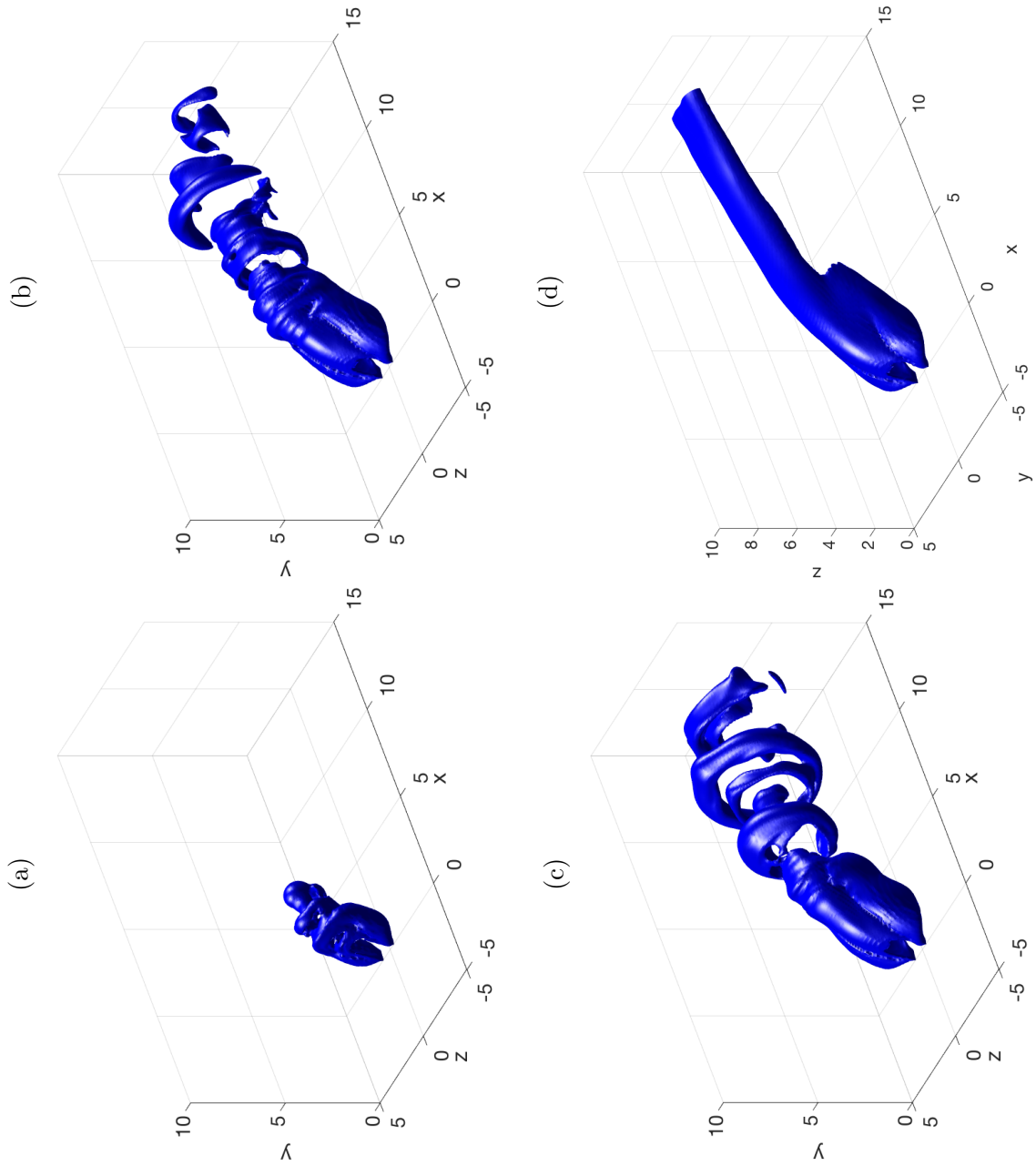


Figure 2.7: Isosurfaces of streamwise velocity,  $u = 1.2$ , for  $V_{av}/U_{max} = 2.3$  and  $Re = 640$ , at non-dimensional times of (a) 6.9, (b) 34.5, and (c) 69 and (d) the temporal average taken after the transient stage has passed.

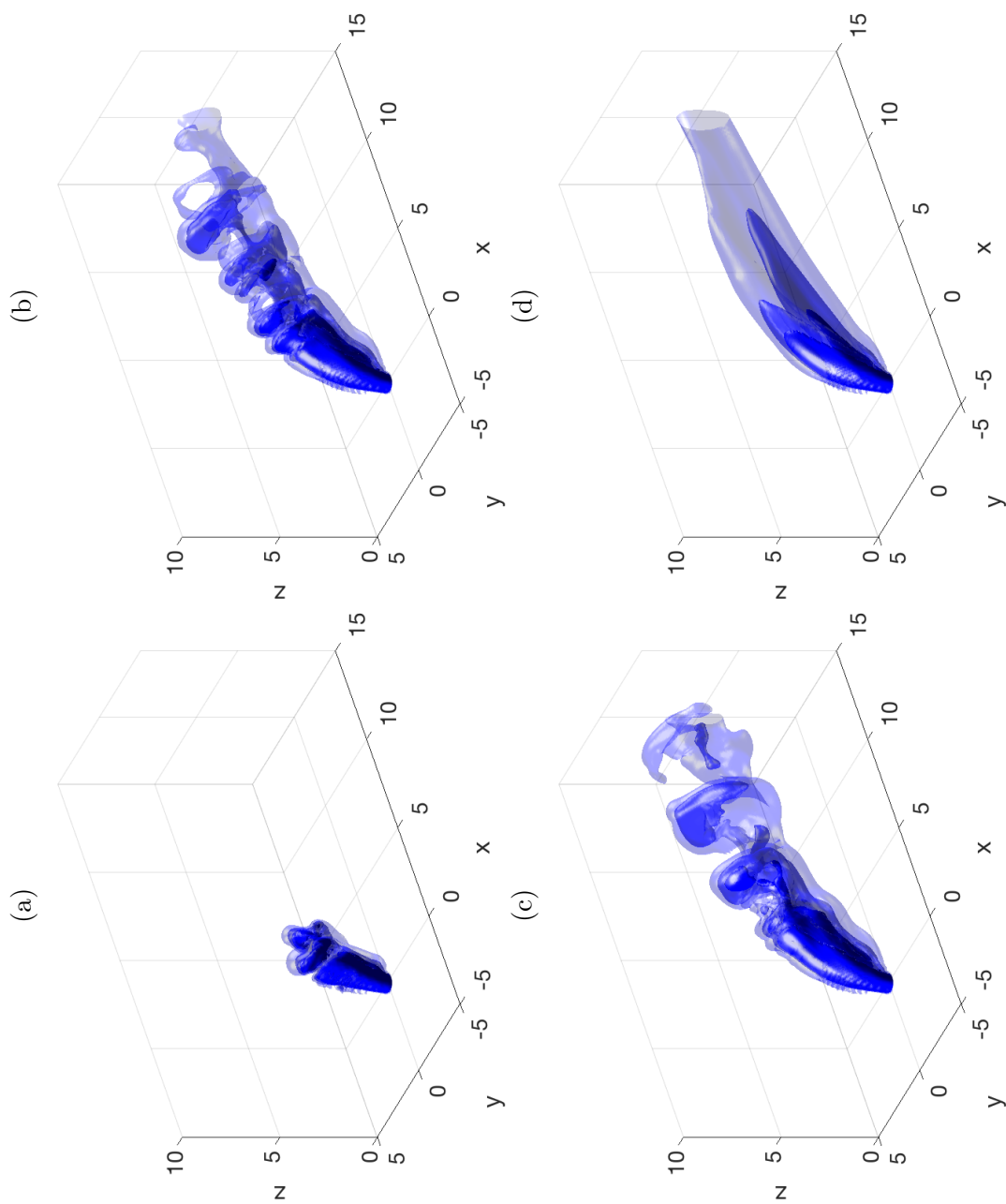


Figure 2.8: Isosurfaces of transverse velocity, with increasing opacity indicating increasing velocity, for  $V_{av}/U_{max} = 2.3$  and  $Re = 640$ , at non-dimensional times of (a) 6.9, (b) 34.5, and (c) 69 and (d) the temporal average taken after the transient stage has passed.

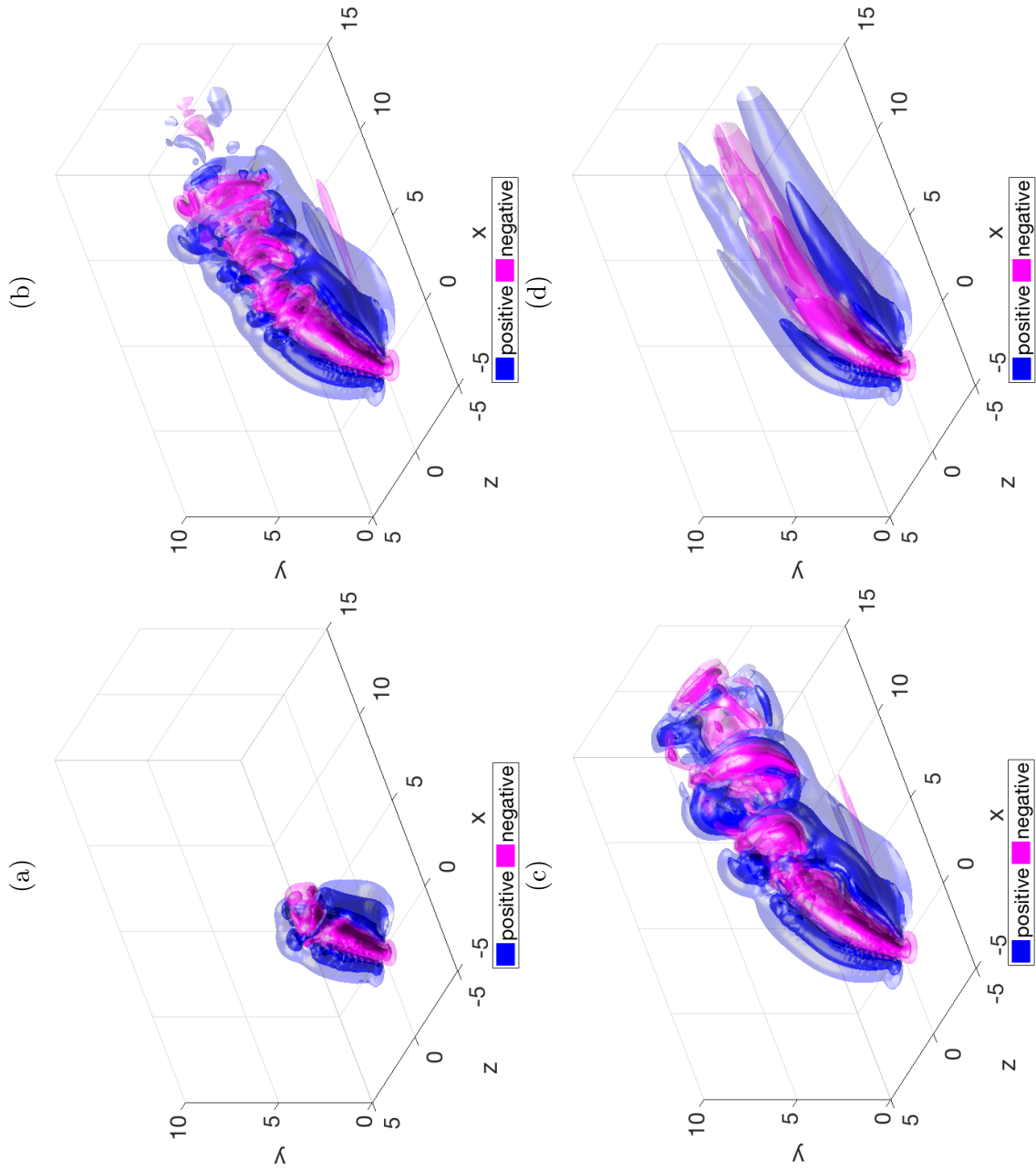


Figure 2.9: Isosurfaces of cross-stream velocity, with increasing opacity indicating increasing velocity and colours indicating direction, for  $V_{av}/U_{max} = 2.3$  and  $Re = 640$ , at non-dimensional times of (a) 6.9, (b) 34.5, and (c) 69 and (d) the temporal average taken after the transient stage has passed.

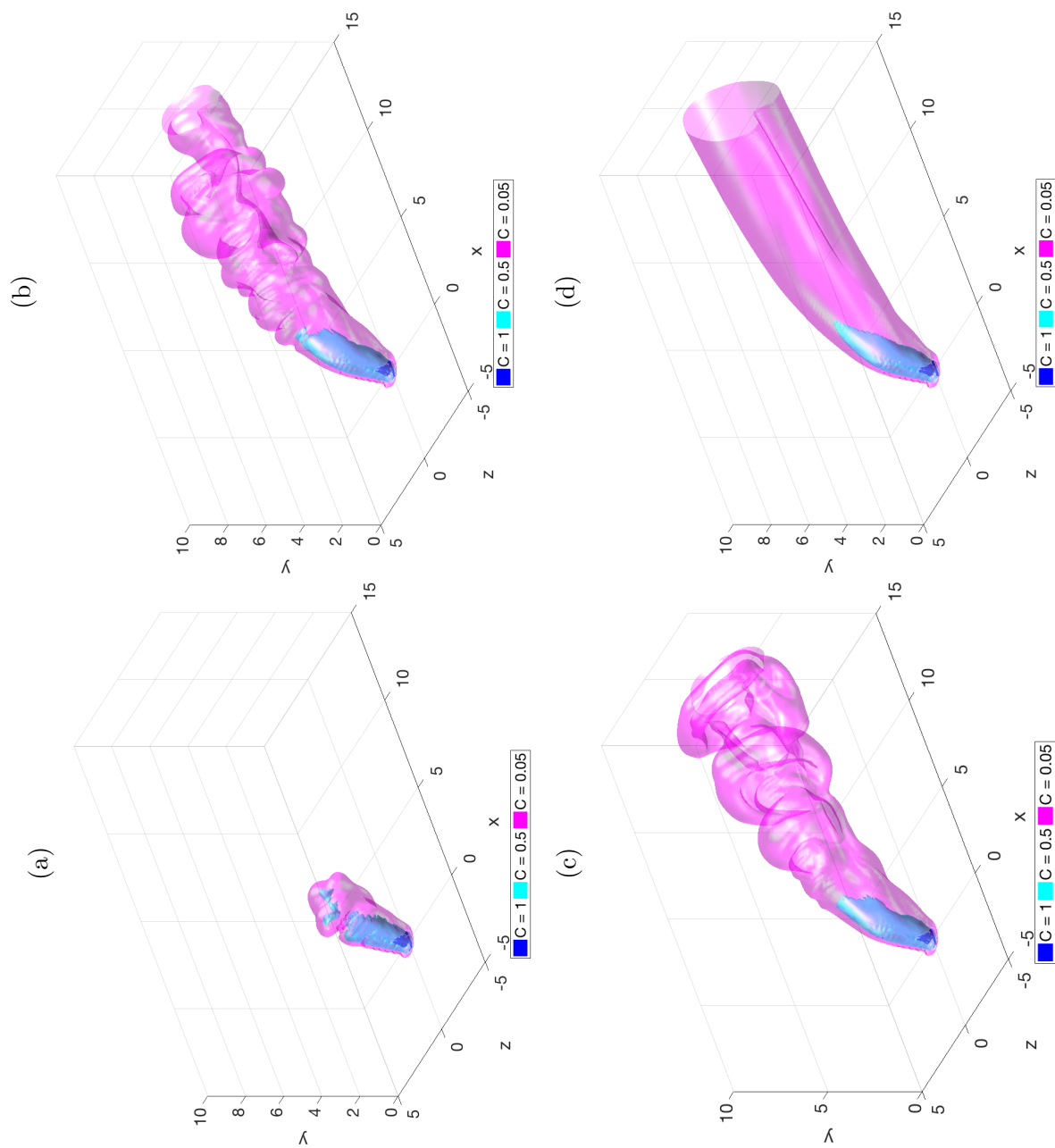


Figure 2.10: Isosurfaces of scalar concentration, for  $V_{av}/U_{max} = 2.3$  and  $Re = 640$ , at non-dimensional times of (a) 6.9, (b) 34.5, and (c) 69 and (d) the temporal average taken after the transient stage has passed.

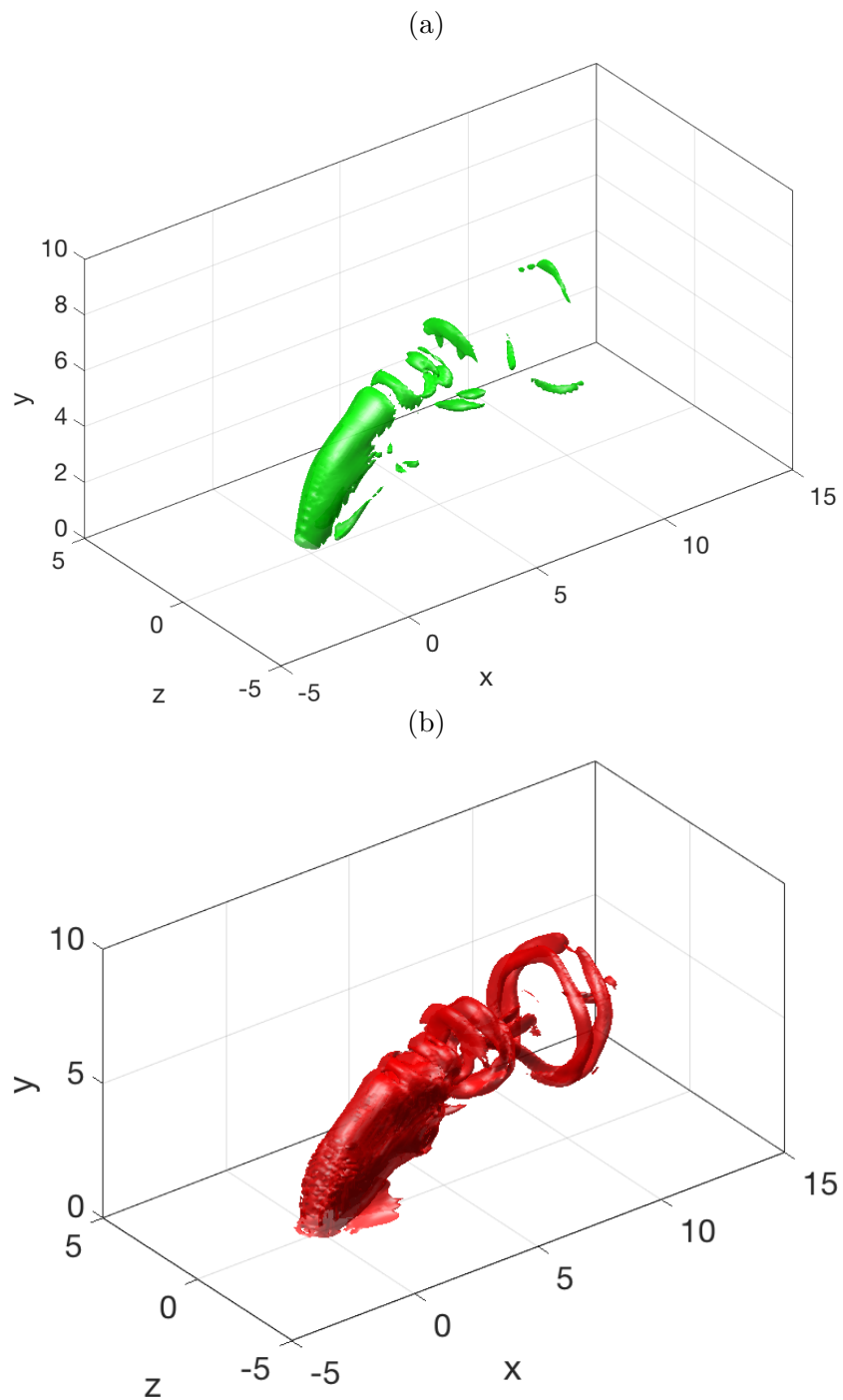


Figure 2.11: Isosurfaces of (a) cross-stream vorticity,  $\omega_z = 5$ , and (b) enstrophy,  $\omega^2 = 20$ , at 10000 timesteps, showing spanwise rollers.

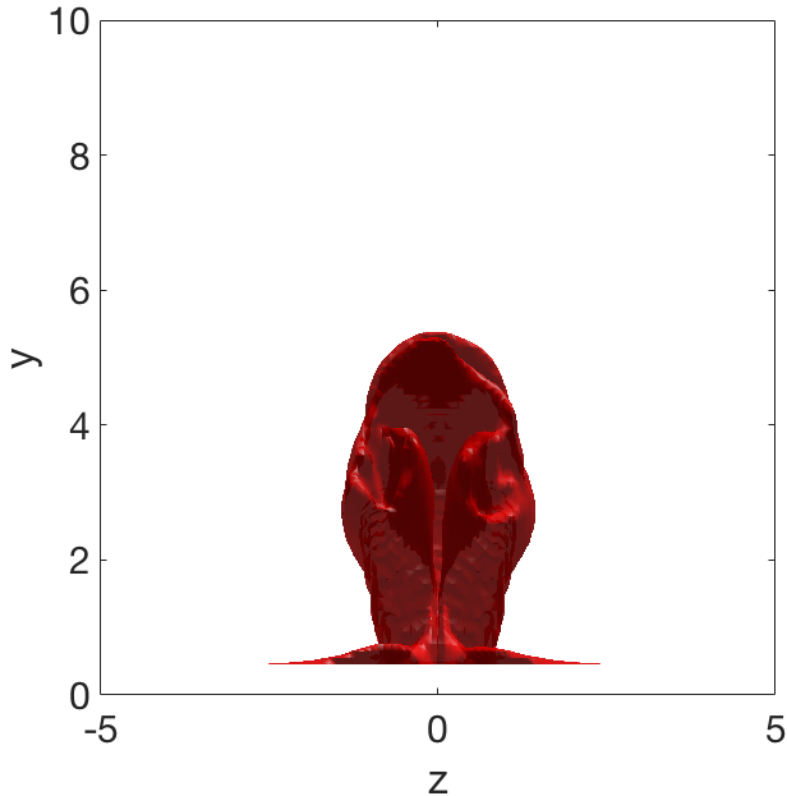


Figure 2.12: Isosurface of time-averaged enstrophy,  $\omega^2 = 5$ , showing CVP development.

the CVP in our results was investigated using vorticity, scalar surfaces and the discriminant, as described in section 2.6 above.

Isosurfaces are used to investigate the three-dimensional structure of the CVP. An isosurface of enstrophy in Figure 2.12 shows two spiralling regions fairly close to the jet inlet that may indicate the early sections of the counter-rotating vortex pair. In Figure 2.13 the isosurface of the discriminant of the velocity gradient tensor is shown for the time-averaged flow. This shows regions of the flow where vortices are present. Of particular interest here are the two central tube-shaped protrusions on the downstream side of the jet. These tube-shaped vortices are indicative of the CVP. The two tubes are not exactly the same shape or size, suggesting that the strengths of the two vortices are different, and the CVP is not exactly symmetrical.

Figure 2.14 shows contours of scalar concentration at positions downstream of the jet inlet. At  $x = 1$  the jet has already begun to take on the recognised kidney-like shape of the CVP. This shape persists for the full length of the simulation domain.

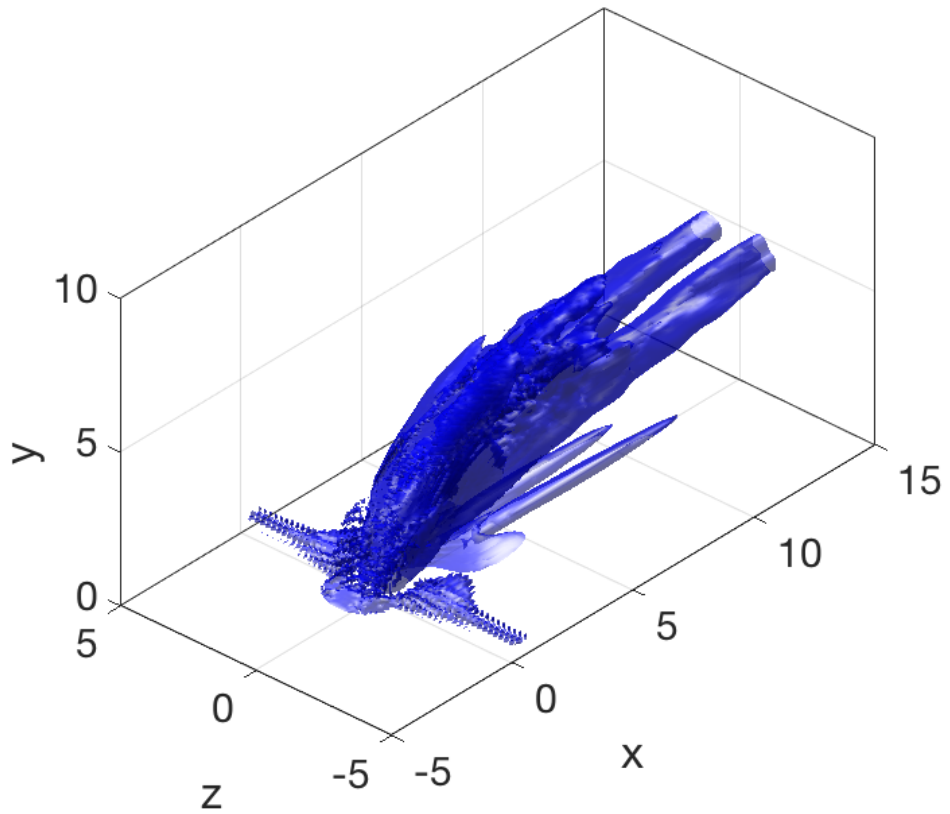


Figure 2.13: Isosurface of the time-averaged discriminant,  $\Delta = 1 \times 10^{-3}$  showing CVP.



The counter-rotating vortex pair can also be visualised in contour plots of the streamwise component of vorticity, as shown in Figure 2.15. In this series of images the development of the CVP as the jet plume travels downstream can be seen. Close to the jet inlet the regions with high vorticity magnitude (both positive and negative, indicating the direction of the vortices) are around the outer regions of the jet, surrounding a region of lower vorticity. Further downstream the two round high vorticity magnitude regions indicate where the CVP has formed.

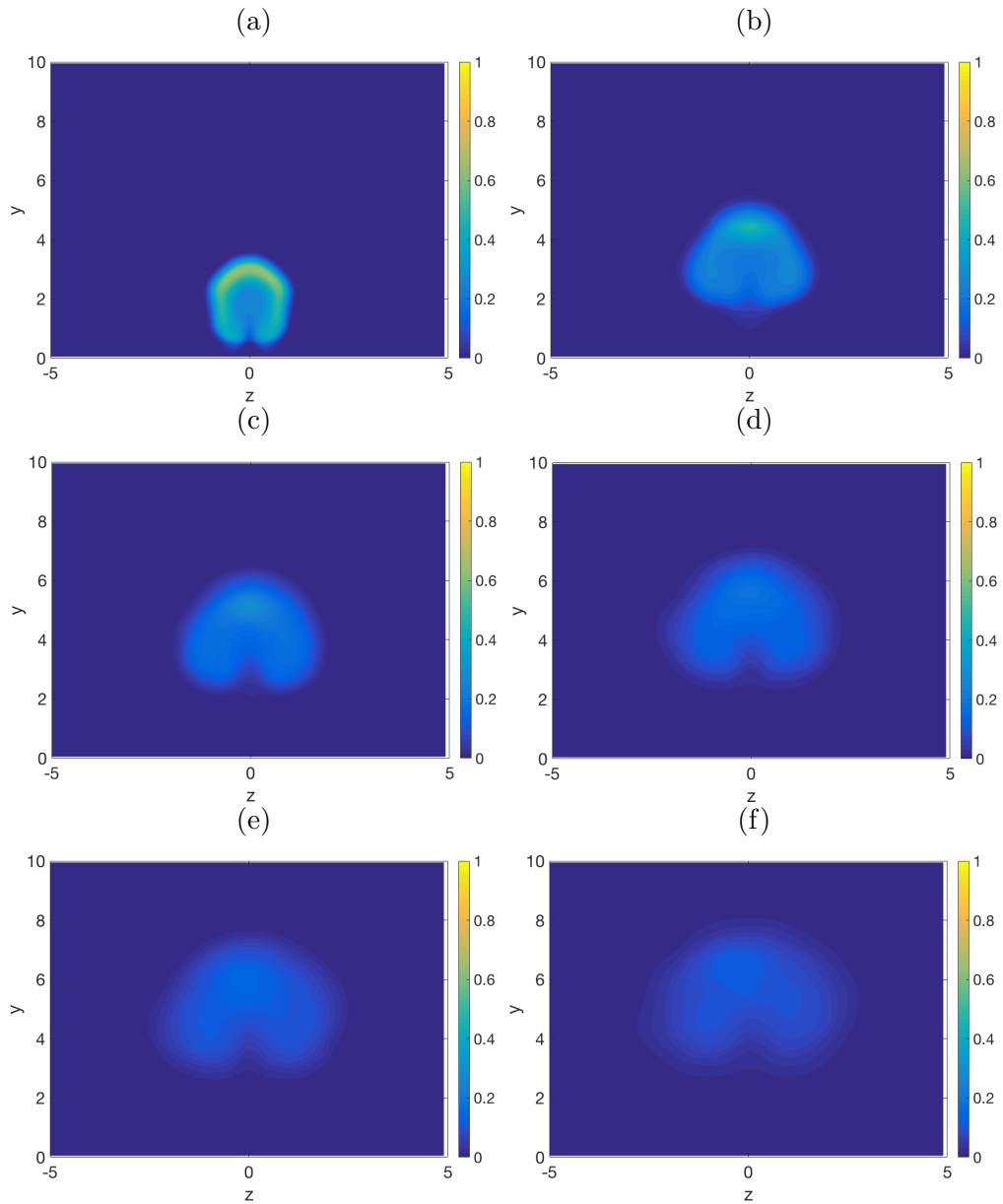


Figure 2.14: Contours of time-averaged scalar concentration in  $yz$ -plane. Slices taken at (a)  $x = 1$ , (b)  $x = 3.5$ , (c)  $x = 6$ , (d)  $x = 8.5$ , (e)  $x = 11$  and (f)  $x = 13.5$ .

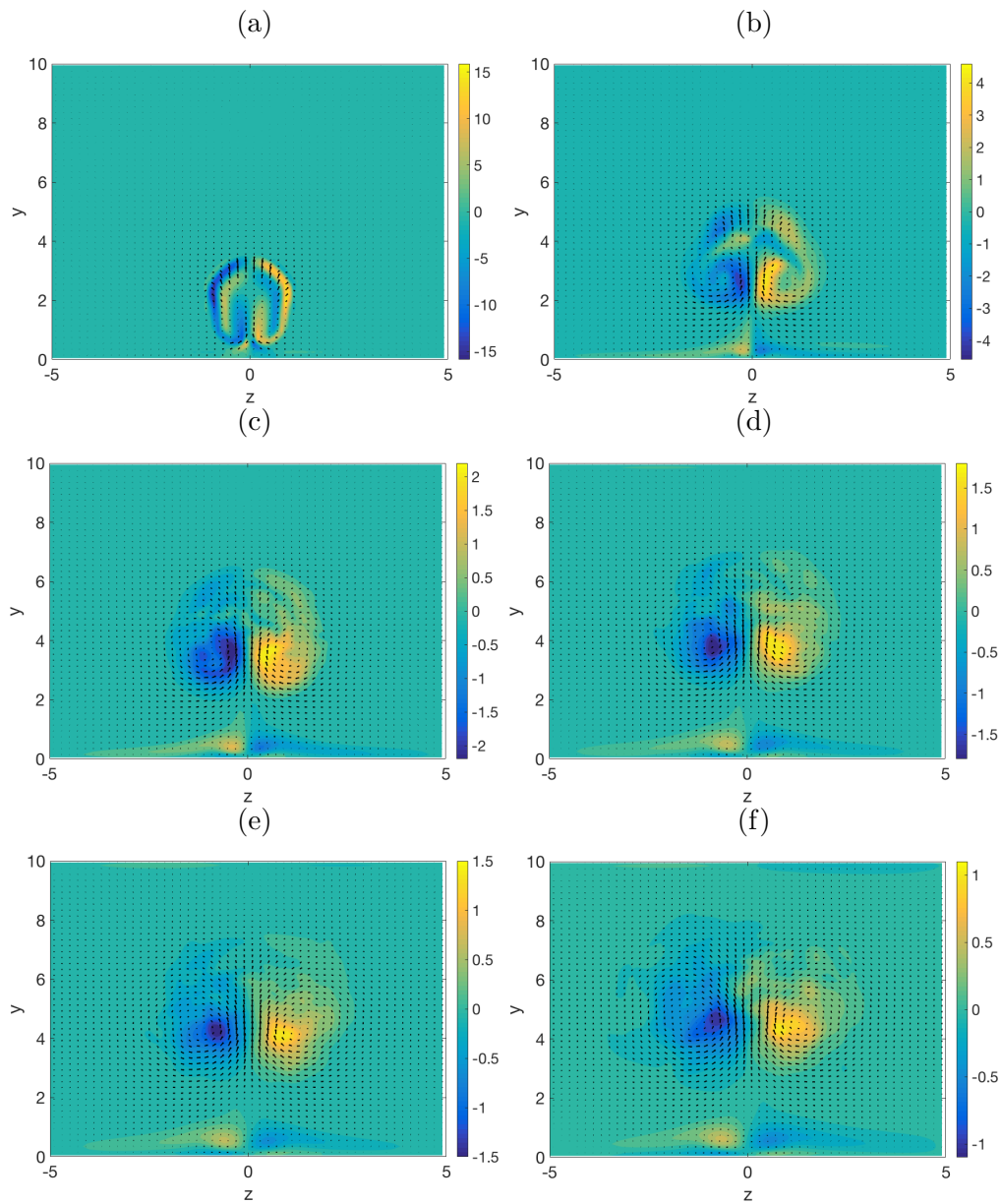


Figure 2.15: Contours of time-averaged vorticity in  $yz$ -plane overlaid with quiver plot of velocity. Slices taken at (a)  $x = 1$ , (b)  $x = 3.5$ , (c)  $x = 6$ , (d)  $x = 8.5$ , (e)  $x = 11$  and (f)  $x = 13.5$ .

## 2.10 Conclusion

In this chapter a hybrid second-order finite-difference and spectral finite-difference method for solving the Navier–Stokes equations is described, to be applied to the large-eddy simulation of a jet in crossflow. Methods for analysing the results of these simulations are also presented.

The Navier–Stokes solver is used, with the sub-grid scale model switched off, to perform a simulation of a zero-viscosity Taylor–Green vortex, a flow with a known exact solution. The results of this simulation show that the Navier–Stokes solver is working as expected.

Finally, the Navier–Stokes solver, with the sub-grid scale model switched on, was used to simulate a low Reynolds number jet in crossflow. Isosurfaces of velocity, scalar concentration, vorticity, enstrophy and the discriminant were used to show various well-documented flow characteristics, such as spanwise rollers and the counter-rotating vortex pair. The counter-rotating vortex pair was also shown through contour plot of time averaged scalar concentration and vorticity.

In the following chapters further simulations of jets in crossflow will be analysed. First, simulations will be compared to experiments and other published and unpublished simulations, to ensure that the Navier–Stokes solver and sub-grid scale model produce reasonable results. A series of simulations with all parameters but the velocity ratio held constant will then be analysed to determine the effect of velocity ratio on the behaviour of the jet. Finally, large-eddy simulations of a jet in crossflow will be compared to their direct numerical simulation counterparts, at low and moderate Reynolds numbers, to investigate the effects of the sub-grid model on the large-scale flow.

# Chapter 3

## Comparison to experiments and other simulations

Seven simulations (see Table 3.1) were run for comparison of our large-eddy simulation (LES) method with experiments and other simulations. Experimental results from Cambonie et al. [6] were used to validate the data produced by our simulations. LES performed by others [40, 56, 59] were used to validate our numerical methods. A full comparison of flow characteristics was carried out using results produced from my code and from a code written by Trent Mattner.

| Re                 | $V_{av}/U_{max}$ | $d$  | Notes  |
|--------------------|------------------|------|--|
| 243                | 0.54             | 1.83 | Cambonie et al., 2013 [6]                      |
| 640                | 3.05             | 2.06 | Cambonie et al., 2013 [6]                      |
| 1500               | 1.52             | 0.44 | Muppidi and Mahesh, 2005 [40]                  |
| 6930               | 3.3              | 0.5  | Yuan et al., 1999 [59]                         |
| $2.05 \times 10^4$ | 0.5              | 1    | Wegner et al., 2004 [56]                       |
| $2 \times 10^4$    | 2.25             | 1    | Thomas' simulation, for full code validation   |
| $2 \times 10^4$    | 2.25             | 1    | Mattner's simulation, for full code validation |

Table 3.1: Table of parameters for simulations discussed in this chapter, showing Reynolds number, Re, velocity ratio,  $V_{av}/U_{max}$ , and crossflow boundary layer thickness,  $d$ .

The Reynolds number, Re, the velocity ratio,  $V_{av}/U_{max}$ , and the boundary layer thickness at the inlet,  $d$ , were chosen to correspond to the cases considered in the given publications. The apparent difference in the Reynolds numbers given in Table 3.1 and those given by the original authors in some cases is due to different definitions of the Reynolds number. Further, all simu-

lations other than Wegner use boundary layer thicknesses that were specified in the original papers. No boundary layer thickness was specified in Wegner et al.'s paper [56], so a value of  $d = 1$  was chosen.

### 3.1 Comparison with published experimental results

Cambonie et al. [6] performed a series of experiments in which a range of jets in crossflow, with different jet velocities, Reynolds numbers, and boundary layer thicknesses, were produced in a water tunnel, and velocity data was collected using 3D particle tracking velocimetry. Figure 3.1a shows a comparison of counter-rotating vortex pair trajectories between my simulation, run for  $Re = 243$ ,  $V_{av}/U_{max} = 0.54$  and  $d = 1.83$  and experiment 1 from Cambonie et al. Figure 3.1b shows a comparison of counter-rotating vortex pair trajectories between a second simulation, run at  $Re = 640$ ,  $V_{av}/U_{max} = 3.05$  and  $d = 2.06$  and experiment 16 from Cambonie et al.

Cambonie et al. locate two transverse velocity maxima at each  $x$  position downstream of the jet [6]. The maximum with the lower position in the  $y$  direction is used to track the CVP trajectory, and the maximum with the higher  $y$  position is used to track the jet trajectory. In my analysis, only a global maximum is recorded. Close to the jet inlet, this single maximum captures the jet trajectory, as the initial velocity of the jet has a larger transverse component than the CVP close to the inlet. Further away from the inlet, the transverse velocity induced by the CVP is larger than that of the jet itself, which causes the drop off that can be seen around  $x = 2$  in my results in both Figures 3.1a and 3.1b. We compare the trajectories of my simulation to the experiments only after this drop.

Better agreement between CVP trajectories is seen for the simulation with the higher velocity ratio and Reynolds number, in Figure 3.1b, than for the low Reynolds number and low velocity ratio simulation in Figure 3.1a, especially downstream of the jet inlet. The agreement between the CVP trajectories for the lower velocity ratio and Reynolds number is not as good, as shown in Figure 3.1a. Cambonie et al. do not specify their definition of the boundary layer thickness, so it is likely that it is different to the definition that is used for these simulations. If this is the case, the boundary used in my simulation would be thinner than that seen in Cambonie et al.'s experiments, as my value of  $d$  indicates the 99.99% thickness, rather than the 80% or 99% thickness, as is common. This would contribute to the differences seen between the results of my simulations and those of Cambonie et al.'s

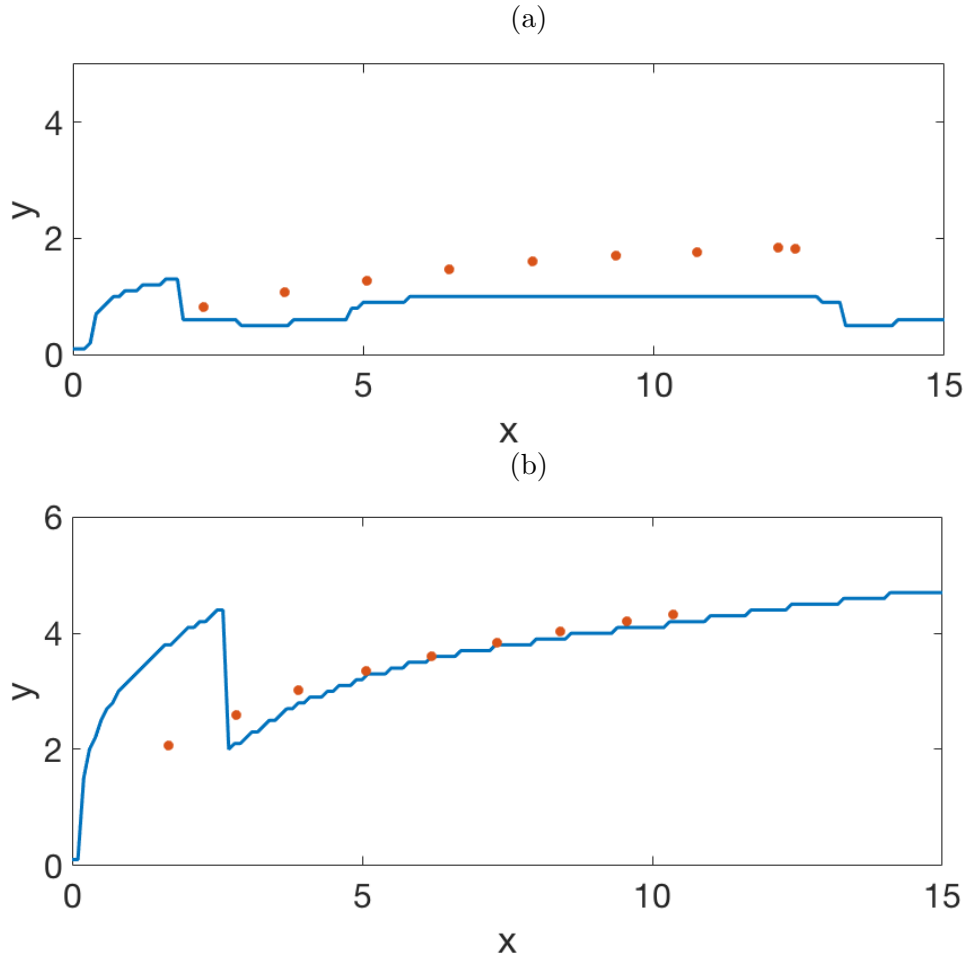


Figure 3.1: Counter-rotating vortex pair trajectories of my simulation (line) and Cambonie et al.'s configuration 1 (circles) for (a)  $Re = 243$ ,  $V_{av}/U_{max} = 0.54$ ,  $d = 1.83$ , and (b)  $Re = 640$ ,  $V_{av}/U_{max} = 3.05$  and  $d = 2.06$ .

experiments, as a thinner boundary layer would lead to earlier bending of the jet, as the jet comes in contact with the maximum crossflow velocity closer to the lower wall. This can be seen in Figure 3.1a. The difference is less noticeable at higher velocity ratios, such as in Figure 3.1b, as the jet penetrates further beyond the boundary. The shape of the jet inlet profile is also significantly different, with Cambonie et al.'s experiments reporting an approximate profile that is more plug-shaped than parabolic. This would also contribute to the differences seen in the results, as plug-shaped velocity profiles lead to a larger proportion of the jet travelling at its maximum velocity, which allows for deeper penetration.

## 3.2 Comparison with published simulations

Trajectories and velocity profiles of simulations were compared to results reported in previous studies [40, 56, 59].

### 3.2.1 $Re = 1500$ , $V_{av}/U_{max} = 1.52$ , $d = 0.44$

Muppidi and Mahesh performed a direct numerical simulation (DNS) of a jet in crossflow using a finite volume method on an unstructured grid [30, 40]. The published centreline trajectory of Muppidi and Mahesh's simulation 3II was compared to the results of my simulation, run at  $Re = 1500$ ,  $V_{av}/U_{max} = 1.52$ , and  $d = 0.44$ , and shown in Figure 3.2.

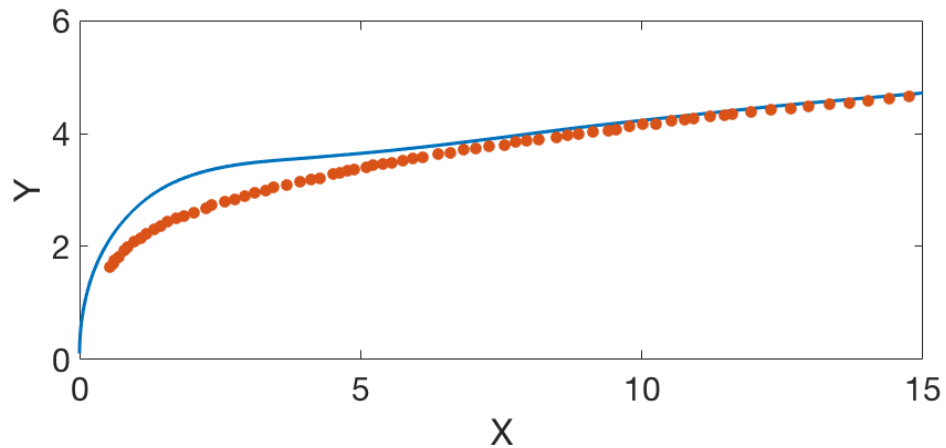


Figure 3.2: Centreline trajectory from my simulation (blue line) and that of Muppidi and Mahesh [40] (orange circles).

Close to the jet inlet, Figure 3.2 shows that the trajectory of my simulation is significantly different to the direct numerical simulation. In my simulation the jet penetrates more deeply into the crossflow before being deflected, and the deflection is much sharper. Muppidi and Mahesh's simulation shows a much more gradual deflection. Further away from the jet inlet the two simulations show very good agreement, matching position and angle almost exactly.

Muppidi et al. [40] report an 80% boundary layer thickness of 0.44, meaning that in their simulation when  $y = 0.44$  the velocity is 80% of its maximum. In my simulation the boundary layer reaches its maximum much closer to  $y = 0.44$ , resulting in a much thinner boundary layer. As a result, we would expect to see the trajectory of my jet bend much earlier, as it would interact with higher velocity flow closer to the jet inlet. This is not



the case. In section 3.3 ahead, it is shown that in my model the flow near to the jet inlet is not fully resolved on the computational grid, so the results are less accurate than a DNS. In this same area less than 80% of the kinetic energy is resolved by the large-scale model, so the sub-grid scale model is not performing as expected in this area. Because of this the results of my simulation close to the inlet are likely to be less accurate than a DNS.

Overall, although my LES does not match well with Muppidi and Mahesh's simulation close to the jet inlet, the agreement is much better far downstream of the jet inlet. The results are not exactly as would be expected due to the difference in boundary-layer thickness, but these differences may be explained by the behaviour of the turbulence model used in my simulation in the region near to the jet inlet.

### 3.2.2 $Re = 6930$ , $V_{av}/U_{max} = 3.3$ , $d = 0.5$

Yuan et al. performed a large-eddy simulation of a jet in crossflow using a finite volume method, with the turbulence model given by Zang et al. [59, 61]. Prior to entering the crossflow, the jet was simulated as a turbulent pipe flow for a short distance to produce a turbulent inlet velocity profile. Published velocity magnitude profiles were compared to my simulation, run for  $Re = 6930$ ,  $V_{av}/U_{max} = 3.3$ , and  $d = 0.5$ , and given in Figure 3.3.

In Figure 3.3a, the shape of the velocity magnitude profile for my simulation is quite similar to that of Yuan et al.'s simulation, although my simulation shows a slightly higher maximum velocity. In Figure 3.3b profiles of both my simulation and Yuan et al.'s simulations show two peaks. The higher of these peaks reach a similar maximum value, although Yuan's peak occurs closer to the lower wall of the domain. The centre of the lower peak falls at approximately the same  $y$  value, although the heights are quite different, with my simulation showing a broader, shallower peak. In Figures 3.3c and 3.3d, the higher peak again takes approximately the same value, but the position of the peaks in Yuan's simulation is closer to the lower wall. In my simulations the lower peak is better defined, with a deeper trough separating the two peaks.

The differences between the profiles of the simulations are caused by the difference in jet velocity that can be seen at the centre of the jet,  $x = 0$ , in Figure 3.3a. The larger transverse velocity causes a deeper penetration of the jet, shifting the upper peak away from the lower wall at each  $x$  position. Yuan et al. simulate a turbulent flow in a pipe for a short distance, which is used for the jet inlet velocity profile, while my simulation uses a laminar profile at the jet inlet. This pipe flow simulation modifies the shape of the jet velocity profile enough to cause the visible differences between the simulations.

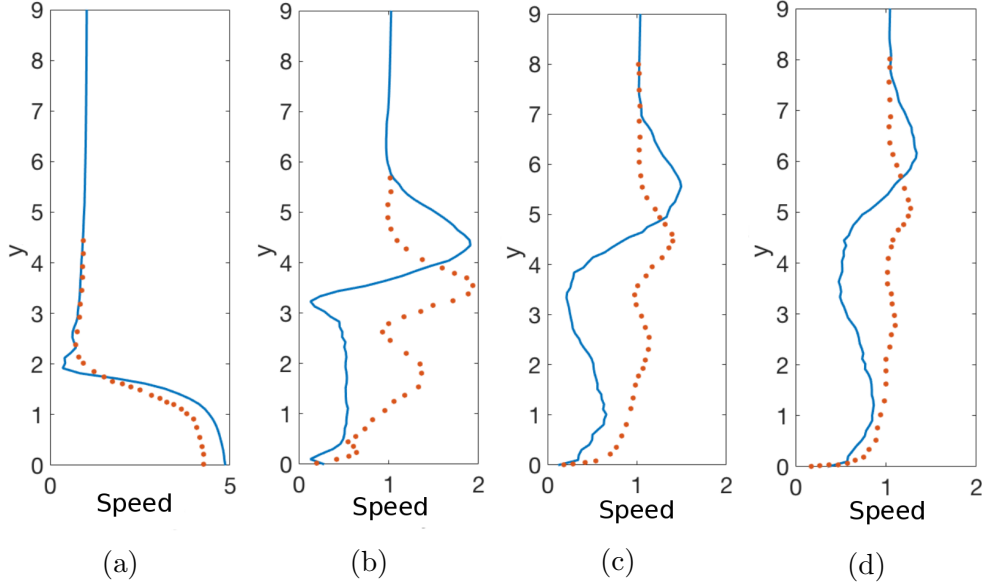


Figure 3.3: Velocity magnitude profiles in the jet centreline,  $z = 0$ , from my simulation (blue lines) and Yuan et al. [59] (orange circles). Profiles are given at (a) the centre of the jet inlet at  $x = 0$ , and downstream of the jet inlet at (b)  $x = 1.84$ , (c)  $x = 3.67$  and (d)  $x = 5.54$ .

Yuan et al. use a cylindrical mesh around the jet inlet to better capture the circular boundary conditions that define the jet inlet [59]. This was not done in my simulation, so the shape of the jet in my simulation is not exactly circular. The grid in my simulation is also not as refined as that of Yuan et al., as a finer grid would have led to unreasonable computational expense. These issues will have had an overall effect on the accuracy of my simulation. Yuan et al. also use a different sub-grid scale turbulence model in their LES.

Despite the differences, there is a recognisable qualitative agreement between the two simulations. The differences that are seen can be attributed to the differences in jet inlet velocity profile and model used. This shows that, for this particular set of parameters, my simulation is performing reasonably well.

### 3.2.3 $Re = 20500$ , $V_{av}/U_{max} = 0.5$ , $d = 1$

Wegner et al. [56] performed a large-eddy simulation of a jet in crossflow using a second order central collocated numerical solver and a Smagorinski model to approximate the sub-grid stresses and flux. Following Wegner et al., transverse profiles of single velocity components and scalar concen-

tration, as well as the turbulent kinetic energy (TKE) were plotted for a number of points both up and downstream of the jet inlet for  $Re = 20500$  and  $V_{av}/U_{max} = 0.5$ . The boundary layer thickness  $d$  was not specified by Wegner et al., so it was chosen as  $d = 1$  to approximately match Wegner et al.'s streamwise velocity profile upstream of the jet. These were compared to the published velocity and scalar concentration profiles of a jet entering perpendicularly to a crossflow.

Profiles of the streamwise component of velocity,  $u$ , have similar trends although the maximum velocity  $u = 1$ , occurs further from the lower wall in my simulation than in that of Wegner et al. at every  $x$  position. Upstream of the jet centre point, in Figures 3.4a and 3.4b, this is due to a difference in boundary layer thickness. In both of these figures the boundary layer in my simulation appears to be thicker, however as both  $x = -0.5$  and  $x = -0.25$  are within the jet inlet region the profiles are impacted by the jet. Wegner et al. did not publish velocity profiles from further upstream so the thickness of the boundary layers could not be compared without the impact of the jet. Downstream of the jet inlet, the peak velocity occurring further from the wall indicates deeper penetration of the jet into the crossflow.

Within the jet inlet region,  $x = -0.5$  to  $0.5$ , Figure 3.5 shows the transverse velocity component  $v$  is higher in my simulation than in Wegner's results, however further from the wall they show good agreement, with  $v$  decaying to 0 in both cases. The transverse velocity at the inlet is different because Wegner et al. simulate a short region of pipe flow before the jet enters the domain, whereas I assume that the jet enters the crossflow with a parabolic profile. Wegner et al.'s jet profile also appears to be asymmetric, indicating that the jet inflow is affected by the crossflow while it is still within the pipe. In my simulation the jet inflow is fixed by the inlet boundary condition, which contributes to the deeper penetration of the jet seen in the results of my simulation.

A significant difference between the profiles can be seen in Figure 3.5e, close to the lower wall, where Wegner et al.'s simulation shows a peak very close to the lower wall that takes a maximum value close to one, whereas my simulation shows remains close to zero at the same position. The cause of this peak in Wegner et al.'s simulation at  $x = 0.5$  is unknown, and no similar peak can be seen in their simulation at either of the surrounding points,  $x = 0.25$  or  $x = 1$ . Further downstream the two simulations show good agreement, with slightly less penetration seen in Wegner's results.

Within the jet inlet, concentration profiles given in Figures 3.6a to 3.6c show qualitative agreement between my simulation and Wegner et al.'s results, however the jet appears to penetrate slightly more deeply in my simulation, which is consistent with the streamwise velocity profiles. The deeper

penetration seen in my simulation is not surprising as the transverse velocity at the centre of the jet inlet is larger in my simulation. In Figures 3.6d and 3.6e the concentration of the scalar close to the wall is significantly less for my simulation, however it shows a peak at around  $y = 0.75$  that takes a similar value to the maximum seen in Wegner et al.'s results. The concentration peak in my simulation is in the same position as the streamwise velocity peak in Figure 3.4f, suggesting that, in my simulation, more of the scalar is being carried in the jet plume itself than in the region between the jet plume and the wall, whereas in Wegner et al.'s simulation the concentration of the scalar is fairly consistent between the lower wall and the top of the jet. Further downstream, in Figure 3.6f the two simulations are in much closer agreement.

Within the jet inlet region peaks in the turbulent kinetic energy (TKE) in my simulation are significantly larger than those in Wegner et al.'s results, however their location is similar. Further downstream the transverse location of the peaks is more noticeably different, although the amplitudes are more consistent, with the kinetic energy peak occurring further from the lower wall in my simulation. This is consistent with the deeper penetration of the jet that has been deduced from the velocity and scalar profiles. Wegner et al. include the sub-grid TKE in their plots [56], which I have not done. The inclusion of the sub-grid TKE in my simulation will lead to less similar results.

Overall, the results of the two simulations are quite similar, with a slight difference in penetration of the jet the most noticeable difference. Most differences that can be seen between the two simulations is explained by the difference in velocity at the jet inlet, caused by the different methods of calculating the jet inlet velocity profile.

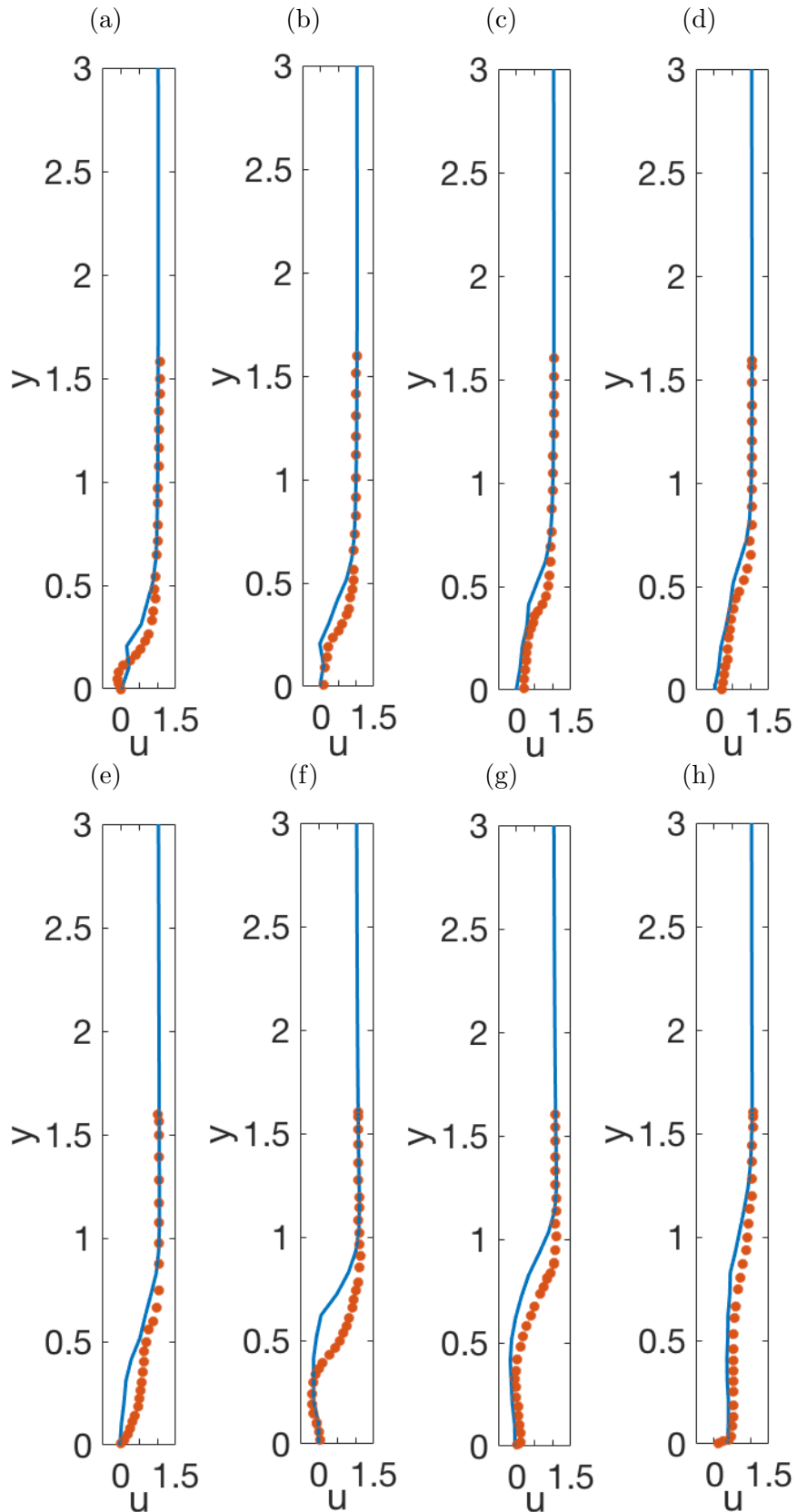


Figure 3.4: Streamwise velocity profiles for my simulation (blue lines) and Wegner et al. [56] (orange circles). Profiles given at (a)  $x = -0.5$ , (b)  $x = -0.25$ , (c)  $x = 0$ , (d)  $x = 0.25$ , (e)  $x = 0.5$ , (f)  $x = 1$ , (g)  $x = 2$ , and (h)  $x = 4$ .

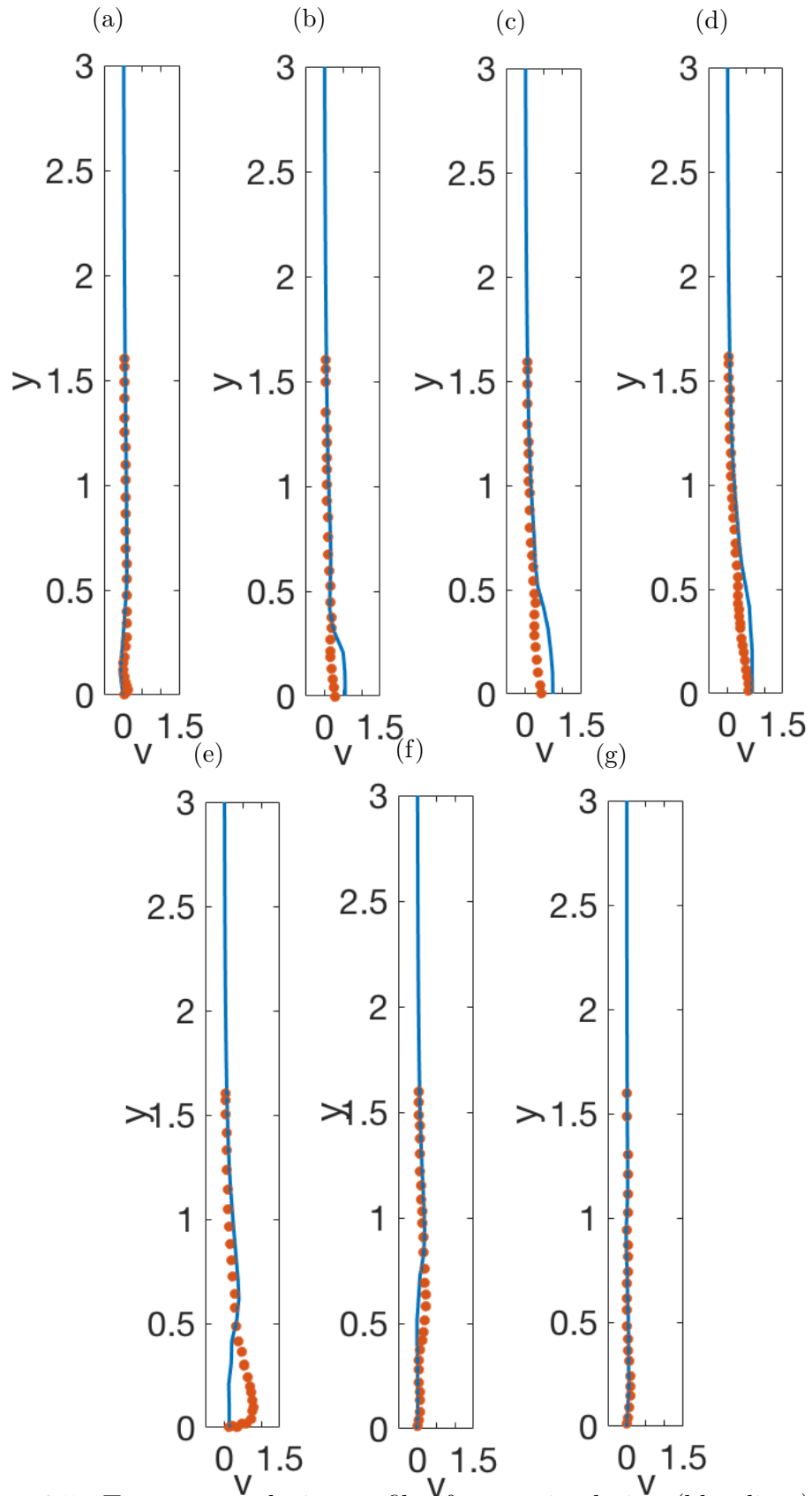


Figure 3.5: Transverse velocity profiles for my simulation (blue lines) and Wegner et al. [56] (orange circles). Profiles given at (a)  $x = -0.5$ , (b)  $x = -0.25$ , (c)  $x = 0$ , (d)  $x = 0.25$ , (e)  $x = 0.5$ , (f)  $x = 1$ , and (g)  $x = 2$ .

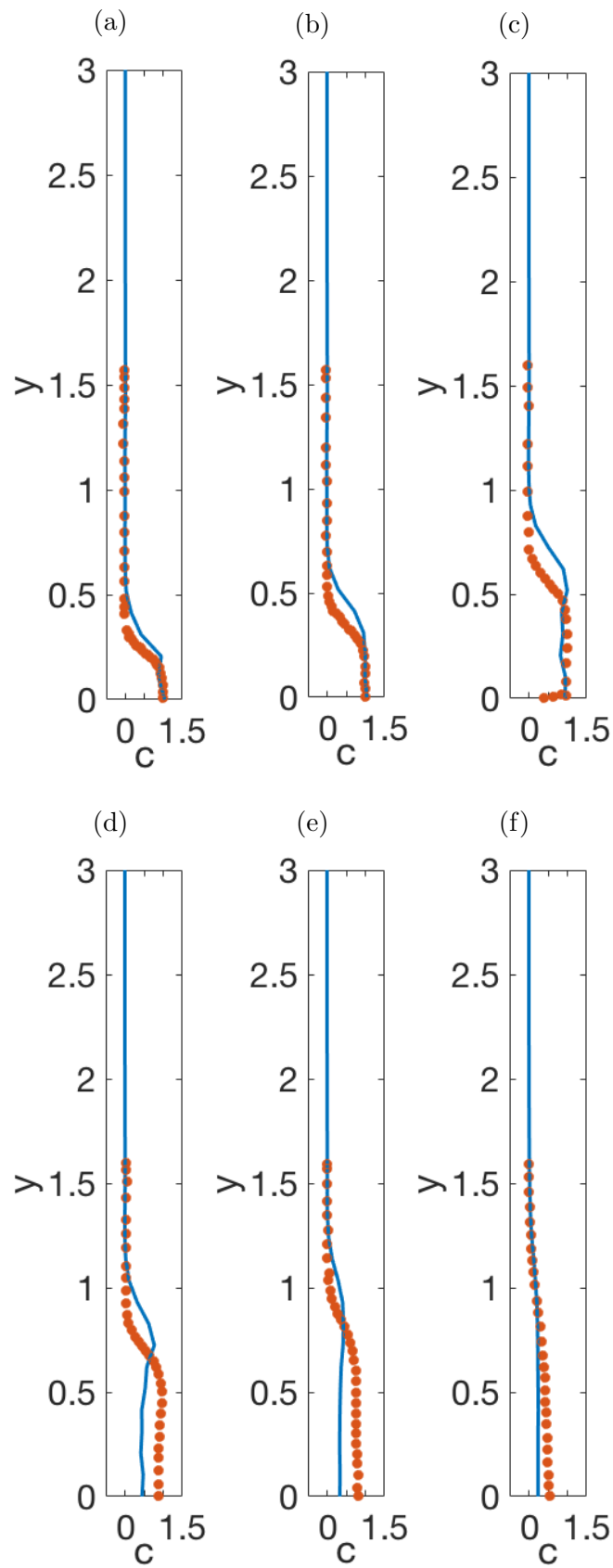


Figure 3.6: Concentration profiles for my simulation (blue lines) and Wegner et al. [56] (orange circles). Profiles given at (a)  $x = -0.25$ , (b)  $x = 0$ , (c)  $x = 0.5$ , (d)  $x = 1$ , (e)  $x = 2$ , and (f)  $x = 4$ .

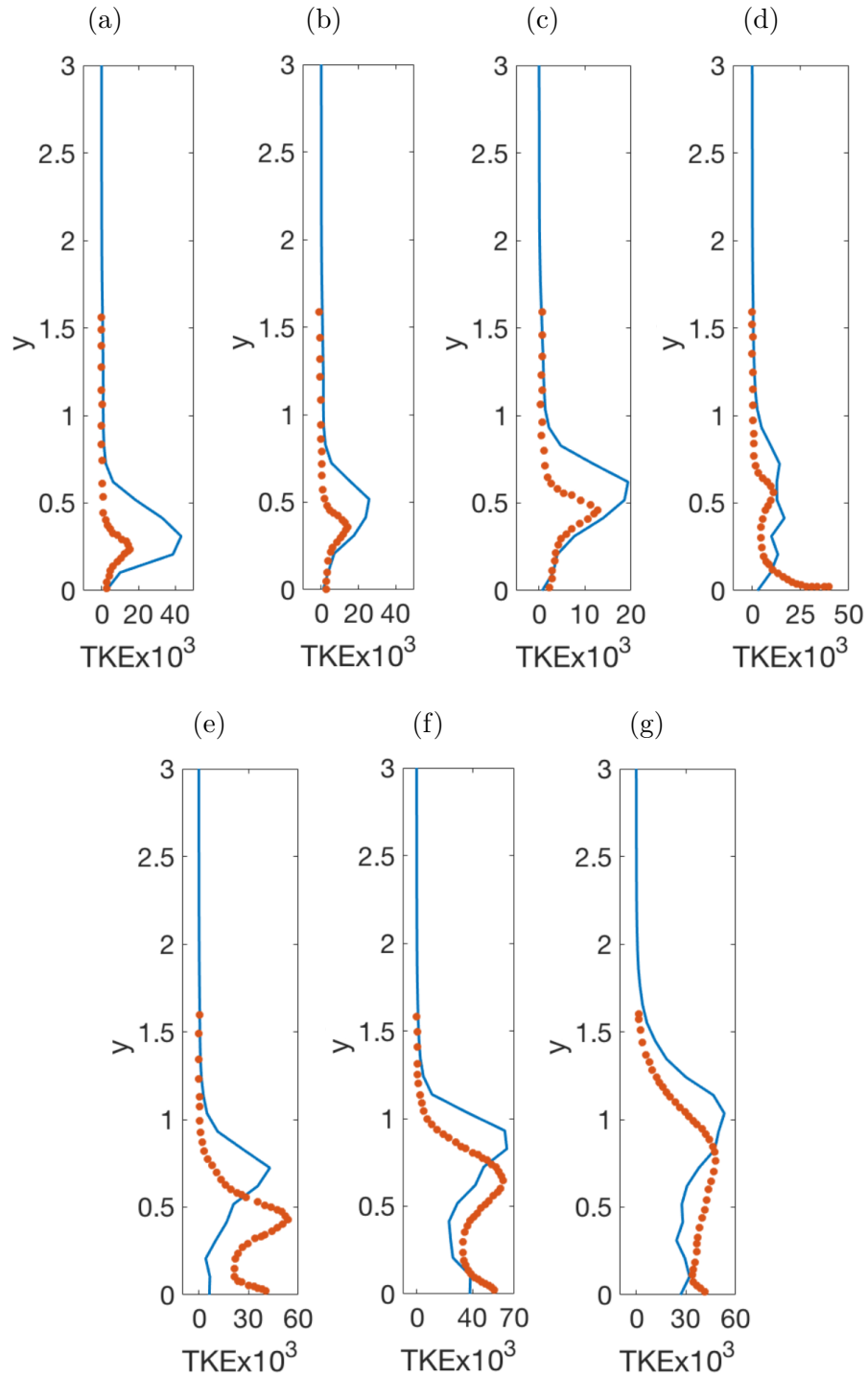


Figure 3.7: Turbulent kinetic energy profiles for my simulation (blue lines) and Wegner et al. [56] (orange circles). Profiles given at (a)  $x = -0.25$ , (b)  $x = 0$ , (c)  $x = 0.25$ , (d)  $x = 0.5$ , (e)  $x = 1$ , (f)  $x = 2$ , and (g)  $x = 4$ .



### 3.3 Verification against an alternative LES code

An LES code using a fourth-order central finite-difference method in all three spatial directions and a low-storage third order Runge–Kutta timestepper was provided by Trent Mattner in order to ascertain the effect of the numerical method on the solution of an LES. In the streamwise and transverse directions, it is expected that the fourth-order scheme will be more accurate than the hybrid scheme, as in the hybrid scheme these directions use a second-order accurate method. In the cross-stream direction, the hybrid scheme is expected to be more accurate, as a spectral scheme is used in this direction.

The two codes were run on the same domain with the same sub-grid model. The boundary conditions were almost the same, but a slip boundary condition was applied on the upper and lower walls in the simulation using Mattner’s code. Parameters were chosen as  $Re = 2 \times 10^4$ ,  $V_{av}/U_{max} = 2.25$  and  $d = 1$ . Trajectories, velocity and scalar concentration profiles, spectra and contour plots of turbulent kinetic energy ratio were calculated for both of these simulations.

#### 3.3.1 Trajectories

Time averaged centreline, concentration and counter-rotating vortex pair (CVP) trajectories were calculated in the jet centreplane,  $z = 0$ .

The centreline trajectories of Mattner and my simulations, shown in Figure 3.8a follow the same curve close to the jet inlet. Travelling downstream the centreline trajectory of my simulation falls lower than that of Mattner’s, with a maximum deviation of approximately 0.6 of the jet diameter. This suggests that Mattner’s fourth-order accurate method maintains the transverse velocity of the jet for longer. A similar trend is seen in the concentration trajectory, in Figure 3.8b.

Although once again following a similar course close to the jet inlet, the CVP trajectories shown in Figure 3.8c are significantly different downstream of the jet. The trajectory of my simulation drops from the initial high much closer to the jet, and also drops a longer distance, remaining lower for the rest of the length of the domain. The later drop of Mattner’s simulation reflects the deeper penetration of both the centreline and concentration trajectories, indicating that upwards momentum is conserved for longer in this simulation.

In Figure 3.9 we examine cross-stream contour plots of the transverse velocity component  $v$  at a number of points downstream of the jet. From

these, the cause of the difference in drop distance can be seen. While there are at most two local transverse velocity maxima in each cross-section of my simulation, there are often three in Mattner's simulation, as can be seen in Figures 3.9b and 3.9c. The upper and lower of these maxima seem to correspond to the two maxima of my simulation, while the third, falling between the other two, is not present in my simulation.

Despite the noticeable differences in the CVP trajectory, the both the contour plots of transverse velocity in Figure 3.9 and the transverse velocity profiles in Figure 3.11 are broadly similar. This indicates that the calculation of the CVP trajectory by the locus of maximum transverse velocity is sensitive to minor variations in the flow. It suggests that the numerical method that is used will have a strong impact on the nature of this trajectory.

### 3.3.2 Velocity and Scalar Profiles

Profiles of individual velocity components,  $u$  and  $v$ , and scalar concentration,  $c$ , were plotted at  $z = 0$  at a number of points up and downstream of the jet inlet for both my simulation and Mattner's simulation, as shown in Figures 3.10 - 3.12. No profiles were produced for the cross-stream velocity component,  $w$ , as the magnitude of this velocity component was very small in both simulations.

Overall, these show both qualitative and quantitative agreement, although the profiles of Mattner's simulation are smoother than those of my simulation. In the streamwise velocity and scalar concentration profiles, differences near the upper and lower walls are caused by different boundary conditions.

Upstream of the jet inlet (Figures 3.10a, 3.11a and 3.12a), there is variation between the two simulations in the lower half of the region, particularly noticeable in the vertical velocity and scalar concentration. The fluctuations seen in all three upstream profiles are numerical artifacts, caused by dispersion effects as described by Trefethen [52] and Matheou and Dimotakis [33]. The range over which these variations occur is small, with the range in Mattner's simulations being smaller, as would be expected for a method that is more accurate in the  $x$  and  $y$  directions [33].

In the streamwise velocity profiles ( $u$ ), for  $x \geq 4$ , it can be seen that the main peak caused by the jet begins closer to the lower wall for my simulation than it does for Mattner's simulation, the difference becoming more pronounced further downstream. This correlates with the difference in centreline trajectory seen in Figure 3.8a. The transverse velocity profiles in Figure 3.11 are quite similar between the two simulations, but it is possible to see the different values and positions of the local maxima, corresponding to those seen in Figure 3.9.

In the scalar concentration profiles, the maximum concentration values for Mattner's simulation are higher than those for my simulation. These maxima occur closer to the upper wall and are part of peaks that are more skewed towards the upper wall, whereas the peaks in my simulation are less skewed. The overall width of the peaks is fairly consistent between the two simulations. The position of the maxima in the two simulations corresponds with the differences in centreline and concentration trajectories seen in Figure 3.8. The amplitude of the peaks indicates that more of the crossflow fluid is being entrained into the jet in my simulation, making the jet more dilute.

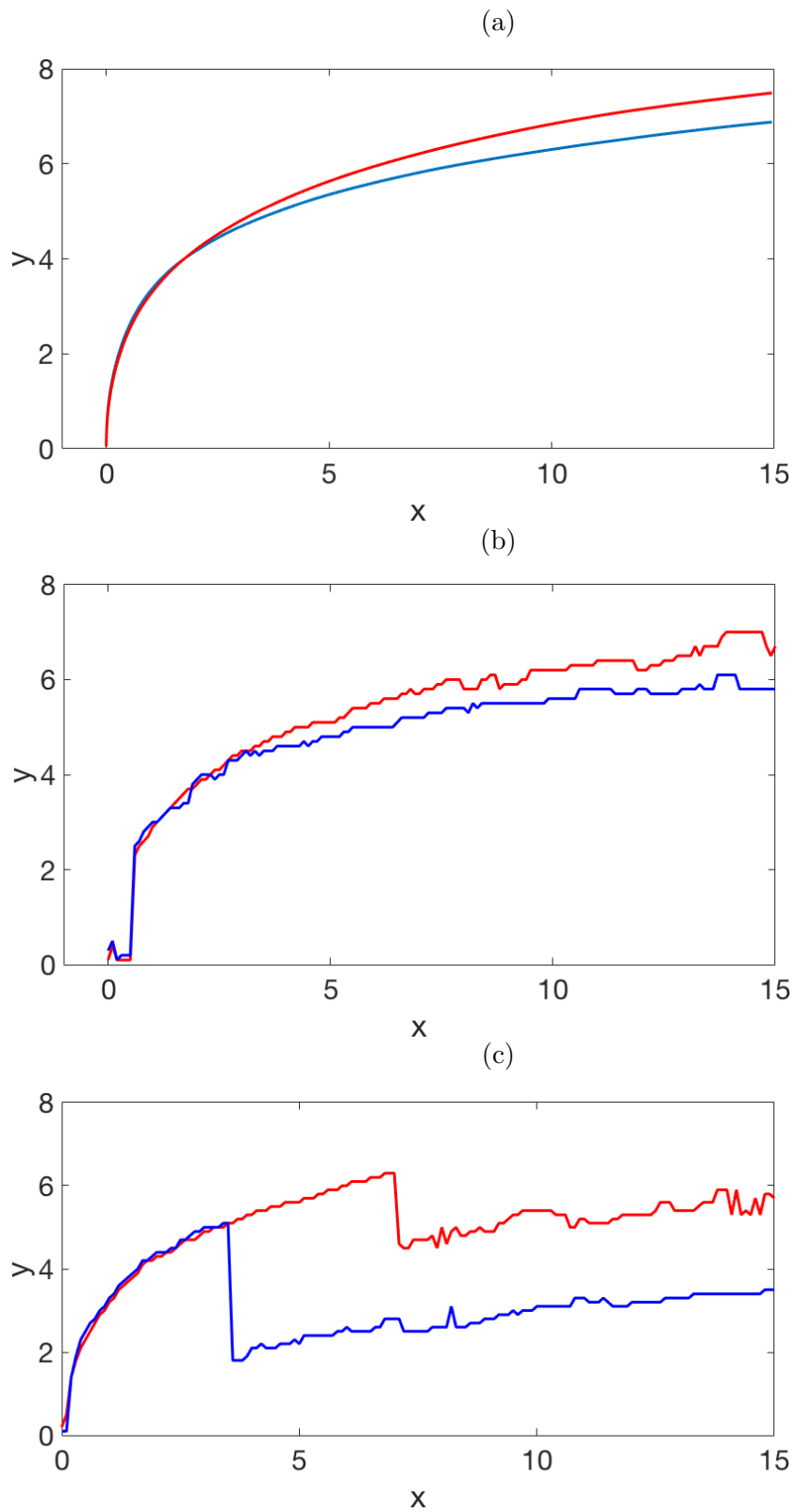


Figure 3.8: (a) Centreline, (b) concentration and (c) CVP trajectories of my simulation (blue) and Mattner's simulation (red).

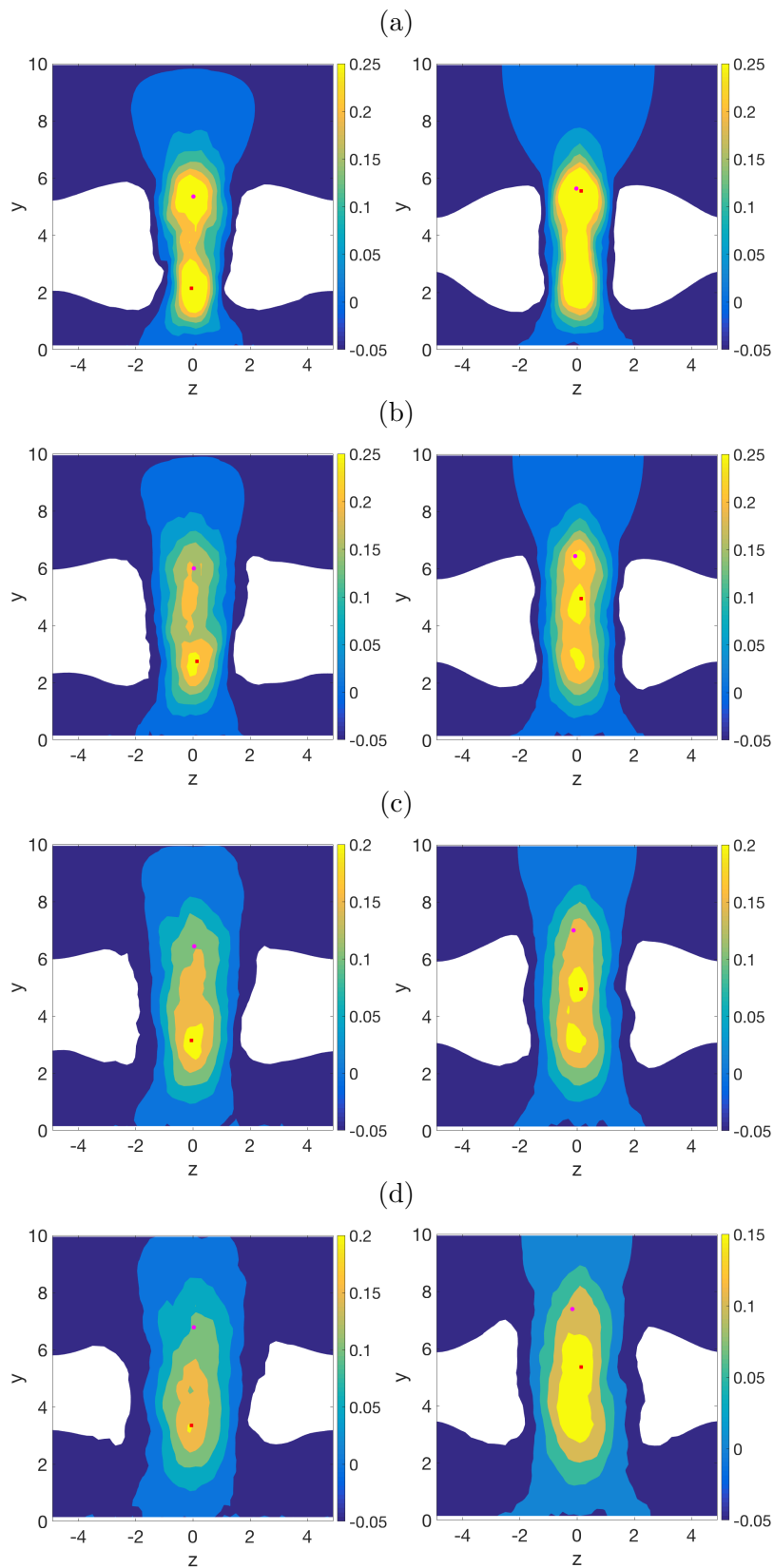


Figure 3.9: Contours of vertical velocity in the cross section at (a)  $x = 5$ , (b)  $x = 8$ , (c)  $x = 11$  and (d)  $x = 14$ , for my simulation (left) and Matner's simulation (right). Also shown are the positions of the jet centreline trajectory (magenta circle) and CVP trajectory (red square). White areas are regions where the vertical velocity is less than -0.05.

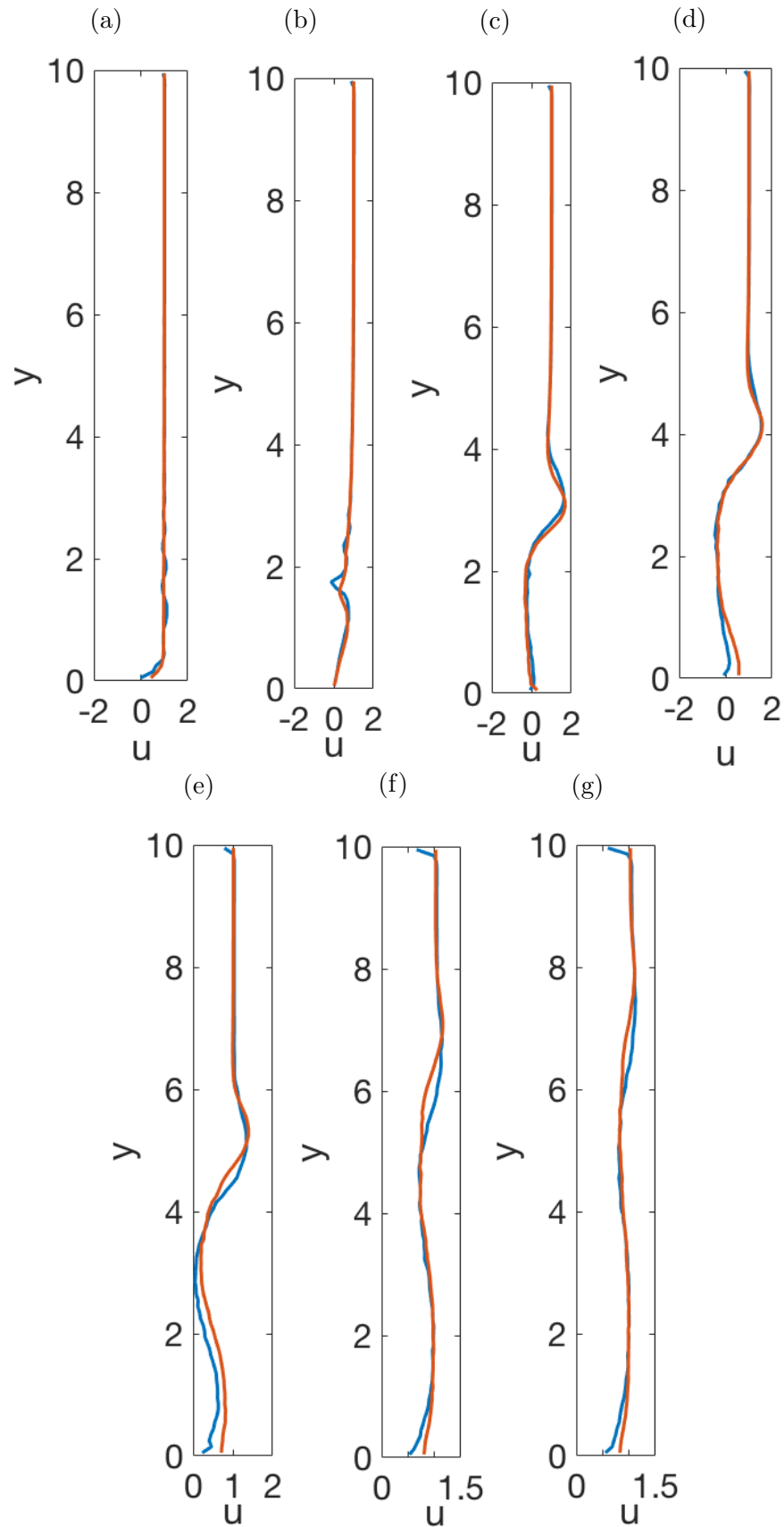


Figure 3.10: Streamwise velocity profiles for my simulation (blue lines) and Mattner's simulation (orange lines) at (a)  $x = -2.5$ , (b)  $x = 0$ , (c)  $x = 1$ , (d)  $x = 2$ , (e)  $x = 4$ , (f)  $x = 10$ , (g)  $x = 14$ .

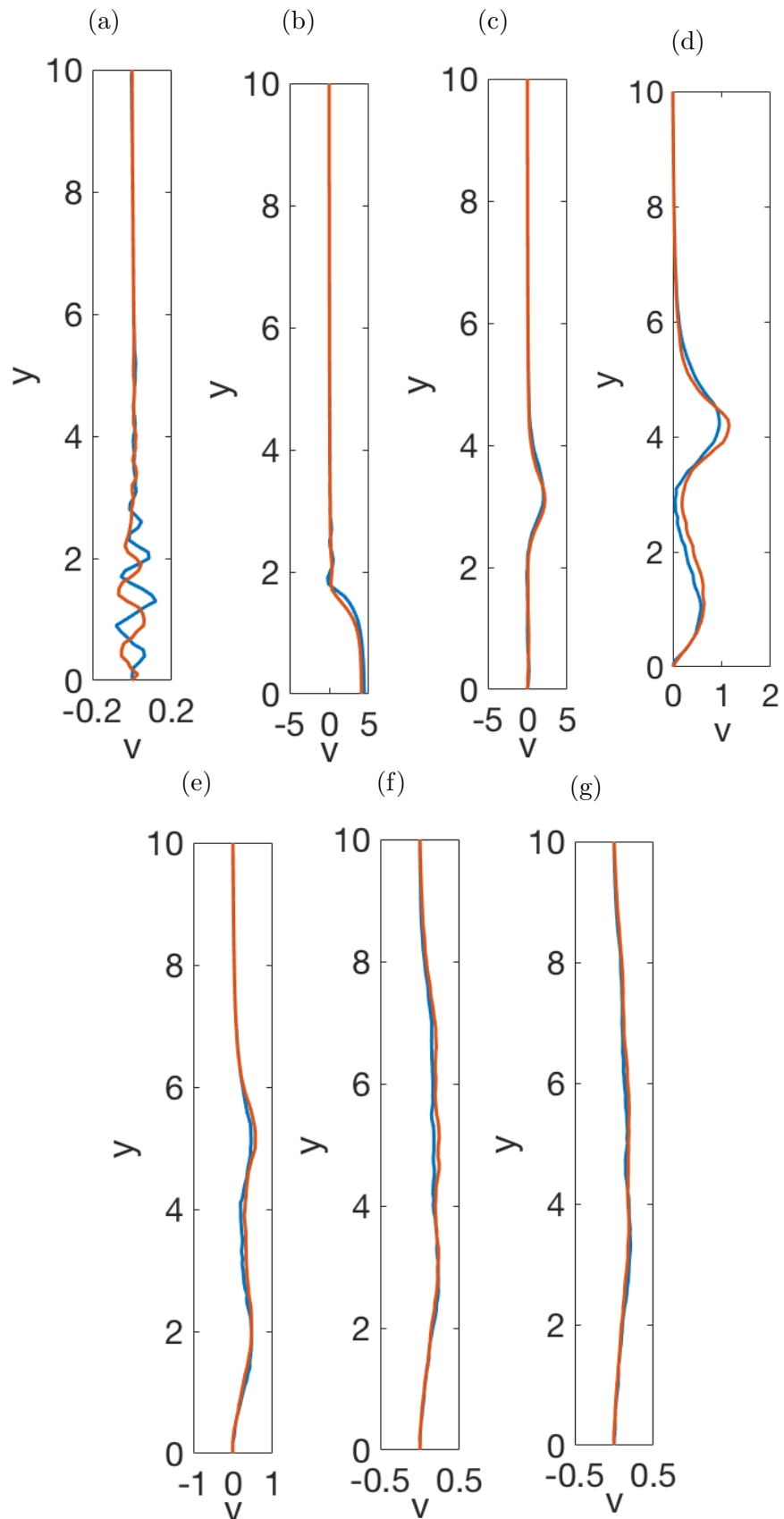


Figure 3.11: Transverse velocity profiles for my simulation (blue lines) and Mattner's simulation (orange lines) at (a)  $x = -2.5$ , (b)  $x = 0$ , (c)  $x = 1$ , (d)  $x = 2$ , (e)  $x = 4$ , (f)  $x = 10$ , (g)  $x = 14$ .

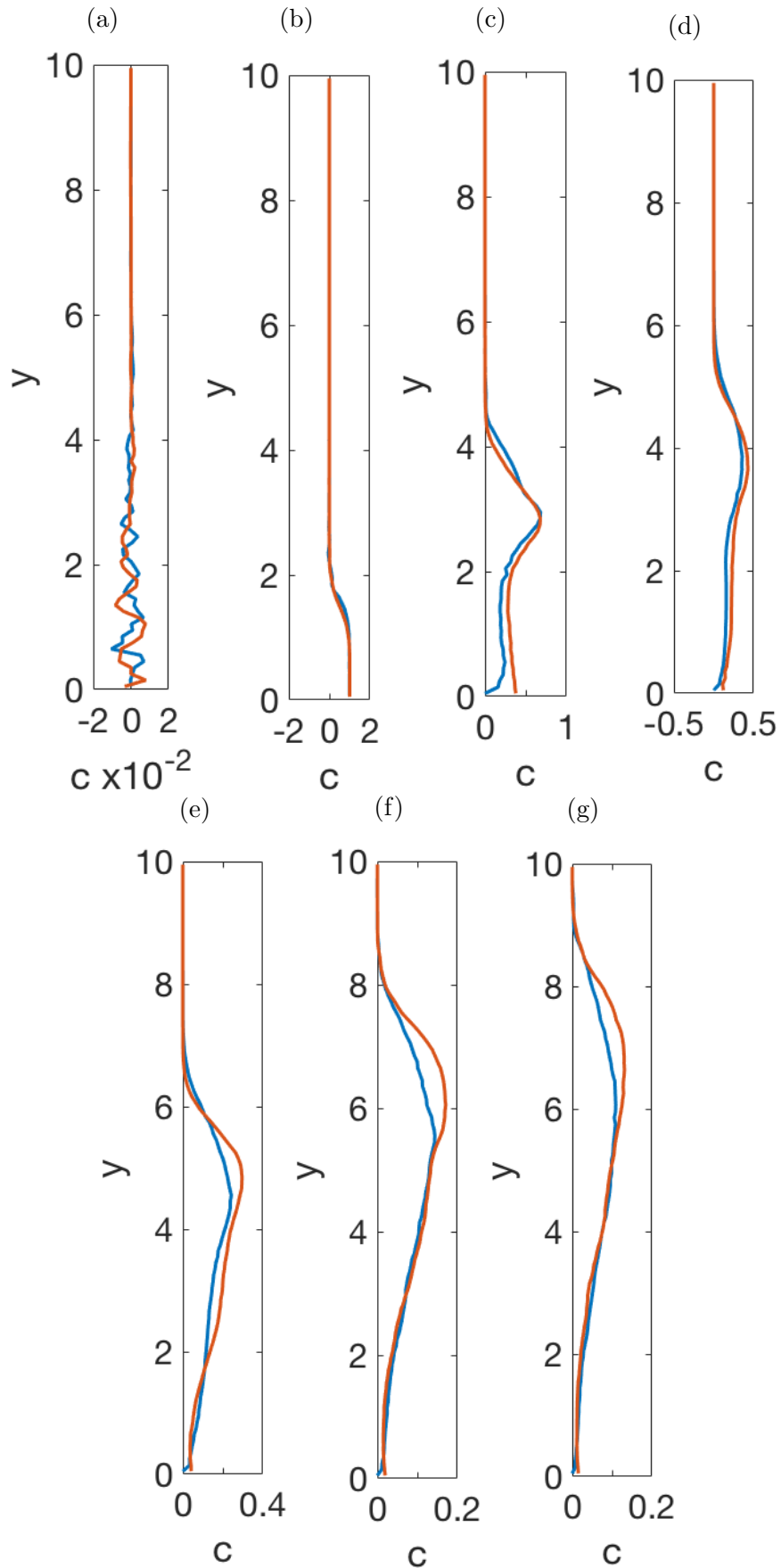


Figure 3.12: Scalar concentration profiles for my simulation (blue lines) and Mattner's simulation (orange lines) at (a)  $x = -2.5$ , (b)  $x = 0$ , (c)  $x = 1$ , (d)  $x = 2$ , (e)  $x = 4$ , (f)  $x = 10$ , (g)  $x = 14$ .



### 3.3.3 Spectral density

Time averaged spectra of turbulent kinetic energy and scalar concentration were calculated in the  $z$  direction for my simulation and Mattner's simulation at  $x = 7.7$ , as this point is far enough from the jet inlet for the turbulent flow to be developed, and far enough from the outlet to be unaffected by the outlet boundary conditions. The  $y$  coordinate for the spectra calculation was chosen to correspond to the centreline trajectory at this point. This gave positions of  $(x, y) = (7.7, 5.9)$  and  $(x, y) = (7.7, 5.0)$  for my simulation and Mattner's simulation respectively.

Overall the spectra of the two simulations show good qualitative and quantitative agreement, particularly at low and medium wavenumbers. There is some deviation at higher wavenumbers, most significantly in the spectrum of the scalar concentration, in Figure 3.13b. Both of the spectra show a slope close to the desired  $-\frac{5}{3}$  slope at higher wavenumbers.

A small hook can be seen near the high wavenumber end of Figure 3.13b for my simulation, which suggests that more energy than would be expected is building up in the high wavenumber region. The corresponding spectrum for Mattner's simulation shows only a minor hook, indicating a more accurate simulation. These hooks can be attributed to two main numerical causes. The first of these causes is aliasing, where the energy that should be attributed to wavenumbers higher than those used for the discrete Fourier transform is misinterpreted as belonging to wavenumbers within the calculated range [53]. This is connected to the way the non-linear terms are calculated. Aliasing errors indicate that too few discrete modes are being used to represent the flow [7], which is to be expected for a LES. The other possible cause of the build up of energy in the upper end of the spectra relates to the sub-grid scale stress and flux models used for the large-eddy simulation. The vortex alignment model used, Misra and Pullin's model 1b [37], allows for the backscatter of energy from the sub-grid scales to the resolved scales of the flow. While this is desirable to some extent, too much backscatter leads to more energy than expected appearing in the high wavenumber regions of the resolved flow.

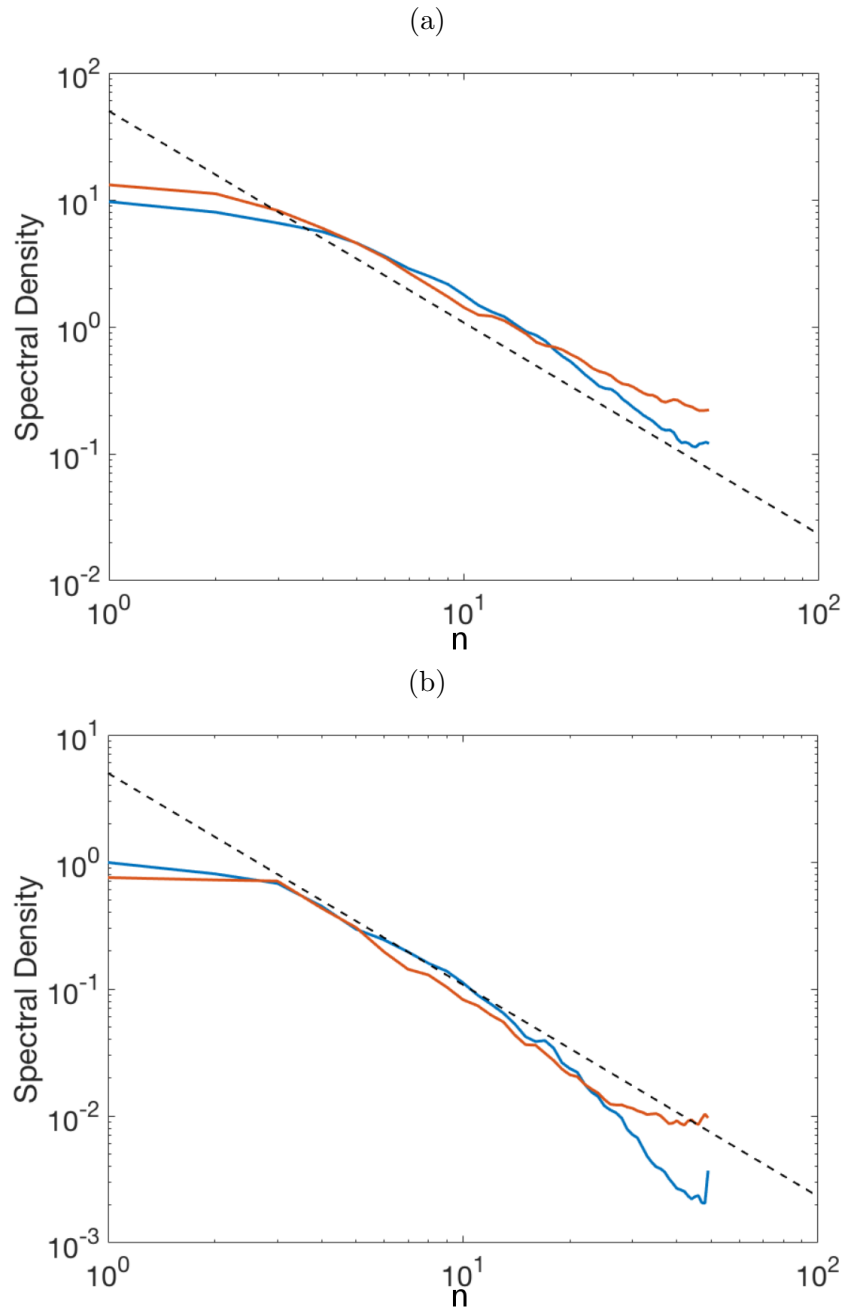


Figure 3.13: Time averaged spectral density of velocity components, (a) kinetic energy and (b) scalar concentration, taken at  $(x, y) = (7.7, 5.9)$ , for my simulation (blue) and  $(x, y) = (7.7, 5.0)$  for Mattner's simulation (red). Black dashed line has ideal  $-\frac{5}{3}$  slope.

### 3.3.4 Turbulent Kinetic Energy

The turbulent kinetic energy ratio,  $K_{rat} = \frac{K}{K+K^{SGS}}$ , as calculated in section 2.6.6, is plotted in Figure 3.14 along the jet centreline,  $z = 0$  for the two simulations, to compare the extent to which the large-scale model resolves the kinetic energy. In both simulations the desired 80% ratio is not achieved near the jet inlet. In my simulation it appears that little to none of the TKE is resolved on the computational grid, as shown by the dark blue area, while in Mattner's simulation it appears that at least 30% of the TKE is resolved by the large scale, shown by the lighter shade of blue. In both simulations, this could be fixed by using a more refined grid close to the jet inlet. Away from the jet inlet, both simulations achieve the desired 80% ratio, as shown by the orange contour.

Along the upper wall of the domain, my simulation shows a thin region in which less than 80% of the TKE is resolved by the large scale equations. This region is not present in Mattner's simulation. This is caused by the difference in boundary conditions on this wall.

The other observable difference between the two simulations is the streaking of low values of  $K_{rat}$  upstream of the jet inlet. While this does appear in both simulations, it occurs only near the lower wall for Mattner's simulation, while in my simulation it continues to appear quite a distance from the wall. This upstream streaking is a result of numerical dispersion caused by the use of finite difference methods [52], and matches what can be seen upstream of the jet in the velocity and scalar concentration profiles.

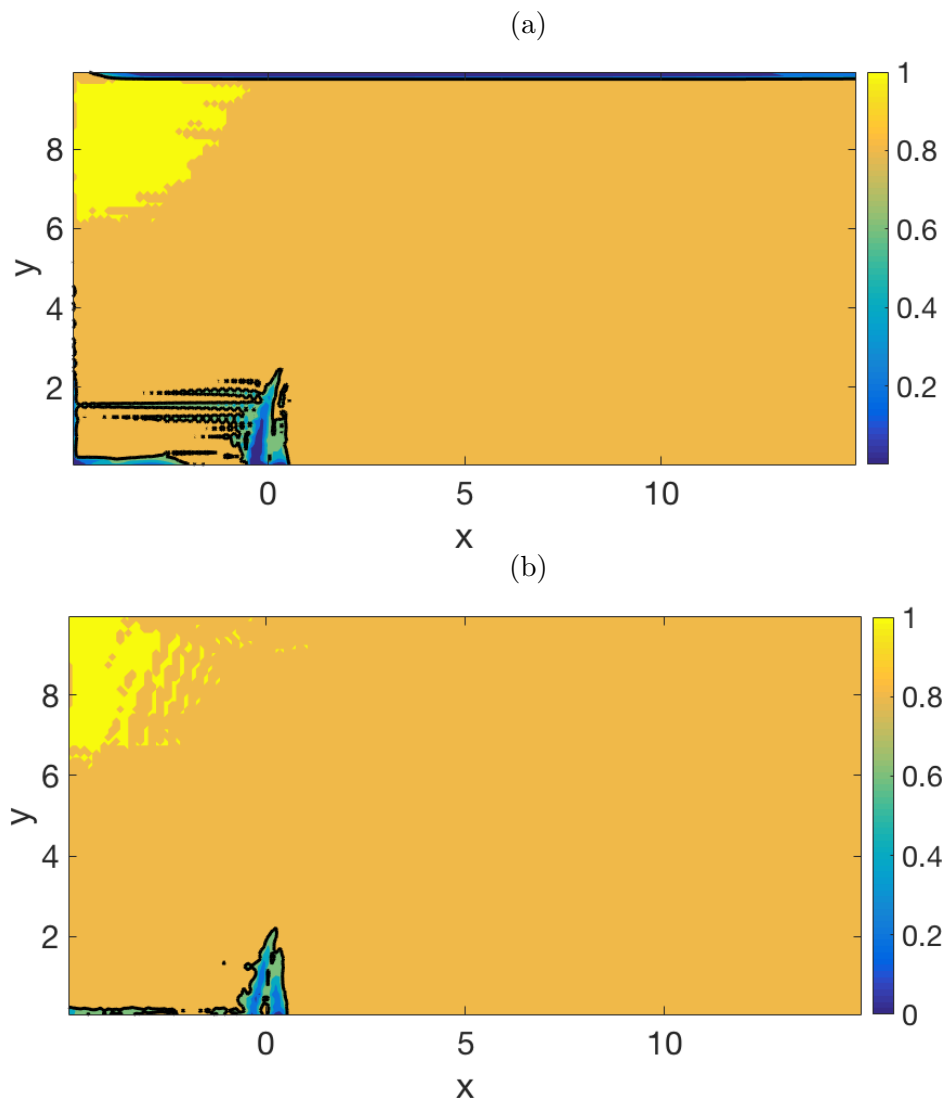


Figure 3.14: Contour plots of turbulent kinetic energy ratio at  $z = 0$ , with 0.8 contour marked in black for (a) my simulation and (b) Mattner's simulation.

### 3.3.5 Dissipation and Kolmogorov length scale

Large and sub-grid scale dissipation were calculated for all points on the centreplane,  $z = 0$ , for both my simulation and Mattner's simulation to ascertain the effect of the numerical method on energy loss and energy transfer between scales. The Kolmogorov length ratio,  $\eta/\Delta x$ , is also calculated to determine the necessity of using a sub-grid scale model.

Figure 3.15 shows contours of  $\log(\varepsilon^{SGS}/\varepsilon^{LS})$ . The black contour indicates the points where  $\log(\varepsilon^{SGS}/\varepsilon^{LS}) = 0$ , equivalent to  $\varepsilon^{SGS}/\varepsilon^{LS} = 1$ , which is where the sub-grid and large-scale dissipation is equal, separating the regions where the large-scale and sub-grid dissipation dominate. Close to the inlet, both my simulation and Mattner's simulation show positive values of  $\log(\varepsilon^{SGS}/\varepsilon^{LS})$ , indicating that the sub-grid scale dissipation dominates. The region in which this is true is larger in Mattner's simulation. Further downstream, where the values of  $\log(\varepsilon^{SGS}/\varepsilon^{LS})$  are negative, the values seen in Mattner's simulation are less negative than those of my simulation for the full length of the domain. This indicates that Mattner's simulation is producing either less large scale dissipation or more sub-grid scale dissipation than my simulation.

Figure 3.16 shows contours of the Kolmogorov length scale ratio,  $\eta/\Delta x$ . In both simulations, this ratio is less than one at all points, indicating that the smallest eddies are smaller than the computational grid. In the region surrounding the jet inlet, where the turbulence has not yet developed, my simulations shows a ratio of close to zero, while Mattner's ratio is closer to 0.1. Both of these values are very small, but the difference indicates that Mattner's simulation is more resolved. This difference in ratio continues downstream of the jet for the full length of the domain.

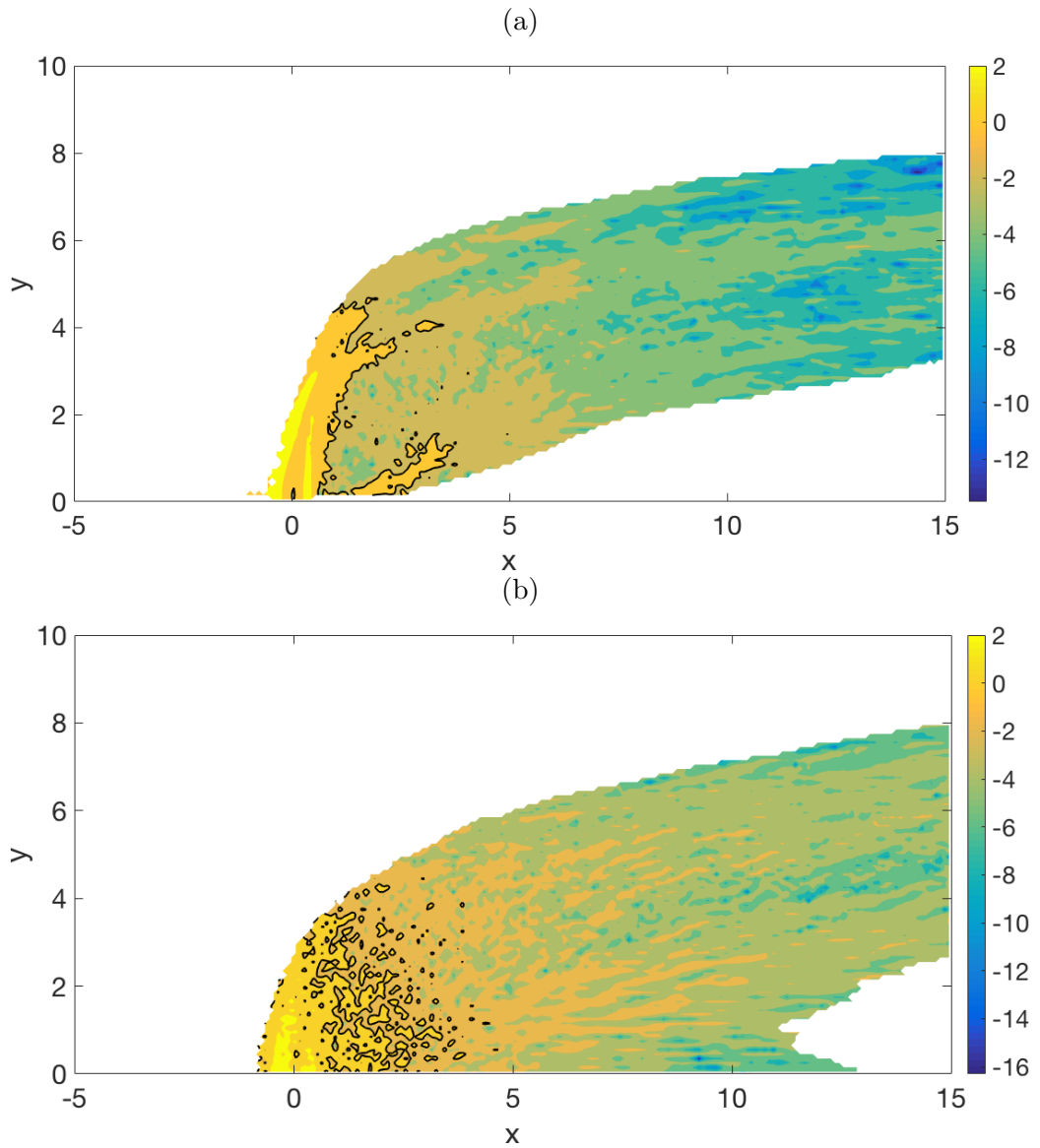


Figure 3.15: Logarithm of point-wise dissipation ratio on plane  $z = 0$  for regions where scalar concentration  $c \geq 0.05$  for (a) my simulation and (b) Mattner's simulation. Black line shows contour where  $\log(\varepsilon_{\text{SGS}}/\varepsilon_{\text{LS}}) = 0$ .

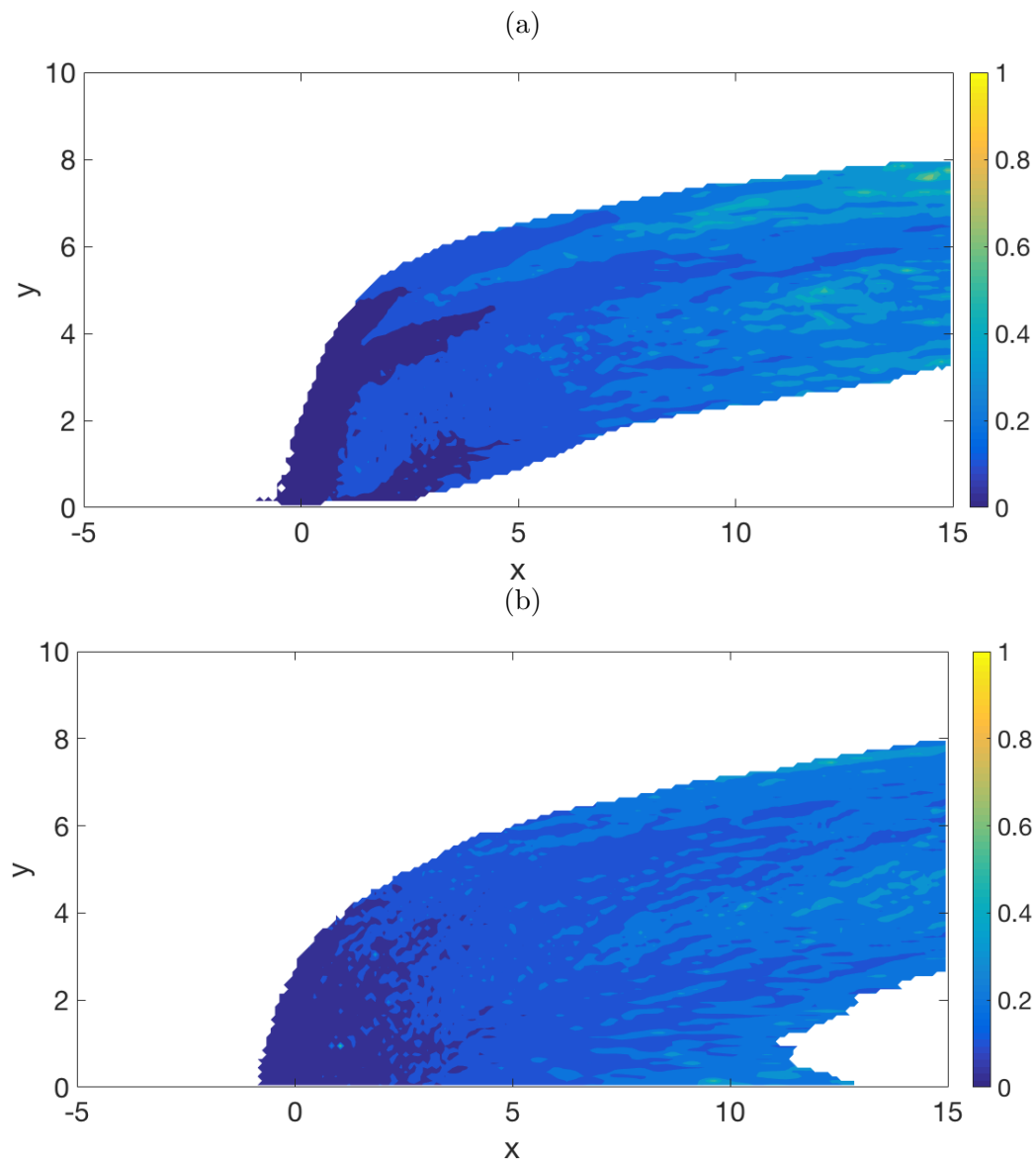


Figure 3.16: Point-wise Kolmogorov length scale ratio on plane  $z = 0$  for regions where scalar concentration  $c \geq 0.05$  for (a) my simulation and (b) Mattner's simulation.

### 3.4 Conclusion

For low velocity ratio flows interacting closely with the lower wall of the simulation domain, such as those shown in sections 3.1 and 3.2.3 above, my simulations show only reasonable qualitative agreement to the published results. This is seen at both low and high Reynolds number. The poor agreement is caused by a combination of interactions with the no-slip boundary condition, chosen to justify the artificial boundary layer velocity profile at the crossflow inlet, and the lack of boundary assumptions in the LES model used.

For jets that have higher velocity ratios, and thus penetrate further into the crossflow, the differences between our results and those of previous studies are much smaller, as there is less interaction between the jet and the no-slip boundary conditions. Quantitative differences that can be seen, such as those in section 3.2.2, can be explained by differences in the modelling of the jet at the inlet.

It has also been shown that details of the jet inlet have a strong impact on the overall flow. Small differences in jet velocity maxima can lead to a significant difference in jet penetration, as can a difference in velocity profile, such as a plug-shaped profile rather than Poiseuille. Similarly, a jet that is turbulent before entering the crossflow will behave differently to a jet that is laminar at the point where it enters the crossflow. Finally, the resolution of a simulation in the vicinity of the jet inlet can impact the flow, as an unresolved simulation cannot capture the same level of detail as that seen in a simulation on a refined grid.

Comparing results using the same parameters and sub-grid stress and flux model, but different large-scale numerical methods yielded much more similar results. Differences were seen in the vertical velocity profiles, leading to significant differences in the CVP trajectory, and slight differences in the concentration and centreline trajectories, however all spectra were very similar. The observed differences in dissipation and Kolmogorov length scale ratio are caused by the different levels of accuracy between second- and fourth-order finite difference schemes.

Overall, the numerical methods and sub-grid scale model combine to provide acceptable qualitative agreement to the results of experiments and other simulations.



# Chapter 4

## Parameter Investigation - Velocity ratio

In this chapter, the effect of varying the velocity ratio, while holding all other parameters constant, will be investigated. Two large-eddy simulations (LES) were performed at  $Re = 2 \times 10^4$ , with velocity ratios of  $V_{av}/U_{max} = 2.25$  and  $V_{av}/U_{max} = 3$  respectively, and one at  $Re = 2.05 \times 10^4$  with an average jet velocity of  $V_{av}/U_{max} = 0.405$  at the inlet. Trajectories, jet spreading, spectra and dissipation were compared for the three simulations.

| Name | Re                 | $V_{av}/U_{max}$ | $d$ |
|------|--------------------|------------------|-----|
| I    | $2.05 \times 10^4$ | 0.405            | 1   |
| II   | $2 \times 10^4$    | 2.25             | 1   |
| III  | $2 \times 10^4$    | 3                | 1   |

Table 4.1: Names and parameters for the three simulations discussed in this chapter.

### 4.1 Trajectories

Three types of time-averaged trajectories were calculated for low, middle and highest velocity simulations. These are used to investigate the effect of the average jet velocity on the shape and penetration of the jet.

Figure 4.1a shows the centreline trajectory, the streamline taken from the centre of the jet inlet, for each of the three velocity ratios. As the velocity ratio increases the trajectories show deeper penetration, being less readily deflected by the crossflow. The lowest velocity ratio simulation,  $V_{av}/U_{max} = 0.405$  is deflected until it is parallel to the crossflow free stream

near to the jet inlet, and remains close to parallel for the remainder of the length of the simulation domain. A slight downwards trend in the trajectory is visible close to the outlet, which is most likely caused by the advective outlet condition given in section 1.2.4. This simulation shows a maximum penetration of approximately one jet diameter. In contrast, neither of the two higher velocity ratio simulations reach the point where they are parallel with the lower wall within the simulation domain. Because of this we cannot ascertain and compare their maximum penetration, or even say definitely if a point of maximum penetration will exist. The separation between the  $V_{av}/U_{max} = 2.25$  and  $V_{av}/U_{max} = 3$  centreline trajectories at the outlet is approximately 1.8 jet diameters.

The concentration trajectories, calculated as the maxima of scalar concentration in the centreplane,  $z = 0$ , at each  $x$  position downstream of the jet inlet, for each of the three simulations are shown in Figure 4.1b. The concentration trajectory of the  $V_{av}/U_{max} = 0.405$  simulation initially has a similar shape to its centreline trajectory, however it begins to drop toward the lower wall of the domain, and from approximately 5 jet diameters downstream of the jet inlet the trajectory runs along the lower wall. This indicates that the maximum concentration of the scalar is along the lower wall of the domain, and that the jet streaks along the lower wall rather than separating from the wall into a plume. This is supported by Figures 4.2a and 4.2b, which show isosurfaces of scalar concentration for the  $V_{av}/U_{max} = 0.405$  and  $V_{av}/U_{max} = 3$  simulations, and display the difference between a low velocity ratio, wall-attached jet, and a higher velocity ratio jet which separates from the wall.

Both of the higher velocity ratio concentration trajectories follow much the same shape as their respective centreline trajectories, although they do not penetrate quite as deeply. This supports results that have been previously reported by Kamotani and Greber [21]. The separation between the  $V_{av}/U_{max} = 2.25$  and  $V_{av}/U_{max} = 3$  concentration trajectories at the outlet is approximately 2 jet diameters.

The separation between the centreline and concentration trajectories at the outlet for the  $V_{av}/U_{max} = 2.25$  and  $V_{av}/U_{max} = 3$  simulations are approximately 1 jet diameter and 0.8 jet diameters respectively. This indicates that the jet in the  $V_{av}/U_{max} = 3$  simulation is further from reaching its maximum penetration than the  $V_{av}/U_{max} = 2.25$  simulation, as the separation between the two types of trajectory increases until the point where the jet becomes parallel to the crossflow free stream.

The CVP trajectories, measured by the locus of maximum transverse velocity along the centreplane,  $z = 0$ , of the three simulations is shown in Figure 4.1c. All three CVP trajectories follow their respective centreline

trajectories close to the jet inlet, however their behaviour further from the inlet differs significantly. The drop in transverse position occurs much closer to the inlet in the  $V_{av}/U_{max} = 0.405$  simulation than either of the  $V_{av}/U_{max} = 2.25$  or  $V_{av}/U_{max} = 3$  simulations, indicating that the initial vertical velocity of the jet perseveres for longer at higher a higher average inlet velocity. The trajectory of the  $V_{av}/U_{max} = 3$  simulation after the drop is also higher than that of the  $V_{av}/U_{max} = 2.25$  simulation, which in turn is higher than that of the  $V_{av}/U_{max} = 0.405$  simulation, suggesting that the position of the CVP is related to the position of the centreline trajectory. However, apart from the difference in penetration, all three curves behave in a similar manner after the drop off, indicating that the CVP behaves in a similar manner, irrespective of the velocity ratio.

Overall, there is a close relationship between the penetration of the jet and the average velocity of the jet at the inlet. To quantify these relationships it would be necessary to run more simulations, holding the Reynolds number and boundary layer thickness constant while varying the velocity ratio more widely, both higher and lower than the values used here. Running simulations with the same parameters on a longer domain would also allow us to further investigate the long-term relationships between velocity ratio and penetration.

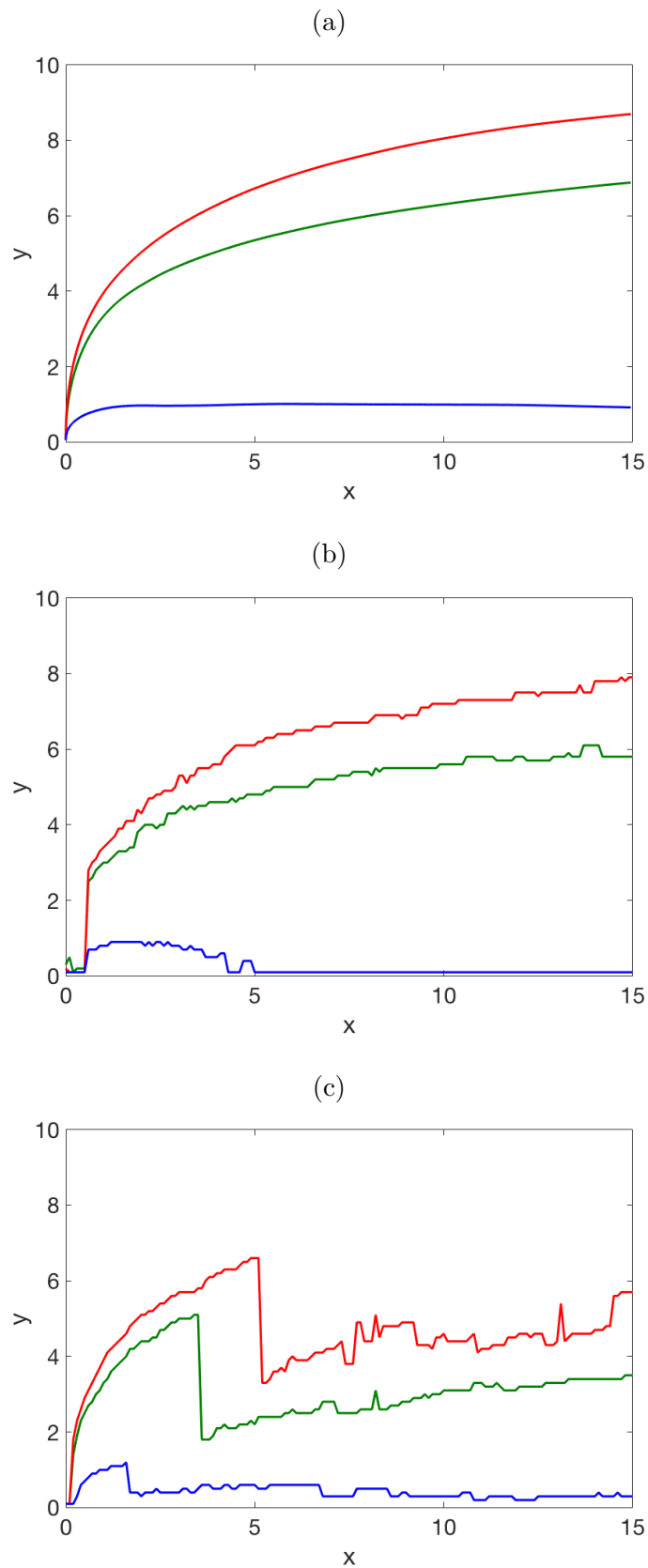


Figure 4.1: (a) Centreline, (b) concentration and (c) CVP trajectories of  $V_{av}/U_{max} = 0.405$  (blue),  $V_{av}/U_{max} = 2.25$  (green) and  $V_{av}/U_{max} = 3$  (red) simulations.

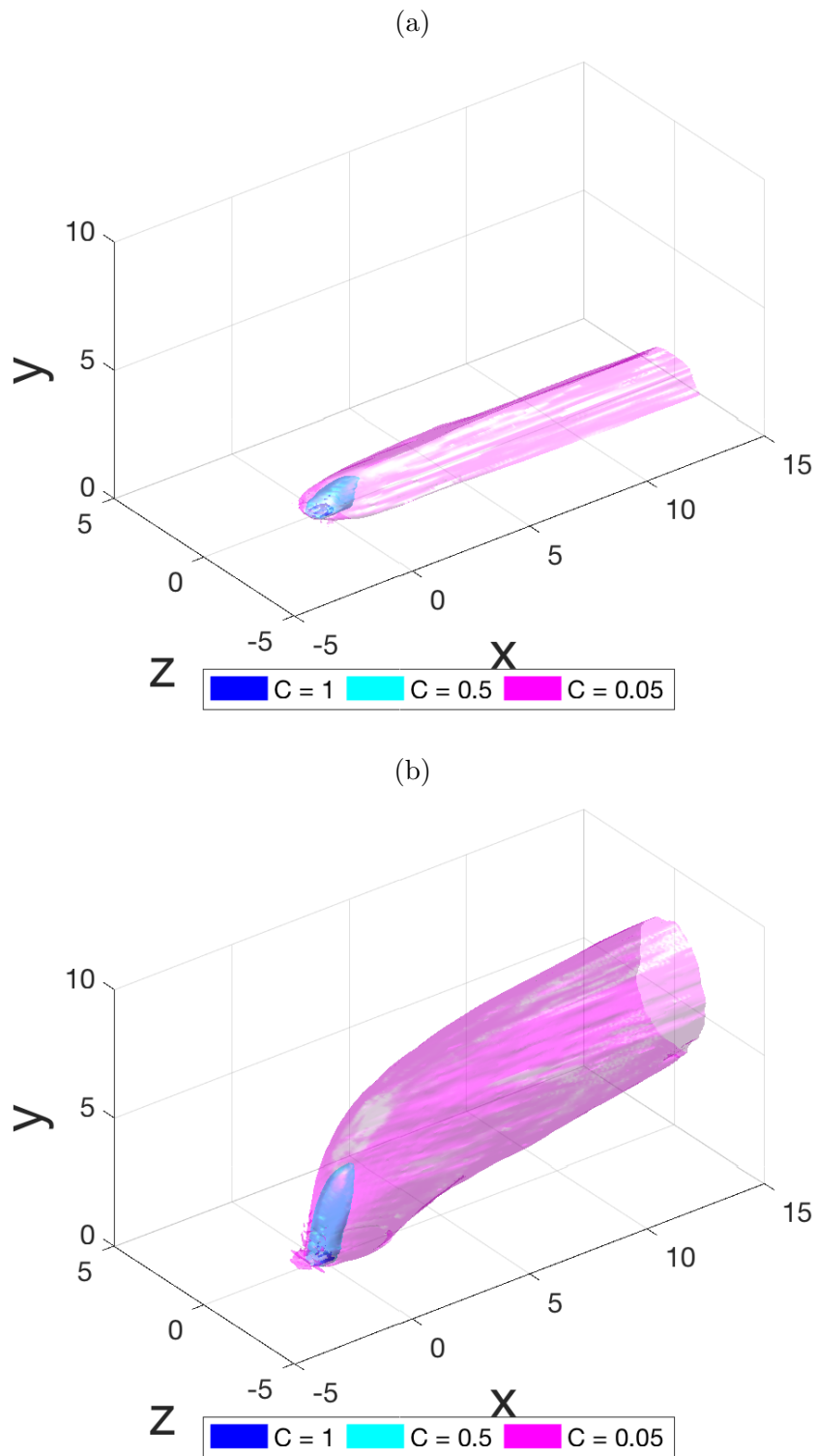


Figure 4.2: Isosurfaces of scalar concentration for simulations run at (a)  $V_{av}/U_{max} = 0.405$  and (b)  $V_{av}/U_{max} = 2.25$ .

## 4.2 Jet Spreading

Jet spreading is used to quantify the amount of entrainment of crossflow fluid that occurs. Both the horizontal and vertical spread of the jets in the three simulations were investigated from one jet diameter downstream of the centre of the jet inlet to the outlet. The width and height of an isosurface of scalar concentration, taken at  $c = 0.05$ , are used to determine the horizontal and vertical jet spread respectively.

The vertical spread of the jet, shown in Figure 4.3a, varies greatly between the smallest and two larger velocities investigated. The spread of the lowest velocity simulation does not achieve values much higher than one jet diameter, and remains fairly constant for the full length of the domain. With reference to the trajectory information given in Section 4.1, this spread is equivalent to the penetration of the jet above the lower wall to which the jet is attached. In the other two simulations the jet is not attached to the wall, and spread can occur both upwards and downwards. In these cases we see a much larger spread which reduces slightly with streamwise distance. It can be seen in Figure 4.4 that this occurs because the lower boundary of the isosurface used to measure the spreading rises more sharply than the upper boundary. The shape of the spread for the  $V_{av}/U_{max} = 2.25$  simulation and the  $V_{av}/U_{max} = 3$  simulation are also very similar, but the heights are different. This is not unexpected, as the velocity ratios are similar. Figure 4.4 also shows that the upper boundary of the jet plume touches the upper wall of the simulation domain near the outlet. As this limits the height of the jet spread in this region, the results beyond approximately  $x = 13$  are impacted by the wall for the  $V_{av}/U_{max} = 3$  simulation, and the spreading may be less than would be seen if the simulation were performed in a taller domain.

The side boundaries of the simulation domain were set to be far enough away from the jet that they would have only minimal effect on the horizontal spreading, particularly in the region close to the jet inlet. Figure 4.3b shows that the horizontal spread close to the jet inlet is quite similar for all three velocity ratios. In all three simulations, the horizontal spread of the jet is approximately 2.5 times the width of the jet inlet, indicating that much entrainment of crossflow fluid has occurred close to the inlet. Further downstream all three jets become wider as they entrain more fluid. Not surprisingly, the larger the velocity ratio, the larger the horizontal spread. The increase in width at the outlet between the two lower velocity ratio simulations is very similar to the equivalent increase between the two higher velocity ratio simulations. As the difference in velocity ratios between these two sets of cases are significantly different, it appears that the relationship between horizontal spread and velocity ratio is non-linear.

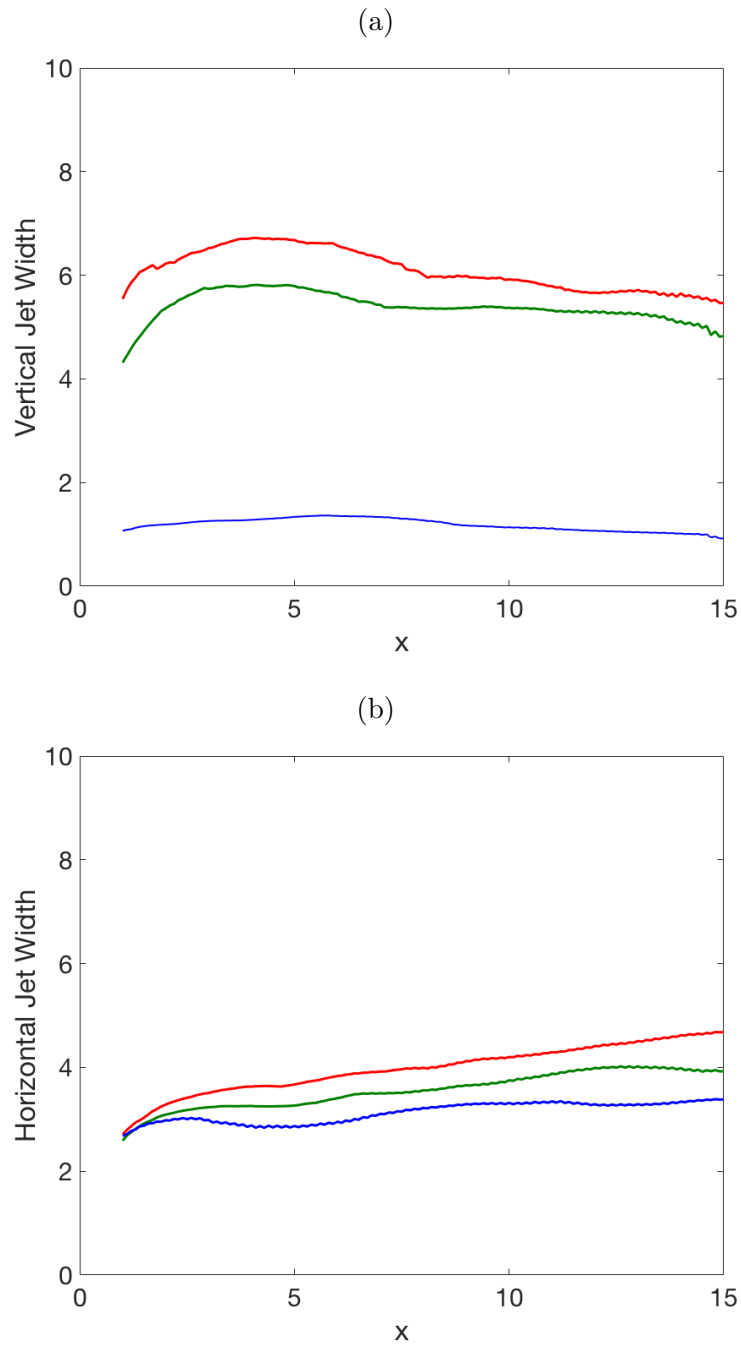


Figure 4.3: (a) Vertical and (b) horizontal spreading of the jet for  $V_{av}/U_{max} = 0.405$  (blue),  $V_{av}/U_{max} = 2.25$  (green) and  $V_{av}/U_{max} = 3$  (red) simulations.

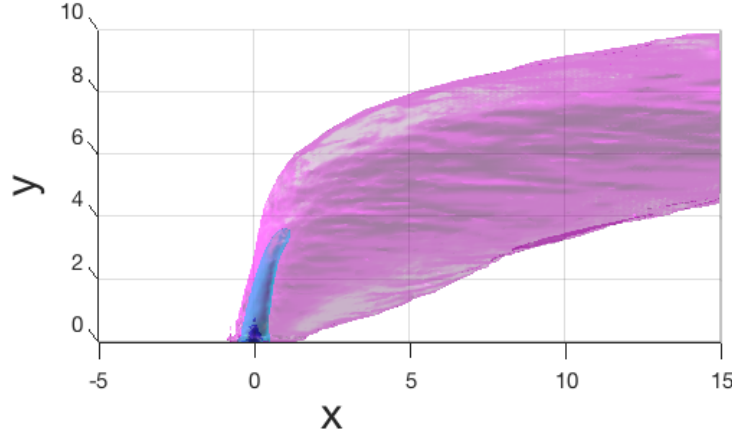


Figure 4.4: Isosurfaces of scalar concentration for  $V_{av}/U_{max} = 3$  simulation. Isosurface values are 1 (dark blue), 0.5 (cyan) and 0.05 (pink)

From these results we see that the jet with the largest velocity ratio entrains the largest amount of crossflow fluid and that with the lowest ratio entrains the least, as would be expected. However, in order to properly investigate the relationships between the jet inlet velocity and both the horizontal and vertical spread, many more simulations at different velocity ratios are needed.

### 4.3 Spectra

Time averaged spectra of turbulent kinetic energy and scalar concentration were calculated in the  $z$  direction for simulations run at the three velocity ratios at  $x = 7.7$ , as this point is far enough from the jet inlet for the turbulent flow to be developed, and far enough from the outlet to be unaffected by the outlet boundary conditions. The  $y$  coordinate for the spectra calculation was chosen to correspond to the centreline trajectory at this point. This gave positions of  $(x, y) = (7.7, 1.0)$ ,  $(x, y) = (7.7, 5.9)$  and  $(x, y) = (7.7, 7.6)$  for the  $V_{av}/U_{max} = 0.405$ ,  $V_{av}/U_{max} = 2.25$  and  $V_{av}/U_{max} = 3$  simulations respectively.

The turbulent kinetic energy spectra of all three simulations, Figure 4.5a, behave similarly, with the spectral density increasing with velocity ratio for all  $\kappa$ . This indicates that proportionally more energy is present at all wavelengths for higher velocity ratios. In all three simulations, turbulent kinetic energy spectra show a slope of approximately  $-5/3$  for wavenumbers above  $n = 6$ , equivalent to  $\kappa = 6\pi/5$ . A  $-5/3$  law is expected in the inertial range by the model, so this suggests that the sub-grid scale model is operating as



designed. A hook, the numerical artifact discussed in Section 3.3.3, is seen in the spectrum of the turbulent kinetic energy for the smallest velocity ratio,  $V_{av}/U_{max} = 0.405$ .

In Figure 4.5b, the spectra of scalar concentration show a higher spectral density for higher velocity ratios, especially for low values of  $\kappa$ . For higher values of  $\kappa$  there is little difference between the spectral density for the two larger velocity ratio simulations, and close to  $\kappa = 50$  all three simulations show similar scalar spectral densities. This suggests that the velocity ratio has less impact on the spectral density of the scalar than it does on the spectral density of the turbulent kinetic energy. Hooks are present at the high wavenumber end of all three scalar spectra, although the hook is largest in the  $V_{av}/U_{max} = 0.405$  simulation and decreases in size with increase in velocity ratio. The scalar spectra shows a  $-\frac{5}{3}$  slope for wavenumbers of  $\kappa \approx 2$  through  $\kappa \approx 20$ . For wavenumbers higher than 20, the slope becomes more negative. Pullin [44] notes that the sub-grid flux model is over-dissipative in the higher wavenumber range, and this more negative slope reflects this.

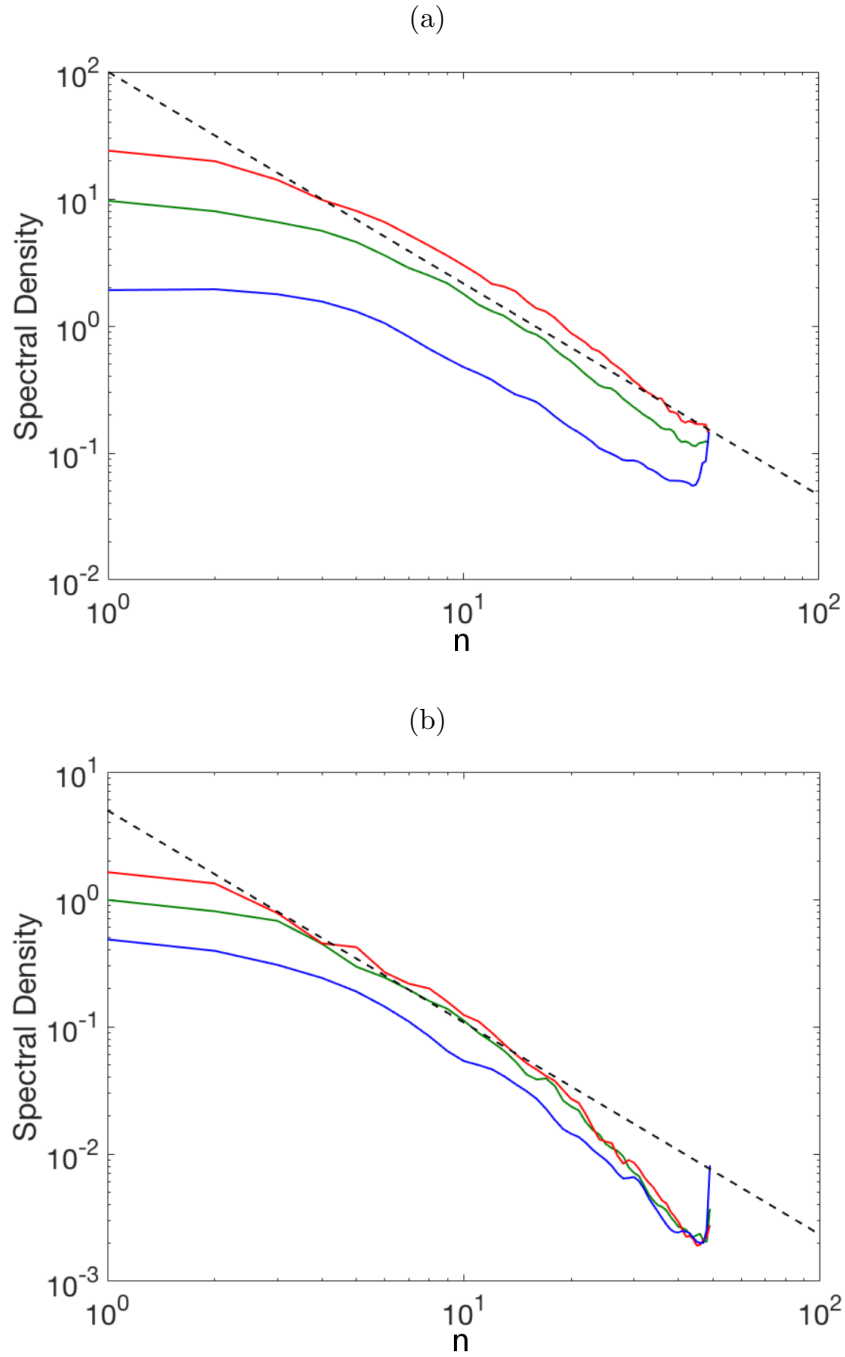


Figure 4.5: Spectra of velocity components (a) kinetic energy, and (b) scalar concentration for  $V_{av}/U_{max} = 0.405$  (blue),  $V_{av}/U_{max} = 2.25$  (green) and  $V_{av}/U_{max} = 3$  (red) simulations, with optimal [37]  $-\frac{5}{3}$  slope marked (dashed line).

## 4.4 Dissipation and Kolmogorov length scale

For each simulation, the dissipation ratio,  $\varepsilon^{SGS}/\varepsilon^{LS}$ , and Kolmogorov length scale ratio,  $\eta/\Delta x$ , were calculated using the methods given in Section 2.6.5 for each position on the jet centreplane,  $z = 0$ . Contours of  $\log(\varepsilon^{SGS}/\varepsilon^{LS})$  and  $\eta/\Delta x$  were plotted within the jet plume, defined as regions where the scalar concentration  $c \geq 0.05$ .

Figure 4.6 shows contours of  $\log(\varepsilon^{SGS}/\varepsilon^{LS})$ . The black contour indicates the points where  $\log(\varepsilon^{SGS}/\varepsilon^{LS}) = 0$  which is where the sub-grid and large-scale dissipation is equal, separating the regions where the large-scale and sub-grid dissipation dominate. Close to the jet inlet  $\varepsilon_{SGS}/\varepsilon_{LS}$  is much greater than one in all three simulations, however downstream of  $x = 5$  the ratio is less than one almost everywhere in both the  $V_{av}/U_{max} = 2.25$  and  $V_{av}/U_{max} = 3$  simulations. The  $\varepsilon_{SGS}/\varepsilon_{LS} \geq 1$  region persists for longer in the  $V_{av}/U_{max} = 0.405$  simulation, however it too does not last the full length of the domain. In all three simulations the ratio becomes steadily smaller as  $x$  increases. This shows that the turbulence model is active close to the jet inlet, but much less active downstream.

Figure 4.7 shows contours of the Kolmogorov length scale ratio,  $\eta/\Delta x$ . At all points within the jet plume the ratio is less than one, indicating that the smallest turbulent eddies are smaller than the grid size. This in turn indicates that the use of LES is justified. Close to the jet inlet the Kolmogorov length,  $\eta$ , is much smaller than the grid size,  $\Delta x$ , with a ratio of less than 0.1 in all three simulations. In the  $V_{av}/U_{max} = 0.405$  simulation the ratio does not take values larger than 0.2, indicating that the eddies remain small throughout the domain. In the  $V_{av}/U_{max} = 2.25$  and  $V_{av}/U_{max} = 3$  simulations the ratio increases steadily in the streamwise direction, increasing to a maximum of approximately 0.6, indicating that larger velocity ratio jets in crossflow produce produce larger eddies downstream.

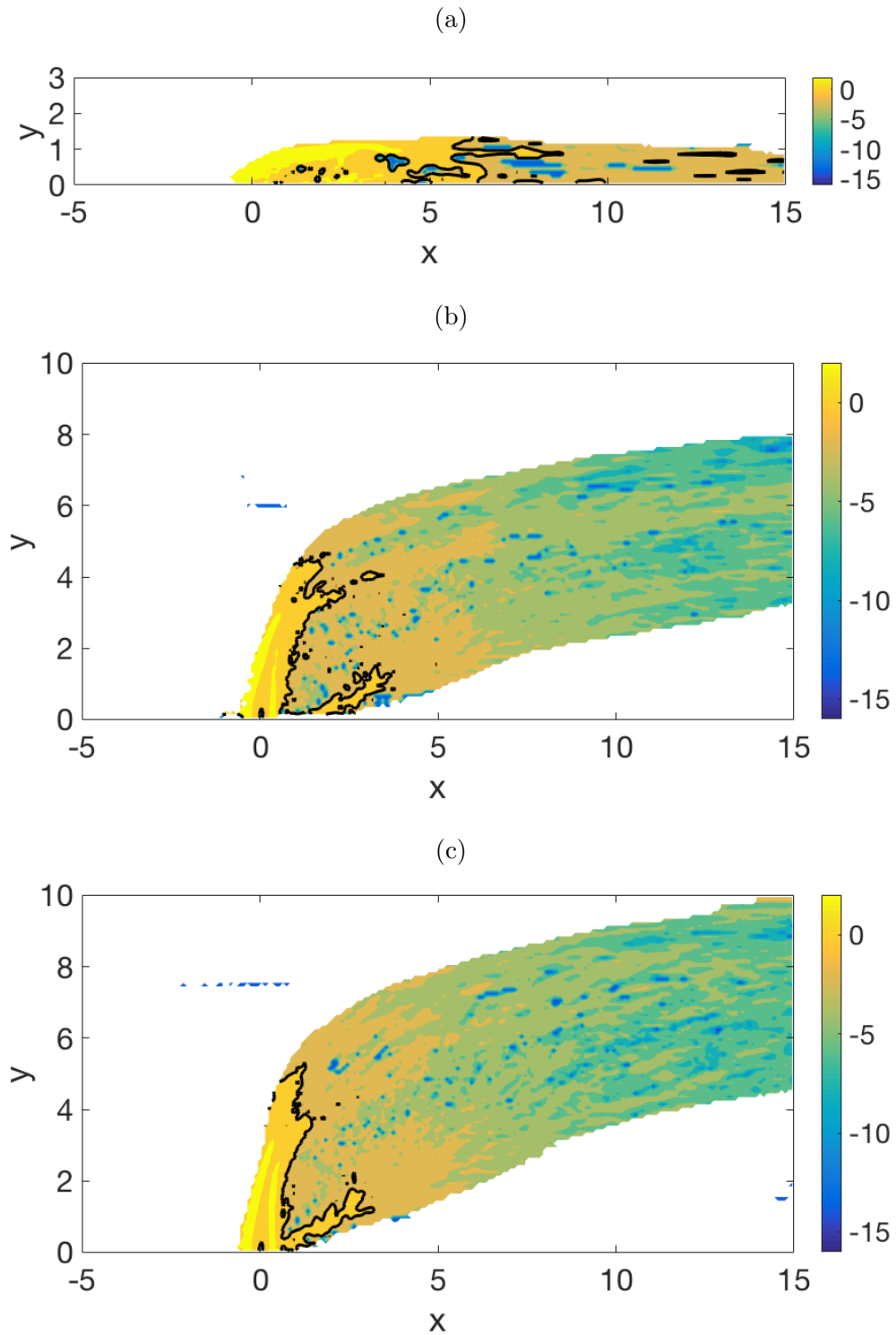


Figure 4.6: Logarithm of point-wise dissipation ratio on plane  $z = 0$  for regions where scalar concentration  $c \geq 0.05$  for simulations run at (a)  $V_{av}/U_{max} = 0.405$ , (b)  $V_{av}/U_{max} = 2.25$  and (c)  $V_{av}/U_{max} = 3$ . Black line shows contour where  $\log(\varepsilon_{SGS}/\varepsilon_{LS}) = 0$ .

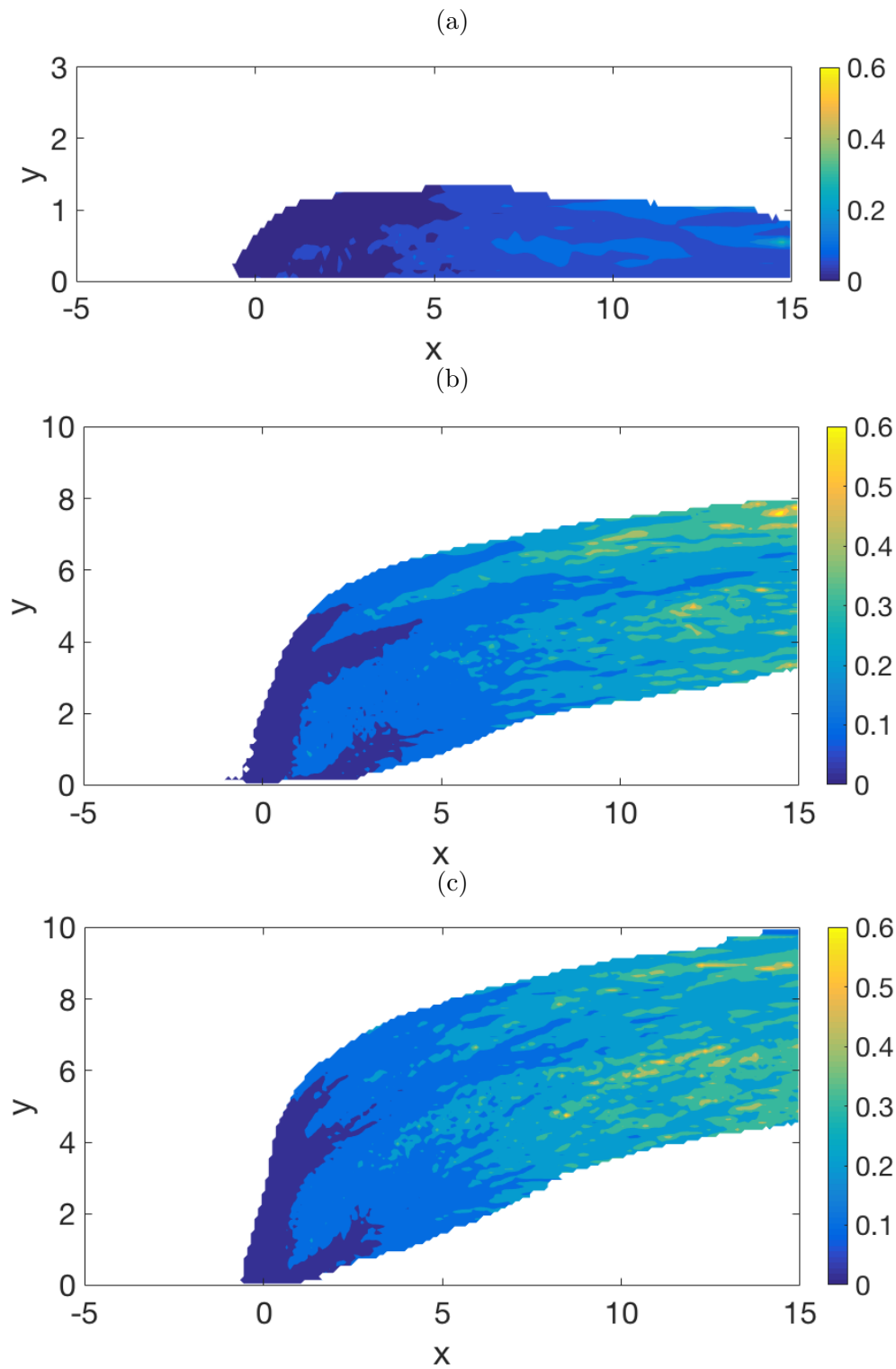


Figure 4.7: Point-wise Kolmogorov length scale ratio on plane  $z = 0$  for regions where scalar concentration  $c \geq 0.05$  for simulations run at (a)  $V_{av}/U_{max} = 0.405$ , (b)  $V_{av}/U_{max} = 2.25$  and (c)  $V_{av}/U_{max} = 3$ .

## 4.5 Conclusion

It has been shown in this chapter that there is a relationship between the velocity ratio at the jet inlet and the penetration and spread of the jet, as well as the amount of kinetic and scalar energy in the system and the dissipation of that energy. A higher jet velocity leads to a deeper penetrating jet that spreads further, and contains and dissipates more energy at all length scales.

In order to properly quantify the relationships between the average jet velocity at the inlet and all of these flow characteristics, it is necessary to run more simulations. Time and computational constraints limited the number of simulations that could be run. Of particular interest are simulations run at  $V_{av}/U_{max} = 1$ , to see the effect of equal jet and crossflow velocities, and at higher velocity ratios than  $V_{av}/U_{max} = 3$ , to continue to track the changes in flow characteristics. Simulating higher velocity ratio flows would require increasing the height of the simulation domain, to avoid contact of the jet plume with the upper wall. For the investigation of trajectories it would also be beneficial to extend the length of the domain to allow the jets to reach their maximum penetration. These increases in the size of the simulation domain could be achieved in two ways. The first would keep the same grid size, retaining the current resolution but increasing the number of grid points. This would lead to much longer simulation times using the current code. The other method would keep the number of grid points constant, but increase the grid size, reducing the resolution of the results. The first of these would not be feasible for my implementation in terms of both time and computational resources, and the second might not provide reliable results.

# Chapter 5

## Comparison of large-eddy simulation and direct numerical simulation

In Chapter 3, some large-eddy simulations (LES) were performed at Reynolds numbers that were lower than  $Re = 1 \times 10^4$ , the Reynolds number at which a change from laminar to turbulent flow is observed [15]. At these low Reynolds numbers, we expect that the sub-grid scale stress and flux models would not have a large impact on the results of the simulation, and thus that the results of an LES and a direct numerical simulation (DNS) would be very similar. At moderate Reynolds numbers, above  $Re = 1 \times 10^4$ , we would expect to see a much greater difference between the LES and DNS.

Comparing the velocity and scalar concentration profiles, trajectories and spectra of LES with their respective DNS equivalents, both performed on the same grid, we show the impact that the addition of the sub-grid scale stress and flux models have on the overall flow at different Reynolds numbers.

| Name | Simulation | Re    | $V_{av}/U_{max}$ | $d$  |
|------|------------|-------|------------------|------|
| I    | LES        | 640   | 3.05             | 2.06 |
| II   | DNS        | 640   | 3.05             | 2.06 |
| III  | LES        | 13640 | 2.2              | 0.28 |
| IV   | DNS        | 13640 | 2.2              | 0.28 |

Table 5.1: Names, simulation types and parameters of the four simulations discussed in this chapter.

In this chapter we consider both low and moderate Reynolds number simulations, with parameters as designated in Table 5.1.

## 5.1 Velocity and scalar profiles

Vertical profiles of the three components of velocity and the scalar concentration were plotted on the centreplane through the jet,  $z = 0$ , at positions both up and downstream of the jet inlet. The profiles for LES and DNS simulations were compared to determine the effect of the sub-grid scale stress and flux models on the components of velocity and the scalar concentration. Figures 5.1 - 5.3 show profiles of  $u$ ,  $v$ , and  $c$  respectively for the low Reynolds number case, while Figures 5.4 - 5.6 show the same profiles for the high Reynolds number case. Profiles of the cross-stream velocity,  $w$  are not given as the velocity fluctuations in this direction were minor.

The low Reynolds number LES and DNS simulations, Figures 5.1 and 5.2, give velocity profiles that are close to identical near to the jet inlet, and that differ only slightly further downstream. The streamwise and transverse velocity comparisons each show that both the LES and DNS have peaks at the same depth, but that the LES peaks are narrower and have a higher maximum value. This difference becomes more pronounced further downstream. The scalar concentration profiles in Figure 5.3 also show good agreement, with slightly narrower peaks in the LES. The narrower peaks seen in the LES are unexpected, as the sub-grid model normally smooths out the velocity and scalar gradients, rather than making them more pronounced.

The higher Reynolds number LES and DNS simulations, Figures 5.4 - 5.6, show differences between the LES and DNS that are more pronounced and begin closer to the jet inlet than those that are seen in the low Reynolds number case. The jet penetrates more deeply in the LES than the DNS, with maximum streamwise and transverse velocity occurring further from the lower wall. A higher maximum velocity is seen in both the streamwise and transverse velocity profiles. A higher maximum scalar concentration can also be seen in the LES, although this difference is less pronounced. The velocity and scalar profiles of the LES are smoother than those of the DNS, as would be expected.

Overall it can be seen that a higher Reynolds number leads to greater differences between the LES and DNS results. The main difference between the two methods of simulation is the penetration of the jet, although a difference in the shapes of the velocity and scalar concentration profiles can also be seen.



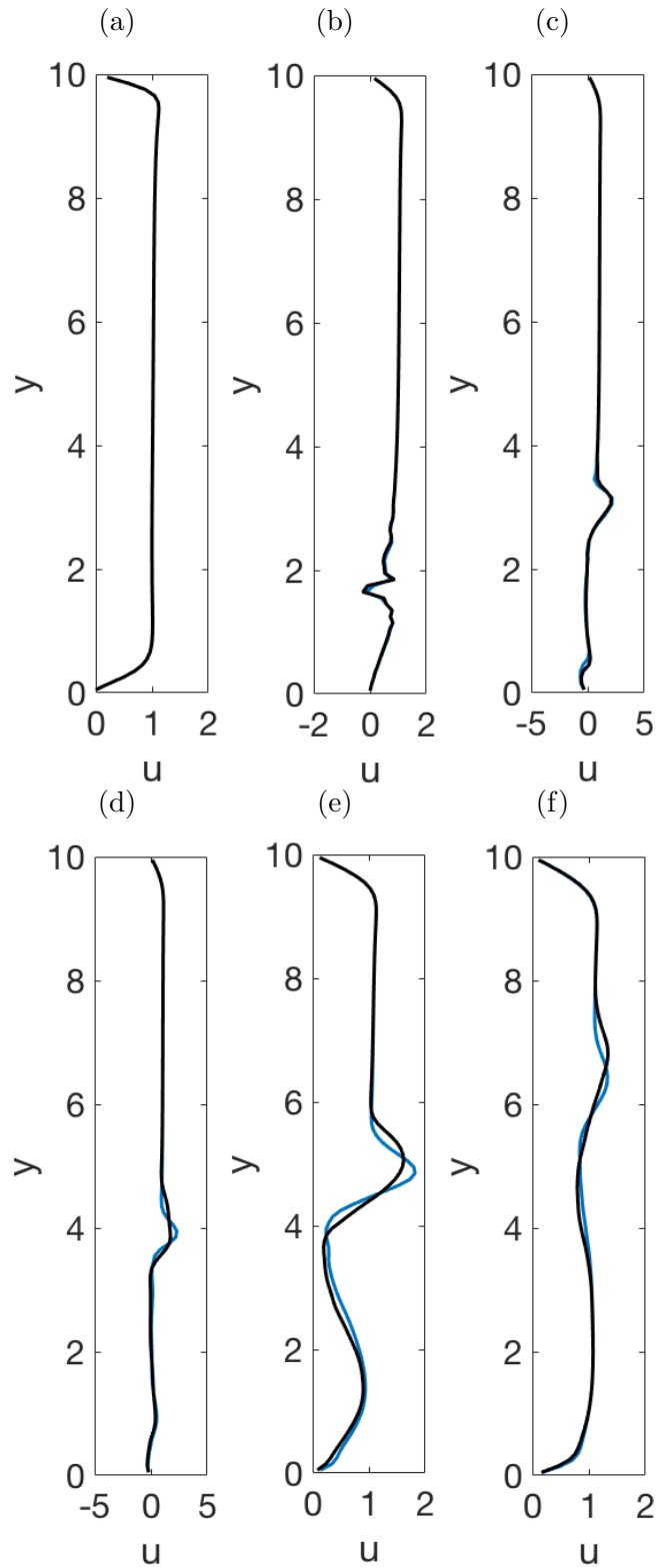


Figure 5.1: Profiles of  $u$  for LES (blue) and DNS (black), for  $\text{Re} = 640$  and  $V_{av}/U_{max} = 3.05$ , at (a)  $x = -2$ , (b)  $x = 0$ , (c)  $x = 1$ , (d)  $x = 2$ , (e)  $x = 4$ , and (f)  $x = 10$ . Note that the horizontal range changes between profiles.

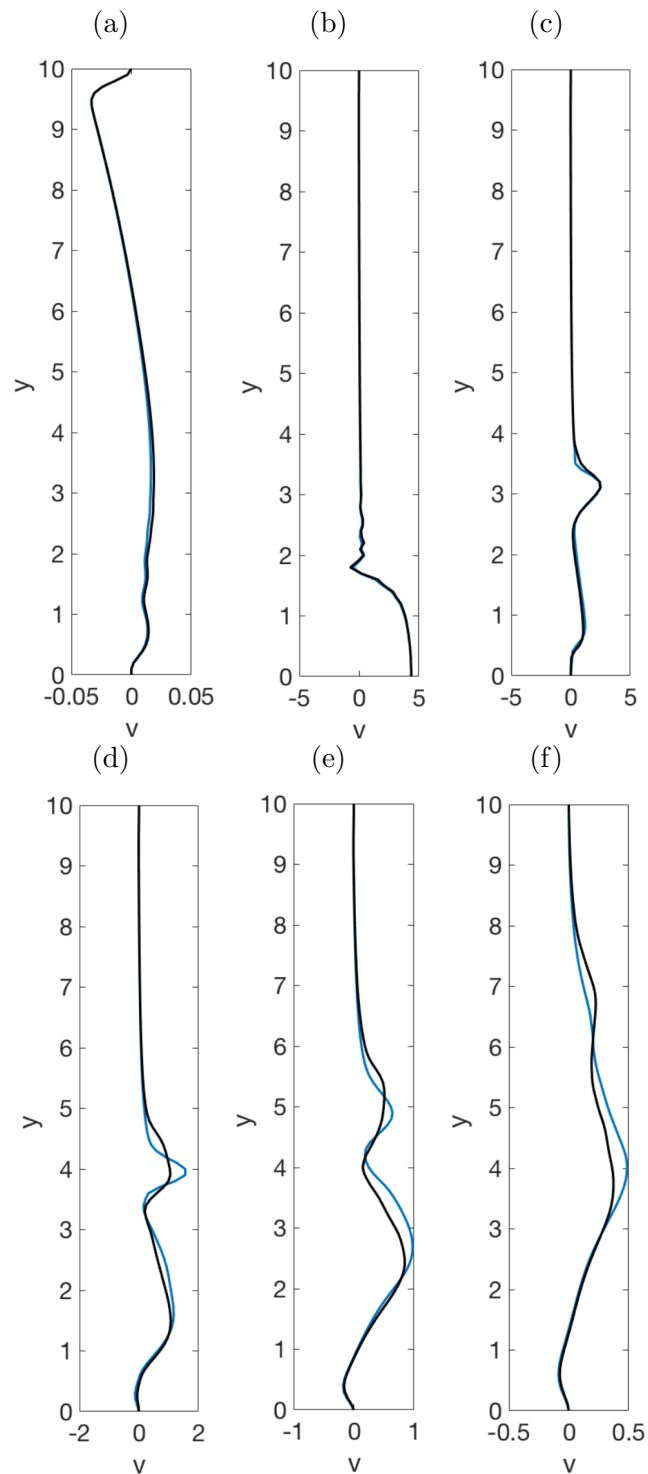


Figure 5.2: Profiles of  $v$  for LES (blue) and DNS (black), for  $\text{Re} = 640$  and  $V_{av}/U_{max} = 3.05$ , at (a)  $x = -2$ , (b)  $x = 0$ , (c)  $x = 1$ , (d)  $x = 2$ , (e)  $x = 4$ , and (f)  $x = 10$ . Note that the horizontal range changes between profiles.

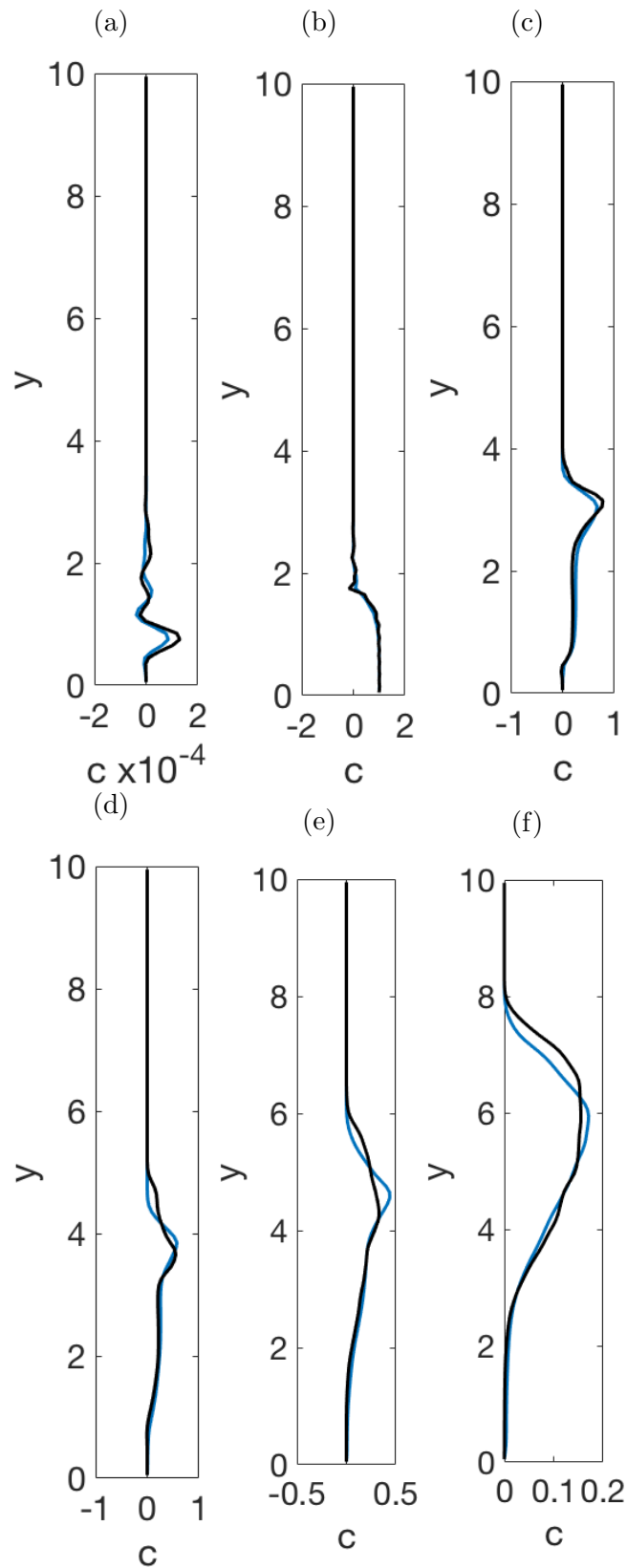


Figure 5.3: Profiles of  $c$  for LES (blue) and DNS (black), for  $\text{Re} = 640$  and  $V_{av}/U_{max} = 3.05$ , at (a)  $x = -2$ , (b)  $x = 0$ , (c)  $x = 1$ , (d)  $x = 2$ , (e)  $x = 4$ , and (f)  $x = 10$ . Note that the horizontal range changes between profiles.

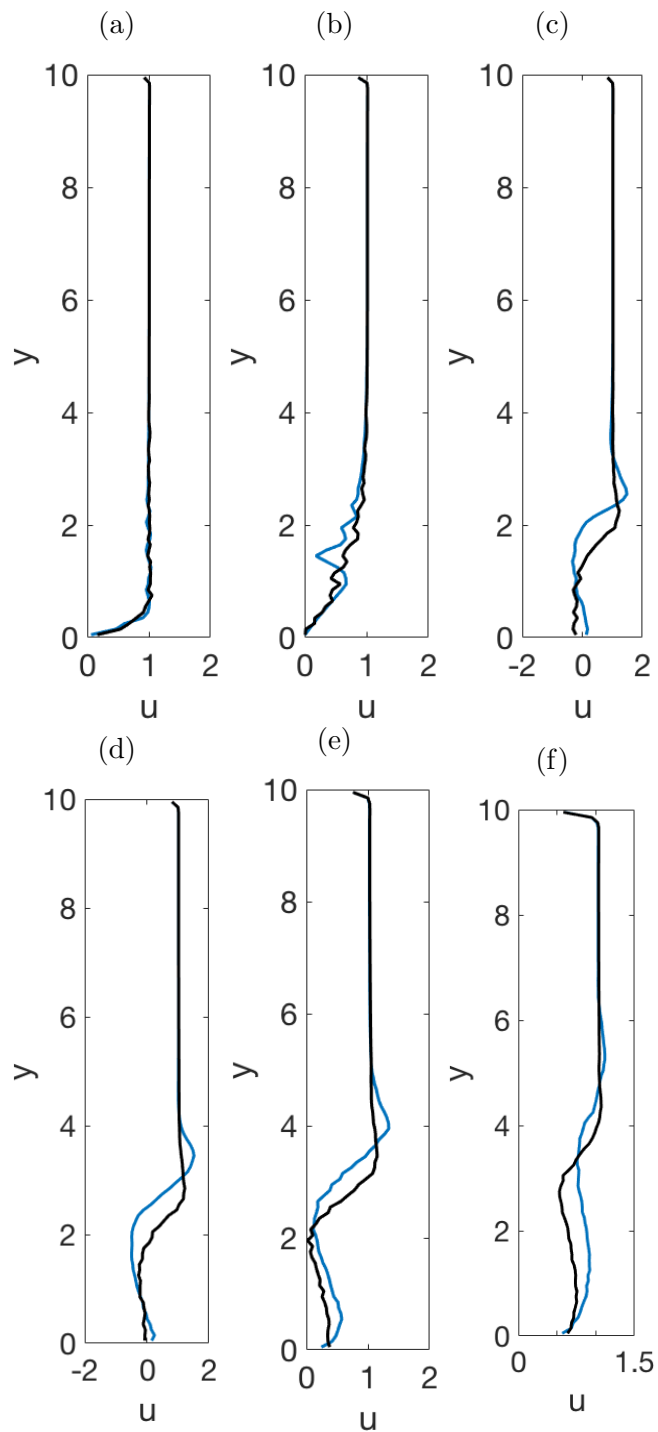


Figure 5.4: Profiles of  $u$  for LES (blue) and DNS (black) for  $Re = 13640$  and  $V_{av}/U_{max} = 2.2$ , at (a)  $x = -2$ , (b)  $x = 0$ , (c)  $x = 1$ , (d)  $x = 2$ , (e)  $x = 4$ , and (f)  $x = 10$ . Note that the horizontal range changes between profiles.

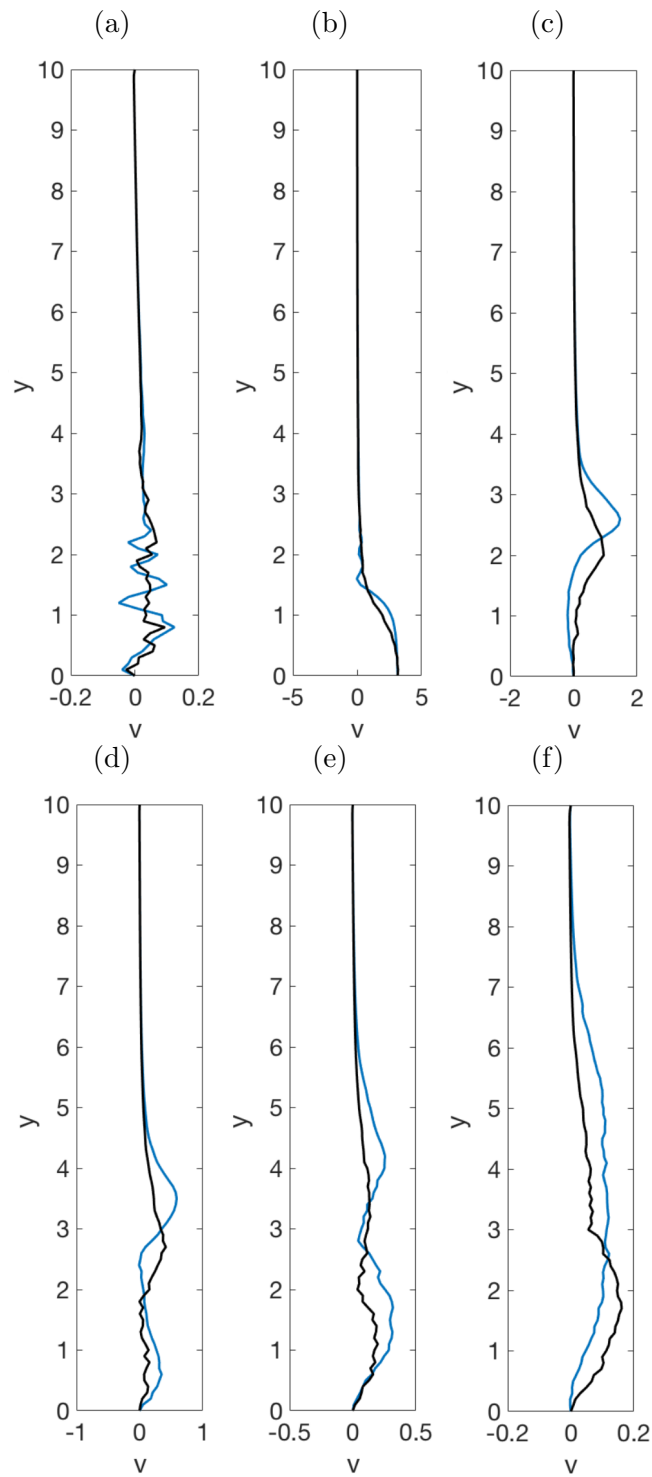


Figure 5.5: Profiles of  $v$  for LES (blue) and DNS (black) for  $Re = 13640$  and  $V_{av}/U_{max} = 2.2$ , at (a)  $x = -2$ , (b)  $x = 0$ , (c)  $x = 1$ , (d)  $x = 2$ , (e)  $x = 4$ , and (f)  $x = 10$ . Note that the horizontal range changes between profiles.

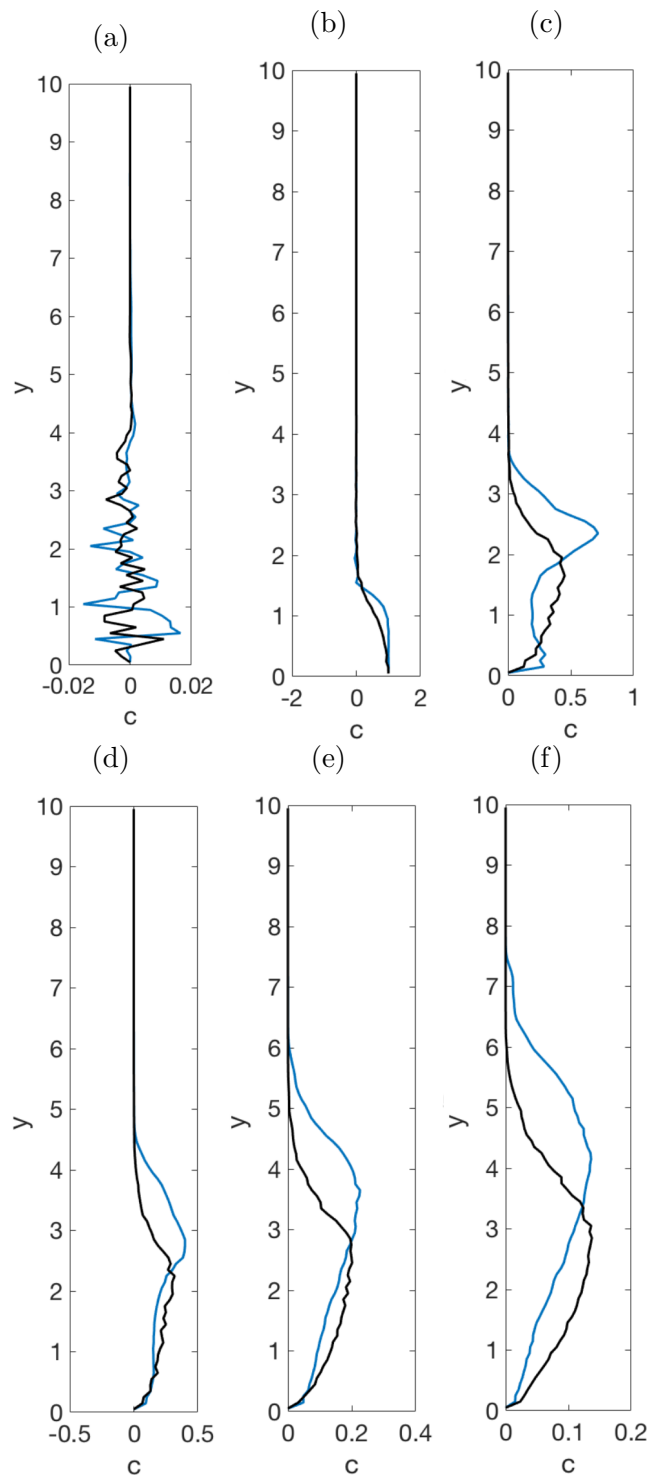


Figure 5.6: Profiles of  $c$  for LES (blue) and DNS (black) for  $Re = 13640$  and  $V_{av}/U_{max} = 2.2$ , at (a)  $x = -2$ , (b)  $x = 0$ , (c)  $x = 1$ , (d)  $x = 2$ , (e)  $x = 4$ , and (f)  $x = 10$ . Note that the horizontal range changes between profiles.

## 5.2 Trajectories

Centreline, concentration and CVP trajectories were calculated for both sets of simulations (Figures 5.7 and 5.8). From these trajectories we examine the effect of the sub-grid scale model on the penetration of the jet and the transport of the scalar.

Figure 5.7 shows that, at low Reynolds number, the difference between LES and DNS trajectories is very small, for all three trajectory types. The LES leads to slightly deeper jet penetration in the central region of the domain, shown in Figure 5.7a, however by the end of the domain the trajectories of the two simulations match very closely. The initial CVP trajectory, which is tracked by the maximum vertical velocity in the plane  $z = 0$ , before the drop off, is slightly longer in the LES case, suggesting that either the initial vertical velocity is maintained for slightly longer in the LES, or that the CVP is stronger close to the jet inlet in the DNS.

At higher Reynolds number, the difference in jet penetration depth is much more pronounced, as shown in Figure 5.8. This suggests that the initial vertical velocity of the jet is maintained for longer before being deflected by the crossflow in the LES case. The concentration trajectory in Figure 5.8b shows similar results to the centreline trajectory, with the line of maximum concentration occurring further from the lower wall for the LES simulation. In Figure 5.8c the drop off from the initial maximum vertical velocity occurs at almost the same streamwise position, despite the difference in depth. This suggests that the CVP is large enough to develop equally with and without the sub-grid stress model in this case.

Overall, these results support what was shown in section 5.1. The impact of the sub-grid scale stress and flux models increases with Reynolds number. This is as expected, as the model assumes that the large scale stresses dominate in the low Reynolds number limit, and scales its effects accordingly [37, 45]. This increase in effect at higher Reynolds number is seen as a significant difference in jet penetration between the high Reynolds number LES and DNS.

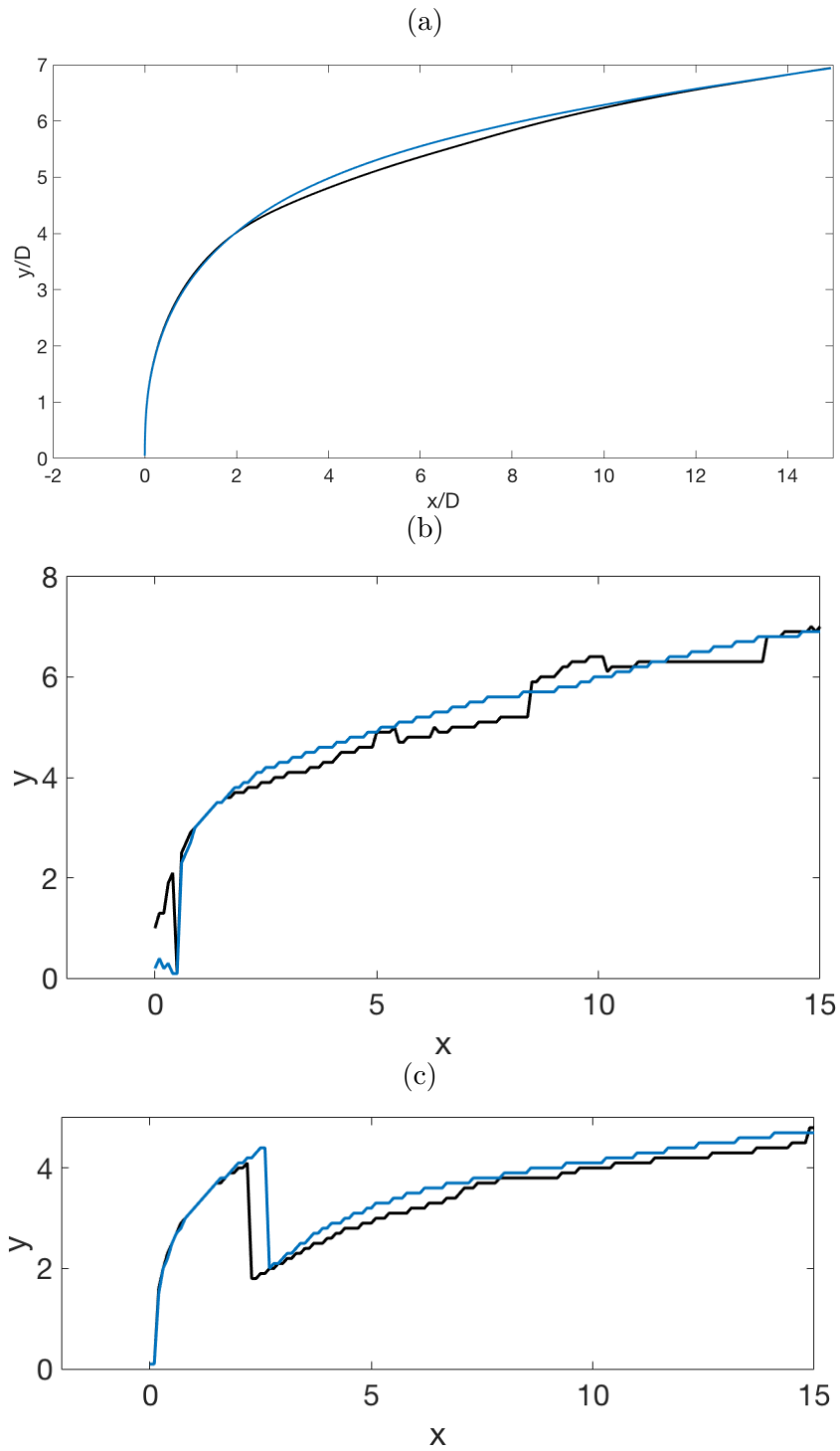


Figure 5.7: Comparison of (a) centreline, (b) concentration and (c) CVP trajectories of LES (blue) and DNS (black) simulations for  $Re = 640$  and  $V_{av}/U_{max} = 3.05$ .



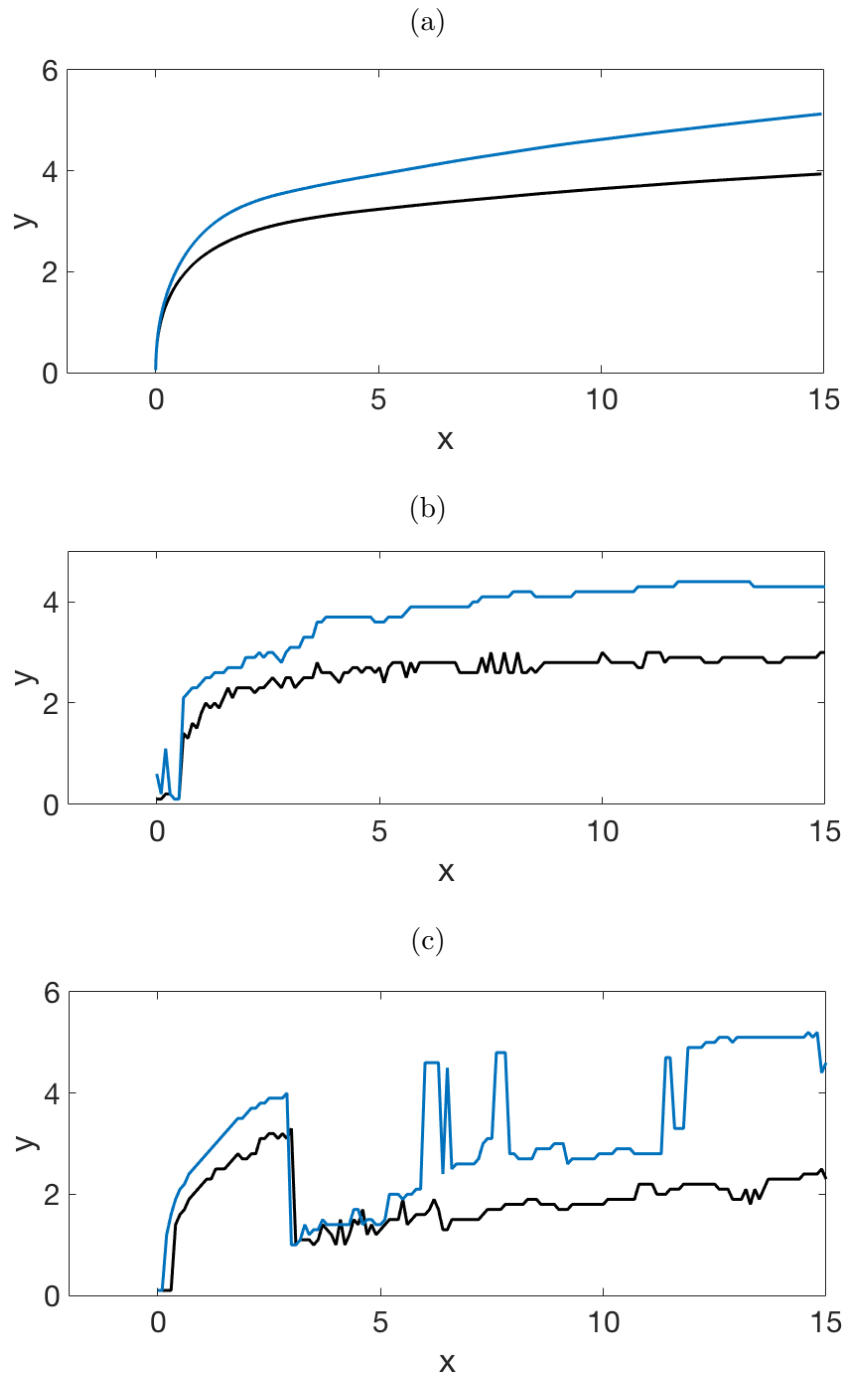


Figure 5.8: Comparison of (a) centreline, (b) concentration and (c) CVP trajectories of LES (blue) and DNS (black) simulations for  $Re = 13640$  and  $V_{av}/U_{max} = 2.2$ .

### 5.3 Spectra

Time averaged spectra of turbulent kinetic energy and scalar concentration were calculated in the  $z$  direction for each pair of simulations. Spectra for each flow were calculated at  $x = 7.7$ , as this point is far enough from the jet inlet for the turbulent flow to be developed, and far enough from the outlet to be unaffected by the outlet boundary conditions, and the  $y$  value was chosen to correspond to the centreline trajectory at this point. For the  $Re = 640$  simulations, this gave positions of  $(x, y) = (7.7, 5.9)$  and  $(x, y) = (7.7, 5.8)$  for the LES and DNS respectively. At  $Re = 13640$ , the positions were  $(x, y) = (7.7, 4.3)$  and  $(x, y) = (7.7, 3.5)$  for the LES and DNS respectively. These allow us to see the quantity and distribution of energy that is present at all wavelengths of the large flow scales.

At low Reynolds number, in Figure 5.9, the difference between simulations for both the turbulent kinetic energy and scalar concentration spectra is slight, in both shape and magnitude. The differences between the spectra increase with  $\kappa$ , indicating that the LES is damping the energy in the higher wavenumbers, as would be expected. The differences are more pronounced in the scalar concentration spectra than in the turbulent kinetic energy spectra, which reflects the overdamping effect of the sub-grid-flux model [44]. The high level of similarity between the two sets of spectra imply that at low Reynolds number the sub-grid-scale models had little impact on the flow. Neither of the low Reynolds number spectra show the  $-5/3$  slope at the high wavenumber end of the spectra that would be expected from a fully-functioning LES. The sub-grid scale model works on the assumption that the flow has an inertial subrange, which is not present in a low Reynolds number flow, so the lack of a  $-5/3$  slope indicates that the model is correctly switching off at low Reynolds numbers.

At higher Reynolds number the differences between the LES and the DNS are more pronounced, as can be seen in Figure 5.10. Significant differences can be seen in both the magnitude and the shape of the spectra. The shape of the high Reynolds number LES spectra are closer to the  $-\frac{5}{3}$  slope which is assumed by the sub-grid stress and flux model. The high Reynolds number LES shows more energy at low wavenumbers, and less energy at the highest wavenumbers, than its corresponding DNS. This means that, in the LES, more energy is present in the large motions within the flow, and more of the energy from the small-scale motions is being dissipated from the system by being transferred from the large scales to the sub-grid scales. The increased impact of the large-scale motions in the LES reflect the larger velocity peaks seen in the velocity profiles and the deeper penetration of the jet seen in the trajectories.

The scalar concentration spectra of both the high Reynolds number LES and DNS show a hook at the high wavenumber end. The causes of these hooks are discussed in section 3.3.3. As hooks are present in both the LES and DNS scalar spectra, it is apparent that the sub-grid flux model alone is not the cause of the hooks in this case.

Overall, these spectra confirm what has been shown in the previous two sections; as the Reynolds number increases the impact of the sub-grid scale model increases.

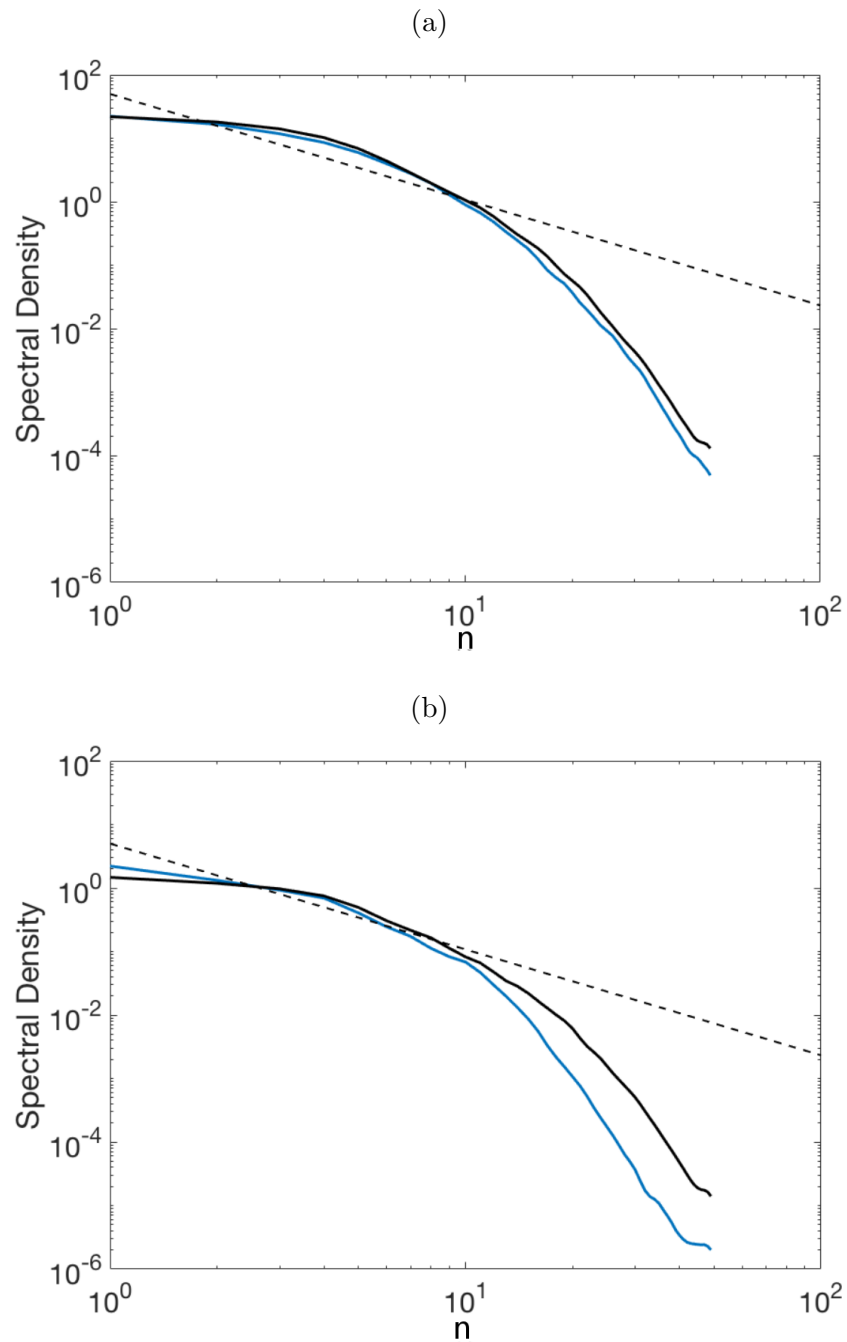


Figure 5.9: Spectra of components of velocity (a) kinetic energy, and (b) scalar concentration of LES (blue) and DNS (black) simulations for  $Re = 640$  and  $V_{av}/U_{max} = 3.05$ .

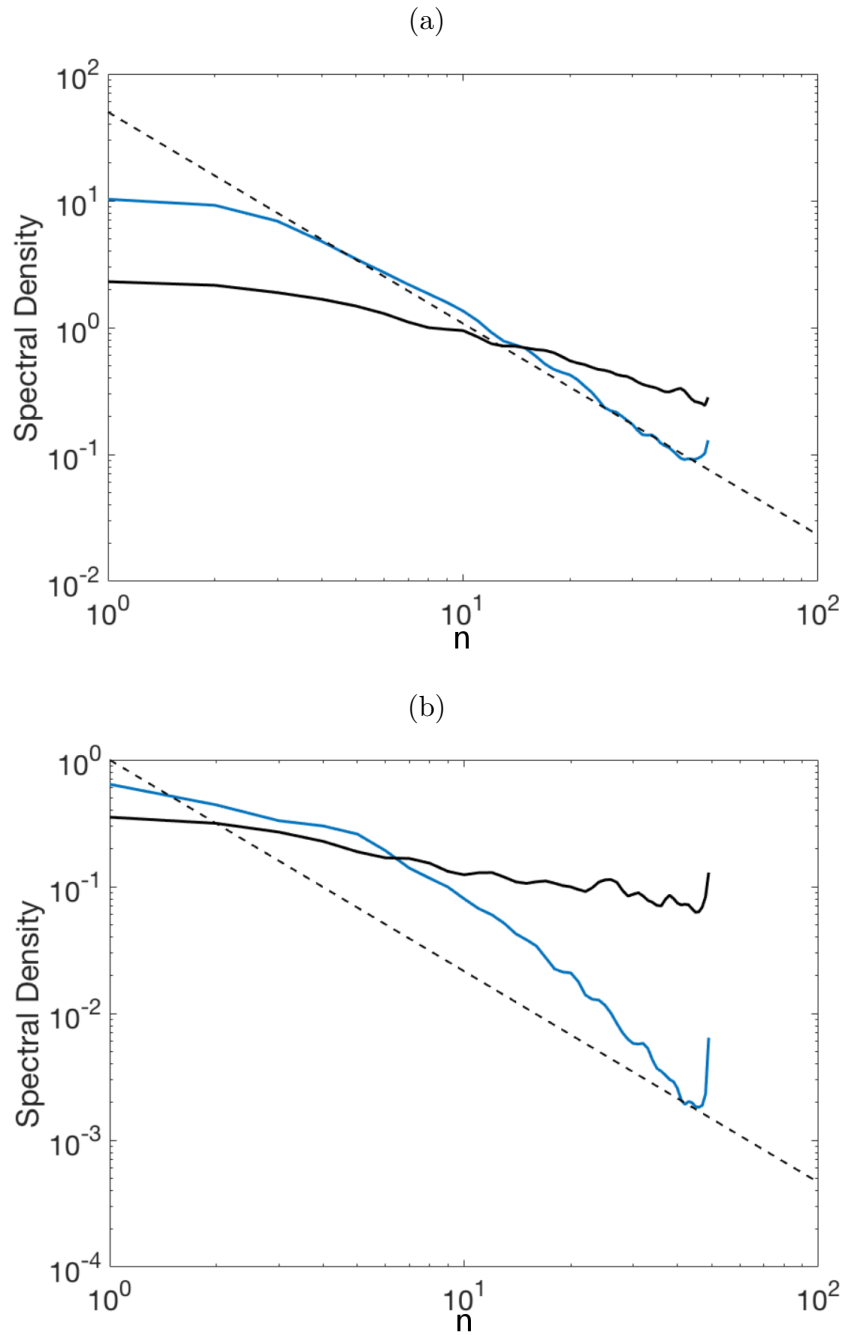


Figure 5.10: Spectra of components of velocity (a) kinetic energy, and (b) scalar concentration of LES (blue) and DNS (black) simulations for  $Re = 13640$  and  $V_{av}/U_{max} = 2.2$ .

## 5.4 Kolmogorov length scale ratio

For each pair of simulations the Kolmogorov length scale ratio,  $\eta/\Delta x$ , was calculated using the methods given in Section 2.6.5 for each position on the jet centreplane,  $z = 0$ . In the DNS, the large-scale dissipation alone was used as the total dissipation, while in the LES, total dissipation was calculated as the sum of the large and sub-grid scale dissipations. Contours of  $\eta/\Delta x$  were plotted within the jet plume, defined as regions where the scalar concentration  $c \geq 0.05$ . In regions where  $\eta/\Delta x > 1$ , the smallest eddies are larger than the grid size, and the flow is resolved. If  $\eta/\Delta x < 1$  the simulation is not resolved on the computational grid.

In the low Reynolds number simulations, shown in Figure 5.11, both the LES and the DNS show regions where  $\eta/\Delta x > 1$  away from the jet inlet, indicating that the flow is resolved in this area. However, close to the jet inlet the ratio is less than one in both simulations, indicating that this portion of the flow is unresolved. From these results it can be seen that the flow cannot be fully resolved on the computational grid, which is essential for a proper DNS. From previous results in this chapter, the impact of adding a sub-grid scale model to this simulation is minimal, so it would be necessary to refine the grid close to the jet inlet to achieve a more accurate simulation.

At higher Reynolds numbers  $\eta/\Delta x < 1$  for all points in the centreplane, and for both the LES and the DNS, as shown in Figure 5.12. This indicates that the flow is nowhere resolved at this Reynolds number, and thus performing the simulation using a sub-grid scale model is necessary on this computational grid.

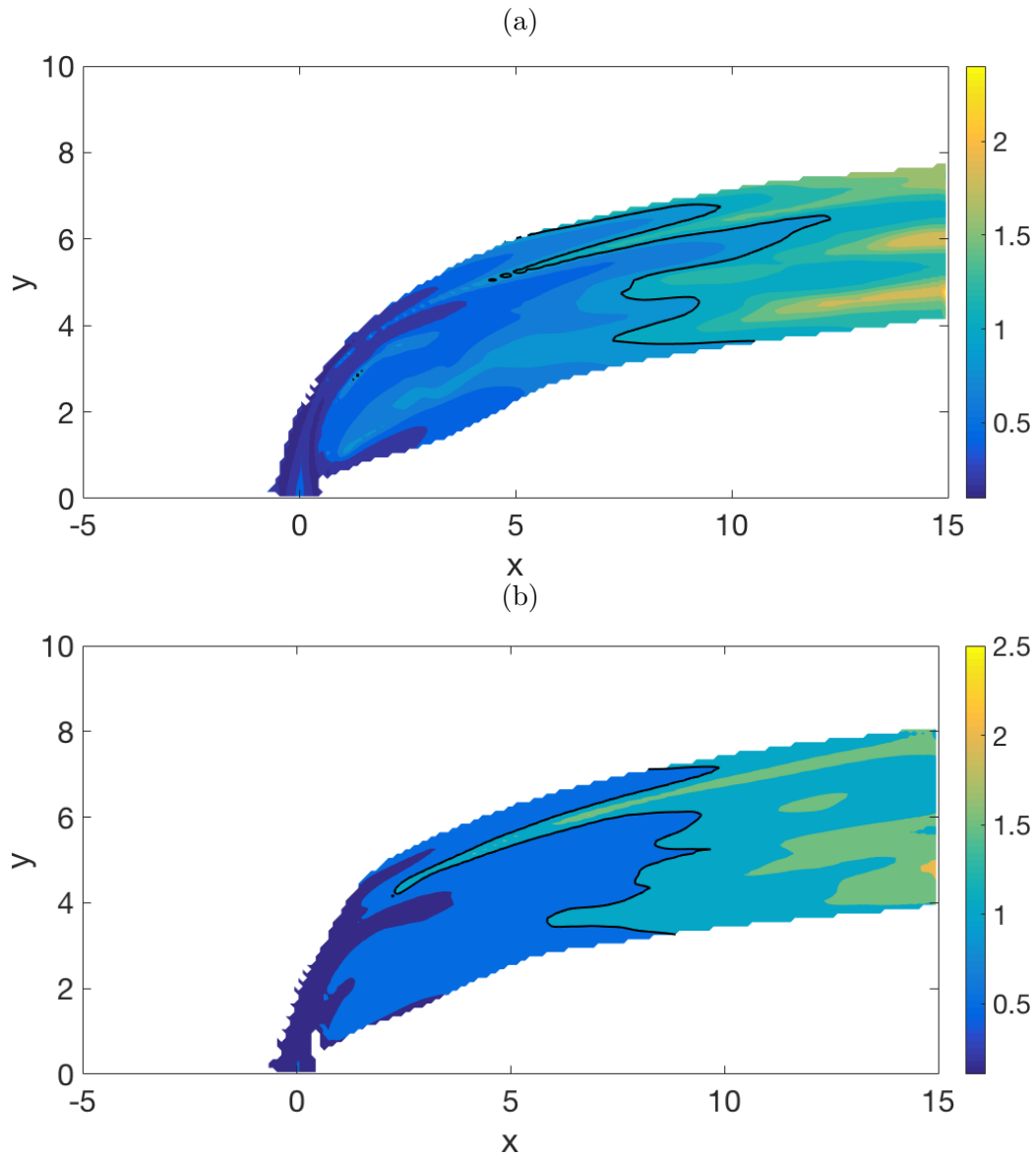


Figure 5.11: Point-wise Kolmogorov length scale ratio on plane  $z = 0$  for regions where scalar concentration  $c \geq 0.05$  (a) LES and (b) DNS simulations run at  $V_{av}/U_{max} = 3.05$ ,  $d = 2.06$  and  $Re = 640$ . Black line indicates the contour where  $\eta/\Delta x = 1$ .

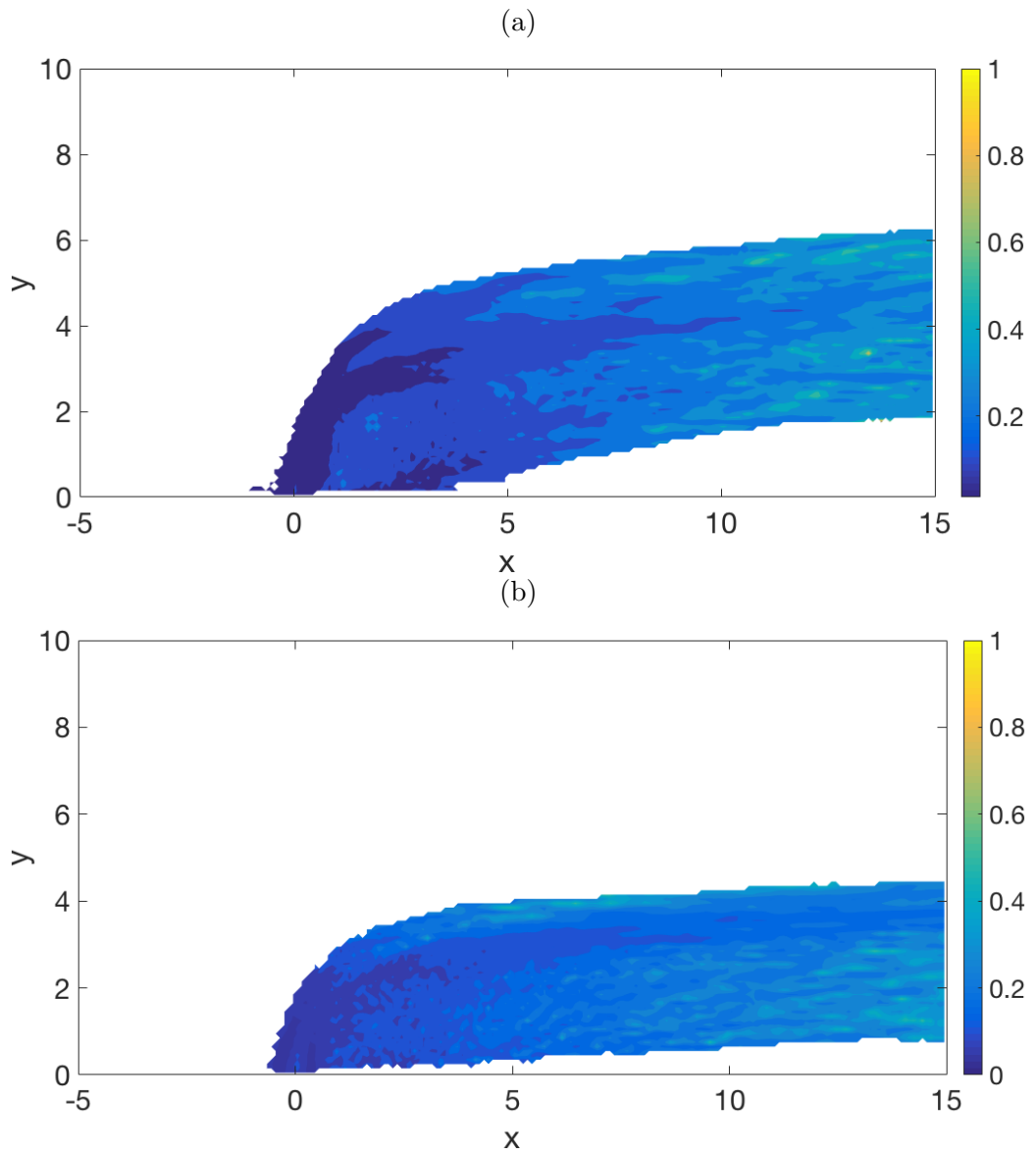


Figure 5.12: Point-wise Kolmogorov length scale ratio on plane  $z = 0$  for regions where scalar concentration  $c \geq 0.05$  (a) LES and (b) DNS simulations run at  $V_{av}/U_{max} = 2.2$ ,  $d = 0.28$  and  $Re = 13640$ .



## 5.5 Conclusion

At low Reynolds numbers the differences between a direct numerical simulation and a large-eddy simulation using the stretched-vortex model are very small, indicating that the sub-grid scale model is switching off as it should. The Kolmogorov length scale ratio shows that the flow was not fully resolved near the jet inlet on the computational grid that was used, so further grid refinement is necessary to adequately resolve the flow for a DNS. At higher Reynolds numbers the differences between the two methods of simulation increase, visible in velocity profiles, trajectories and power spectra. The sub-grid model affects the magnitude and distribution of energy in the system, seen in the spectra, as well as the depth of penetration of the jet into the crossflow, as seen in the trajectories and the velocity and scalar profiles.

To fully investigate the impact of the stretched-vortex model on a simulation, it is necessary to run simulations at higher Reynolds numbers than were used here. The low Reynolds number simulations were well below the recognised point of  $Re = 1 \times 10^4$  for flows to transition into turbulence, while the high Reynolds number simulations were only slightly above this transition point.



# Chapter 6

## Conclusion

The work undertaken in the current thesis investigated a single round jet in crossflow, in a Reynolds number range of  $Re = 243$  to  $Re = 2.05 \times 10^4$ , and a jet inlet velocity ratio range of  $V_{av}/U_{max} = 0.405$  to  $V_{av}/U_{max} = 3$ . Large-eddy simulations were performed using a hybrid second-order central finite difference and spectral method, and the stretched vortex model to approximate the impact of the sub-grid stresses and flux functions used in the simulation were written in the computational language Julia.

Results of simulations were compared to experimental results from Cambonie et al [6], and to simulations by Muppidi et al [40], Yuan et al [59], Wegner et al [56] and to simulations using an independently written code. It was shown that characteristics of the jet inlet, such as the average velocity and velocity profile, had a strong impact on the results of the simulations. Boundary conditions were also found to have an impact on the results, particularly in low velocity ratio flows that did not penetrate deeply into the crossflow.

Simulations were run at average jet inlet velocities of  $V_{av}/U_{max} = 0.405$ ,  $V_{av}/U_{max} = 2.25$  and  $V_{av}/U_{max} = 3$ , with boundary layer thickness and Reynolds number held approximately constant. It was found that increasing the velocity ratio leads to deeper jet penetration and more entrainment of crossflow fluid into the jet plume. The amount of energy present at all wavenumbers also increased, with energy spectra of all three simulations being close to parallel.

Large-eddy simulations were performed at low Reynolds number,  $Re = 640$ , with an average jet inlet velocity of  $V_{av} = 3.05$  and high Reynolds number,  $Re = 13640$ , with an average jet inlet velocity of  $V_{av} = 2.2$ . These were compared to direct numerical simulations run on the same domain with the same parameters. The low Reynolds number simulations showed little difference between the results of the large-eddy simulation and the direct nu-

merical simulation, with trajectories, velocity and scalar profiles and spectra all very similar, although an investigation of the Kolmogorov length scale showed that the flow was still not fully resolved on the computational grid used. At higher Reynolds numbers the difference between the large-eddy simulation and the direct numerical simulation was much more pronounced. The jet in the large-eddy simulation penetrated significantly further into the crossflow, shown in both velocity and scalar profiles and in trajectories. The energy distribution also varied between the direct numerical simulation and the large-eddy simulation, with more energy in the large scales and less in the small scales in the large-eddy simulation. The spectra of the large-eddy simulation also had a slope close to the ideal  $-\frac{5}{3}$ .

The Julia language was found to be straightforward to use, with built-in functions or downloadable packages available for everything that needed to be done, from creating text strings for file names to debugging functions. It was equally simple to use Julia both on desktop computers and high-performance computers, and it ran smoothly in both situations. The `ccall` function was essential for the use of the turbulence model, allowing Fortran code to be called natively within a Julia script. The only downside of Julia was the lack of a reliable three-dimensional graphing package. While packages to produce these graphics did become available over the course of the research, they were not yet as well developed as those available in programs such as MATLAB.

## 6.1 Future work

In order to understand further the relationship between jet inlet velocity and flow characteristics such as those investigated in chapter 4, it would be useful to run simulations at a wider range of jet inlet velocities. It would also be interesting to investigate the effect of the Reynolds number when all other parameters were held constant, to capture a mixing transition in the flow, such as that described by Dimotakis [15].

The effect of velocity profiles of both the jet and the crossflow were not investigated during this work. The jet inlet profile and boundary layer thickness have been shown by Muppidi and Mahesh to have an effect on the trajectory of the jet [40], however the impact of other crossflow inlet profiles other than the boundary layer on flow characteristics have not been investigated. This could include the simulation of a jet in an atmospheric shear layer, or a jet entering into a pipe flow with a parabolic or plug shaped profile. The no-slip boundary conditions on the lower wall were shown here to have an impact on low jet-inlet-velocity flows, so an investigation of different possibilities for lower and upper walls, such as a no-slip boundary on the lower

wall and a no stress boundary on the upper wall, could prove interesting.

By using the dissipation ratio and Kolmogorov length scale ratio, it was shown in this thesis that the simulations performed were highly unresolved in the vicinity of the jet inlet. Muppidi and Mahesh [40] use a refined mesh in the region surrounding the jet inlet to moderate this. It would be possible to implement a similar refined mesh in my code, to better capture the development of turbulence in the flow.

The Julia language has native support for parallelisation of functions. In the current setup of the code it would be possible to separate the wavenumber space simulation domain into smaller regions by wavenumber range, however there was not time to achieve this. Parallelisation would allow simulations to be run with larger domains and velocity ratios without overly increasing the computational time required.



# Bibliography

- [1] J. Bezanson, A. Edelman, S Karpinski, and V. B. Shah. Julia: A fresh approach to numerical computing. *CoRR*, abs/1411.1607, 2014.
- [2] J. Bezanson, S. Karpinski, V. B. Shah, and A. Edelman. Julia: A fast dynamic language for technical computing. *CoRR*, abs/1209.5145, 2012.
- [3] G. A. Blaisdell, E. T. Spyropoulos, and J. H. Qin. The effect of formulation of nonlinear terms on aliasing errors in spectral methods. *Appl. Numer. Math.*, 21:207 – 219, 1996.
- [4] J. N. Blanchard, Y. Brunet, and A. Merlen. Influence of a counter rotating pair on the stability of a jet in a cross flow: An experimental study by flow visualizations. *Exp Fluids*, 26:63 – 74, 1999.
- [5] J. E. Broadwell and R. E. Breidenthal. Structure and mixing of a transverse jet in incompressible flow. *J. Fluid Mech.*, 148:405–412, 1984.
- [6] T. Cambonie, N. Gautier, and J.-L. Aider. Experimental study of counter-rotating vortex pair trajectories induced by a round jet in cross-flow at low velocity ratios. *Exp Fluids*, 54:1475–1488, 2013.
- [7] C. Canuto, M. Y. Hussaini, A. Quarteroni, and T. A. Jr. Zang. *Spectral Methods in Fluid Dynamics*. Springer-Verlag Berlin Heidelberg, 1988.
- [8] G. Chochua, W. Shyy, S. Thakur, A. Branovic, J. Lienau, L. Porter, and D. Lischincky. A computational and experimental investigation of turbulent jet and crossflow interaction. *Numer Heat Tr A-Appl*, 38(6):557–572, 2000.
- [9] M. S. Chong, A. E. Perry, and B. J. Cantwell. A general classification of three-dimensional flow fields. *Phys. Fluids A*, 2(5):765 – 777, May 1990.
- [10] D. Chung and G. Matheou. Large-eddy simulation of stratified turbulence. part i: A vortex-based subgrid-scale model. *J Atmos Sci*, 71:1863 – 1879, May 2014.

- [11] Julia Computing. February 2017 newsletter. <http://juliacomputing.com/blog/2017/02/03/newsletter.html>.
- [12] L. Cortelezzi and A. R. Karagozian. On the formation of the counter-rotating vortex pair in transverse jets. *J. Fluid Mech*, 446:347 – 373, 2001.
- [13] P. R. E. Cutler. *On the Structure and Mixing of a Jet in Crossflow*. PhD thesis, University of Adelaide Department of Mechanical Engineering, 2002.
- [14] O. Desjardins, G. Blanquart, G. Balarac, and H. Pitsch. High order conservative finite difference scheme for variable density low mach number turbulent flows. *J. Comp. Phys*, 227:7125–7159, 2008.
- [15] P. E. Dimotakis. The mixing transition in turbulent flows. *J. Fluid Mech.*, 409:69 – 98, 2000.
- [16] J. M. Faddy and D. I. Pullin. Flow structure in a model of aircraft trailing vortices. *Phys. Fluids*, 17:1 – 17, 2005.
- [17] R. Fearn and R. P. Weston. Vorticity associated with a jet in cross flow. *AIAA Journal*, 12:1666 – 1671, December 1974.
- [18] A. Ferrante, G. Matheou, and P. E. Dimotakis. Les of an inclined sonic jet into a turbulent crossflow at mach 3.6. *J Turbl*, 12(2):1 – 32, 2011.
- [19] N. S. Ghaisas, D. A Shetty, and S. H. Frankel. Large eddy simulation of thermal driven cavity: Evaluation of subgrid models and flow physics. *Int J Heat Mass Tran*, 56:606–624, 2013.
- [20] Andreopoulos J. and Rodi W. Experimental investigations of jets in a crossflow. *J. Fluid Mech.*, 138:93 – 127, 1984.
- [21] Y. Kamotani and I. Greber. Experiments on a turbulent jet in a cross flow. *AIAA Journal*, 10(11):1425 – 1429, November 1972.
- [22] R. M. Kelso, Lim. T. T., and Perry. A. E. An experimental study of round jets in cross-flow. *J. Fluid Mech*, 306:111–144, 1996.
- [23] V. Kolar. Vortex identification: New requirements and limitations. *Int J Heat Fluid Fl*, 28:683 – 652, 2007.
- [24] B. Kosovic, D. I. Pullin, and R. Samtaney. Subgrid-scale modeling for large-eddy simulations of compressible turbulence. *Phys. Fluids*, 14(4):1511 – 1522, 2002.



- [25] Pijush K. Kundu, Ira M. Cohen, and David R. Dowling. *Fluid Mechanics*. Academic Press, 5th edition edition, 2012.
- [26] M. T. Landanl and E. Mollo-Christensen. *Turbulence and random processes in fluid mechanics*. Cambridge University Press, 1992.
- [27] H. Le, P. Moin, and J. Kim. Direct numerical simulation of turbulent flow over a backwards facing step. *J. Fluid Mech.*, 330:349 – 374, 1997.
- [28] D. K. Lilly. A proposed modification of the germano sub-grid scale closure method. *Phys. Fluids A*, 4(3):633 – 635, March 1992.
- [29] K. Mahesh. The interaction of jets with crossflow. *Annu. Rev. Fluid Mech.*, 45:379–407, 2013.
- [30] K. Mahesh, G. Constantinescu, and P. Moin. A numerical method for large-eddy simulation in complex geometries. *J. Comp. Phys*, 197:215 – 240, 2004.
- [31] G. Matheou, C. P. Bonanos, C. Pantano, and P. E. Dimotakis. Large-eddy simulation of mixing in a recirculating shear flow. *J. Fluid Mech*, 646:375–414, 2010.
- [32] G. Matheou and D. Chung. Large-eddy simulation of stratified turbulence. part ii: Application of the stretched-vortex model to the atmospheric boundary layer. *J Atmos Sci*, 71:4439 – 4460, December 2014.
- [33] G. Matheou and P. E. Dimotakis. Scalar excursions in large-eddy simulations. *J. Comp. Phys*, 327:97–120, 2016.
- [34] T. Mattner. personal communication.
- [35] T. W. Mattner. A refined stretched vortex model for large-eddy simulation of turbulent mixing layers. In *17th Australasian Fluid Mechanics Conference*, Auckland, New Zealand, December 2010.
- [36] T. W. Mattner. Large-eddy simulations of turbulent mixing layers using the stretched-vortex model. *J. Fluid Mech*, 671:507–534, 2011.
- [37] A. Misra and D. I. Pullin. A vortex-based subgrid stress model for large-eddy simulation. *Phys. Fluids*, 9(8):2443–2455, 1997.
- [38] P. Moin. *Fundamentals of Engineering Numerical Analysis*. Cambridge University Press, 2001.

- [39] Y. Morinishi, T. S. Lund, O. V. Vasilyev, and P. Moin. Fully conservative higher order finite difference schemes for incompressible flow. *J. Comp. Phys*, 143:90–124, 1998.
- [40] S. Muppidi and K. Mahesh. Study of trajectories of jets in crossflow using direct numerical simulations. *J. Fluid Mech*, 530:81–100, 2005.
- [41] S. Muppidi and K. Mahesh. Direct numerical simulation of passive scalar transport in transverse jets. *J. Fluid Mech. Mech*, 598:335 – 360, 2008.
- [42] F. Nucoud, H. B. Toda, O. Cabrit, S. Bose, and J. Lee. Using singular values to build a subgrid-scale model for large eddy simulations. *Phys. Fluids*, 23:085106, 2011.
- [43] M. A. Ol’shanskii and V. M. Staroverov. On simulation of outflow boundary conditions in finite difference calculations for incompressible fluid. *Int. J. Numer. Meth. Fluids*, 33:499 – 534, 2000.
- [44] D. I. Pullin. A vortex-based model for the subgrid flux of a passive scalar. *Phys. Fluids*, 12(9):2311 – 2319, September 2000.
- [45] D. I. Pullin and P. G. Saffman. Reynolds stresses and one-dimensional spectra for a vortex model of homogeneous anisotropic turbulence. *Phys. Fluids*, 6(5):1787 – 1796, May 1994.
- [46] A. M. Ruiz, G. Lacaze, and J. C. Oefelein. Flow topologies and turbulence scales in a jet-in-cross-flow. *Phys. Fluids*, 27(045101):1 – 35, 2015.
- [47] P. Sagaut. *Large Eddy Simulation for Incompressible Flows*. Springer, 3rd edition edition, 2006.
- [48] J. Smagorinsky. General circulation experiments with the primitive equations, i. the basic experiment. *Mon. Weather Rev*, 91(3):99 – 164, March 1963.
- [49] S. H. Smith and M. G. Mungal. Mixing, structure and scaling of the jet in crossflow. *J. Fluid. Mech*, 357:83 – 122, 1998.
- [50] G. I. Taylor and A. E. Green. Mechanisms of the production of small eddies from large ones. *P Roy Soc Lond A Mat*, 158(895):499 – 521, 1937.
- [51] The HDF Group. Hierarchical Data Format, version 5, 1997-2016. /HDF5/.

- [52] L. N. Trefethen. Group velocity in finite difference schemes. *SIAM J Appl Math*, 24(2):113 – 136, 1982.
- [53] M. Uhlmann. *The need for de-aliasing in a Chebyshev pseudo-spectral method*. Potsdam Institute for Climate Impact Research, 2000.
- [54] T. Voelkl, D. I. Pullin, and D. C. Chan. A physical space version of the stretched-vortex subgrid-stress model for large-eddy simulation. *Phys. Fluids*, 12:1810 – 1825, 2000.
- [55] B. Vreman, B. Geurts, and H. Kuerten. On the formulation of the dynamic mixed subgrid-scale model. *Phys. Fluids*, 6:4057 – 4059, 1994.
- [56] B. Wegner, Y. Huai, and A. Sadiki. Comparative study of turbulent mixing in jet in crossflow configurations using les. *Int J Heat Fluid Fl*, 25:767– 775, 2004.
- [57] L. J. Wicker. A two-step adams–bashforth–moulton split-explicit integrator for compressible atmospheric models. *Monthly Weather Review*, 137:3588–3595, 2009.
- [58] L. L. Yuan and R. L. Street. Trajectory and entrainment of a round jet in crossflow. *Phys. Fluids*, 10(9):2323 – 2335, 1998.
- [59] L. L. Yuan, R. L. Street, and J. H. Ferziger. Large-eddy simulations of a round jet in crossflow. *J. Fluid Mech*, 379:71–104, 1999.
- [60] T. A. Zang. On the rotation and skew-symmetric forms for incompressible flow simulations. *Applied Numerical Mathematics*, 7:27–40, 1991.
- [61] Y. Zang, R. L. Street, and J. R. Koseff. A dynamic mixed subgrid-scale model and its application to turbulent recirculating flows. *Phys. Fluids A*, 5:3186 – 3196, 1993.
- [62] J. Zhou, R. J. Adrian, S. Balachandar, and T. M. Kendall. Mechanisms for generating coherent packets of hairpin vortices in channel flow. *J. Fluid. Mech*, 387:353 – 396, 1999.